

IMPROVED DETECTION OF GOLD NANOPARTICLE
LABELS FOR PAPER-BASED ANALYTICS

A Thesis

presented to

the Faculty of California Polytechnic State University,
San Luis Obispo

In Partial Fulfillment

of the Requirements for the Degree

Master of Science in Biomedical Engineering

by

Brian Taylor Daugherty

March 2015

© 2015

Brian Taylor Daugherty

ALL RIGHTS RESERVED

COMMITTEE MEMBERSHIP

TITLE: Improved Detection of Gold Nanoparticle
Labels for Paper-based Analytics

AUTHOR: Brian Taylor Daugherty

DATE SUBMITTED: March 2015

COMMITTEE CHAIR: David Clague, Ph.D.
Associate Professor of Biomedical Engineering

COMMITTEE MEMBER: Scott Hazelwood, Ph.D.
Associate Professor of Biomedical Engineering

COMMITTEE MEMBER: Daniel Walsh, Ph.D.
Professor of Biomedical Engineering

ABSTRACT

Improved Detection of Gold Nanoparticle Labels for Paper-based Analytics

Brian Taylor Daugherty

Point-of-care diagnostic devices are well-suited, and typically designed, for remote and/or resource-limited environments. The obvious application is for healthcare in the developing world; however, other additional important uses exist, including for security (biothreat agent detection) and human health and research during future manned deep space exploration missions.

The objective of this thesis was to develop, and experimentally validate, techniques for improved quantified detection of labels used in lateral flow assays. Limits of detection were characterized for: (a) optical approaches, i.e., unaided eye, mobile electronic device camera images and microscope images with image analysis software developed through this thesis, and (b) a conductance based approach with direct measurement of electrical impedance in the detection region using hardware and software that were developed. Analysis of camera images from mobile electronic devices enables simultaneous detection of many targets on a multiplexed assay. Additionally, a peripheral device was designed which was intended to provide conductimetric analysis capabilities to mobile electronic devices.

The detection limit of gold nanoparticles for the unaided eye was determined at a concentration of $(3.98 \pm 0.40) \times 10^{-11}$ M; mobile electronic device image analysis, microscope image analysis, and the conductance based approach showed improvements by approximately a half to a third, an order of magnitude, and three orders of magnitude, respectively.

Keywords: point of care diagnostic, lateral flow assay, colloidal gold, multiplexed assay, limit of detection, image analysis, conductance, nitrocellulose, smartphone, mobile electronic device

ACKNOWLEDGMENTS

First and foremost I would like to thank my advisor, Dr. David Clague, for his support and direction through the entirety of my thesis project and for his guidance throughout my academic career at Cal Poly.

Additionally, the time and support of my thesis committee members, Drs. Scott Hazelwood and Daniel Walsh, is very much appreciated.

I am also very grateful for the grant that my work received from the University of California, Santa Cruz's University Affiliated Research Center, and the National Aeronautics and Space Administration (NASA)'s Ames Research Center and for Dr. Michael Krihak's work in securing it. Without this essential funding, the project would not have been possible.

I would like to thank Cal Poly for the resources and opportunities that it has provided me. I would also like to express my gratitude to the faculty and staff that I have encountered at Cal Poly (especially in the biomedical engineering, physics, and aerospace engineering departments) for the invaluable knowledge they have bestowed upon me and for their dedicated and hard work.

Finally, I would like to thank my parents, brother, and my extended family, as well as my friends, classmates, colleagues, and everyone else I've met through my academic endeavors for their support and friendship.

TABLE OF CONTENTS

	Page
LIST OF TABLES	ix
LIST OF FIGURES.....	x
CHAPTER	
1. INTRODUCTION.....	1
1.1. Thesis Objective	1
1.2. Point-of-Care Diagnostics	2
1.3. Applications in Space Exploration.....	4
1.4. Lateral Flow Assays	7
1.5. Gold Nanoparticles.....	12
2. MATERIALS AND METHODS.....	16
2.1. Membrane Preparation	16
2.1.1. Printing Solid Ink Patterns	16
2.1.2. Reflowing Solid Ink to Create Complete Hydrophobic Barriers.....	18
2.1.3. Concentration Factor and Equivalent Target Concentration	22
2.2. Optical Detection.....	26
2.2.1. Dye and GNPs	26
2.2.2. Visual.....	28
2.2.3. Mobile Electronic Device Image Analysis	33
2.2.3.1. Spectral Sensitivity:	33

2.2.3.2. MATLAB:	37
2.2.3.3. Mobile Electronic Device Cameras:	46
2.2.4. Image Analysis – Microscope.....	46
2.3. Conductance Based Detection.....	50
2.3.1. Initial Approach.....	50
2.3.2. Refined Conductance Based Detection Approach	54
2.3.2.1. Electrode Cleaning:	57
2.3.2.2. Contact Resistance:	58
2.3.2.3. Temperature Control System:	58
2.3.2.4. Electronics and Measurement Strategies:	60
2.3.2.5. LabVIEW:	65
2.3.2.6. Cell Constant:	70
2.3.3. Peripheral Device Design.....	70
3. RESULTS.....	71
3.1. Visual.....	71
3.2. Image Analysis	72
3.2.1. MED	72
3.2.2. Microscope 5×.....	77
3.2.3. Microscope 10×.....	78
3.3. Conductimetric Detection	79

3.4. Peripheral Device Design.....	80
4. DISCUSSION	83
4.1. Visual.....	83
4.2. Image Analysis	83
4.3. Conductimetric Detection	85
4.3.1. Peripheral Device	87
4.4. Comparison to Literature	88
4.5. LOD Comparison	89
5. CONCLUSIONS	92
5.1. Future Work	93
BIBLIOGRAPHY	96
APPENDICES	
A : Image Analysis Code (MATLAB).....	102
B : Microscope Image Processing Code (MATLAB)	111
C : Electrical Impedance Measurement Block Diagram (LabVIEW)	112
D : Impedance Value Extraction Code (MATLAB).....	113
E : GNP Concentration Protocol.....	115

LIST OF TABLES

Table	Page
1. Concentrations of Dye Used in Visual Detection Limit Determination.....	29
2. Erythrosine Samples and Their Respective Concentrations Used in LOD Evaluation with MED Images.....	38
3. Samples and Concentrations Used With Microscope LOD Evaluation	49
4. Samples, Concentrations and Buffer Concentration Used for Conductimetric Testing (Note that PBS concentration is listed as combined salt and phosphate concentration – suspended GNP concentration is zero)	55
5. Visual Detection Limit	71
6. Appropriate Centrifuge Speeds and Times for Various GNP Sizes	115

LIST OF FIGURES

Figure	Page
1. Elevated levels of biomarkers, CK-MB and Troponin T, following myocardial infarction [12].	6
2. Proposed flight trajectory for a Mars flyby mission lasting 501 days. The solid line shows the outbound path and the dashed line shows the return path [14].	7
3. Layout and signal generation of competitive and sandwich LFAs. In the competitive assay, the response is negatively correlated with the presence of analyte in the sample (top); in the sandwich assay the response is proportional to the amount of analyte in the sample (bottom) [16].	8
4. Visualization of typical sandwich LFA architecture, which shows beginning, intermediate, and end states for the assay (NASA).	10
5. Visualization of a localized surface plasmon [22].	13
6. Colors of GNPs of different sizes (credit: Irawati Kandela).	14
7. Xerox ColorQube 8570 solid ink printer used for printing hydrophobic wax barriers on nitrocellulose.	17
8. Illustration of pre- and post-heating states for a printed-on NC membrane. This cross-section is perpendicular to the plane of the membrane and the printed line.	18
9. Photos of a solid ink pattern on a NC membrane before and after heating. It is almost impossible to see the pattern through the membrane in the before photo (due to very little penetration and the high opacity of NC).	19

10. IKA C-MAG HP 10 digitally controlled hot plate used for reflowing solid ink to created complete hydrophobic barriers through the depth of membranes.....	20
11. Comparison of absorbance spectra of GNPs and erythrosine dye (approximate) [37].	27
12. Samples used for visual detection limit determination. The tops and bottoms of the membranes are darkened in this image to highlight the detection areas viewed by test subjects. The darkened areas were completely obscured during testing.	30
13. Black construction paper used to mask the samples on the membrane to the shape and area that is found with typical LFAs. Left, window open, showing sample number; right, window closed.	31
14. Diagram of construction paper, nitrocellulose reference, and sample in membrane, showing viewing angle and projected sample height.	32
15. Sample well matrix used for LOD determination via automated image processing of photographs from MED cameras.....	34
16. Front view of spectrometer, showing slit, with razor blade edges, where light enters the system.	35
17. Rear view of spectrometer, showing tape used to attach it to MEDs and the 1000 line/mm diffraction grating.	36
18. Spectrometer attached to a smartphone in preparation for determining the spectral sensitivity of its camera sensor. Left, front view of the smartphone and spectrometer; right, rear view.....	37

19. File import for image processing with graphical user interface.	39
20. Unprocessed image with three corners marked and the fourth selected to be marked. Rows contain samples of the same concentration, the 10 left columns contain samples of decreasing dye concentrations, the 11 th column from the left contains 8× concentrated GNP suspension, and the 12 th column contains DI water as a blank.	40
21. Partially processed image displayed in MATLAB, with column and row centerlines (white) and reference locations (black diamonds) superimposed on it. Intersections of the white lines are sample data collection locations.	42
22. Visualization of absorbance. Light source, reflected light intensities, the membrane, and the optical path length are shown.	44
23. Olympus microscope with camera unit used for capturing images of samples on NC.	47
24. Test card used for collecting data with microscope, loaded with dye sample number 6.	48
25. Exploded diagram showing the layers of the initial conductimetric test platform, which was designed to enable both optical and impedance measurements of samples.	51
26. Close-up photograph of electrode negative used for screen printing.	52
27. Screen printed electrodes. Top, conductive graphite ink; bottom, conductive silver ink. Images were adjusted to improve visibility.	53

28. Four-terminal electrode clamp used for conductimetric measurements (perspective view).	56
29. Four-terminal electrode clamp used for conductimetric measurements (frontal view).	57
30. Beaker with platform and temperature probe taped in place. Temperature probe is marked with a red circle.	59
31. Temperature control system setup. The beaker is marked with a yellow rectangle. The thermometer is labeled, and approximate warm exhaust and cool air directions are indicated.	60
32. Original dual instrumentation amplifiers which were used for testing purposes. This design uses three op-amps per instrumentation amplifier. Potentiometers are present to provide adjustable gain for each channel and safety diodes are visible.	61
33. Upgraded measurement circuit incorporating a dual instrumentation amplifier integrated circuit.	62
34. Schematic for two-op-amp instrumentation amplifier circuit used in INA2126.	63
35. Simplified schematic of sensing circuitry used for conductimetric detection.	64
36. Front panel of LabVIEW conductimetric data acquisition software. (a) Full- scale impedance magnitude (Ω) vs. time (ms); (b) scaled impedance magnitude (Ω) vs. time (ms); (c) scaled phase angle (degrees) vs. time (ms); (d) scaled raw input from oscilloscope, potential (V) vs. time (s), Ch. 0 is	

white (sensor), Ch. 1 is red (resistor); (e) scaled power spectrum of Ch. 0, power (V_{rms}^2) vs. frequency (Hz).....	66
37. Settings and readouts on front panel. Note that a maximum number of measurements can be set, but the “STOP” button can initiate an interrupt to cease acquisition and save data.....	67
38. Example of plot and second order polynomial fit generated from collected data.....	69
39. Spectral sensitivity of camera from Samsung Galaxy S smartphone. The peak sensitivity and the peak absorbance wavelengths for the GNPs and dye that were used are indicated.	72
40. Spectral sensitivity of camera from iPad mini. The peak sensitivity of the green channel and the peak absorbance wavelengths for the GNPs and dye that were used are indicated.	73
41. Spectral sensitivity of iPhone 5 camera. The peak green channel sensitivity and the peak absorbance wavelengths the GNPs and dye are indicated.	73
42. Linear regression of data collected from analysis of image captured with Galaxy S with erythrosine dye. The absorbance values of 8× concentrated GNP were measured, plotted, and used to calculate equivalent GNP concentrations for dye. Error bars represent the standard error of the mean (SEM) absorbance from ten replicates.....	74
43. Linear regression of data collected from analysis of image captured with iPad mini with erythrosine dye. The absorbance values of 8× concentrated GNP	

were measured, plotted, and used to calculate equivalent GNP concentrations for dye. Error bars represent the SEM absorbance from ten replicates.	75
44. Linear regression of data collected from analysis of image captured with iPhone 5 with erythrosine dye. The absorbance values of 8× concentrated GNP were measured, plotted, and used to calculate equivalent GNP concentrations for dye. Error bars represent the SEM absorbance from ten replicates.....	76
45. Result of analysis of images collected from the microscope using a 5× objective and using erythrosine. The absorbance values for 8× GNP were measured and plotted and then used to calculate equivalent concentrations of dye. Error bars represent the SEM absorbance from ten replicates.....	77
46. Result of analysis of images collected from the microscope using a 10× objective and using erythrosine. The absorbance values for 8× GNP were measured and plotted and then used to calculate equivalent concentrations of dye. Error bars represent the SEM absorbance from ten replicates.....	78
47. Comparison of two- and four- terminal sensing measurements.	79
48. Data collected using the conductimetric approach, fitted using a linear regression. Error bars represent the SEM conductivity.	80
49. Block diagram for peripheral device design to provide MEDs with electrical impedance measurement capabilities.....	81
50. Simplified schematic for peripheral device with part numbers indicated.	82
51. Comparison of LODs obtained with different measurement approaches. Error bars represent SEM.	90

52. Comparison of LODs obtained with each approach (after logarithmic transformation of the data). Error bars represent SEM. Tukey results are shown as letters below each column. Groups not sharing letters are significantly different ($p < 0.01$). 91

1. INTRODUCTION

In completing this thesis, techniques for improved quantified detection of labels used in lateral flow assays (LFAs) were developed and experimentally validated. Limits of detection (LODs) were evaluated for optical and conductimetric approaches. Mobile electronic devices (MEDs) were used to capture images, and enabled simultaneous detection capabilities for multiplexed assays through image analysis software that was developed. Hardware and software were developed and used in conjunction with preexisting hardware for the conductance based approach. A peripheral device, which is intended to provide conductimetric analysis capabilities to MEDs, was also designed.

1.1. Thesis Objective

The objective of this thesis was to develop techniques for improved quantified detection of labels used in LFAs. To achieve this objective, two overarching approaches were explored:

- Optical – LODs using dye via unaided eye, MED image analysis, and microscope image analysis
- Conductimetric – LOD of gold nanoparticle (GNP) labels via direct measurement with conductance measurement system

Additionally, a preliminary design was completed for a device, based on the conductance measurement hardware that was used, to connect to a MED (e.g. a

smartphone or tablet) and provide it with the capability to directly measure conductance within the detection region of an LFA membrane.

1.2. Point-of-Care Diagnostics

The implicit objective of this thesis was to advance the capabilities of detection at the point of care (POC).

The promise of POC diagnostics is to enable care providers to rapidly collect data and make diagnoses at the POC without relying on third parties for analysis. It also typically necessitates small form factor, low cost, and ultra-portability in devices [1]. These characteristics make POC diagnostic devices ideal for many remote and/or resource-limited environments.

One main area that can benefit greatly from POC diagnostics is health care in developing nations. Infectious disease is a major cause of mortality and morbidity for people living in developing nations [2]. In 2012, nearly one third of deaths in developing nations were caused by major infectious diseases such as malaria, human immunodeficiency virus (HIV), and tuberculosis [3]. Rapid LFA diagnostic tests exist for the agents that cause these diseases or byproducts resulting from them, but these tests can be improved by increasing sensitivity, accuracy, and incorporating simultaneous detection of multiple analytes [4] [5]. When disease can be quickly and inexpensively diagnosed at the POC, patients can be immediately and effectively treated, which enables health care workers to provide care to a greater number of patients [6]. Alternatively, when a patient is required to make a return trip to a clinic to access their test results, the

time before treatment can begin is extended and a significant number of patients do not follow through due to inconvenience [5]. Improved POC diagnostics could lead to a large reduction in lost life caused by the major infectious diseases in resource-limited settings in developing nations [7]. Another advantage to using LFAs in this application is that they are made from materials that can easily be incinerated after use, safely disposing of biohazardous waste [8]. This is important because adequate waste disposal facilities are often non-existent at the POC in the developing world.

The U.S. government also has an interest in the development of POC testing platforms that enable multiplexed detection of many biothreat agents simultaneously for homeland and military security [4]. Potential biothreat agents that can be tested for at the POC include *Variola major* (smallpox), *Bacillus anthracis* (anthrax), *Yersinia pestis* (plague), *Clostridium botulinum* neurotoxins (botulism), *Francisella tularensis* (tularemia), and *Ricinus communis* (ricin toxin). In scenarios where a biothreat agent could have been deployed, it is important to be able to quickly and accurately identify it so that, if necessary, appropriate action can be taken to limit dissemination, transmission, and potential casualties [9].

Additionally, at-home diagnostics can allow individuals to inexpensively and independently collect information about and diagnose their own health state [4]. A well-known example of LFA-based POC diagnostics at home is the home pregnancy test.

1.3. Applications in Space Exploration

The National Aeronautics and Space Administration (NASA) has an interest in advancing POC diagnostics to address goals within its Exploration Medical Capability (ExMC) Element. The ExMC is one of six elements within NASA's Human Research Program (HRP), which serves to reduce the likelihood of a scenario during an exploration mission where an inability to adequately recognize or treat an illness or injury in a crewmember occurs [10]. On extended human exploration missions (greater than 30 days and beyond low-Earth orbit (LEO)), an exploration medical laboratory (EML) is required to ensure astronaut health and safety even in potential cases of injury or illness. The EML is meant to consist of instruments that are capable of providing biomedical diagnostics capabilities. These instruments are required to facilitate the recognition or treatment of multiple medical conditions and possibly to continually assess the condition of an injured or ill crewmember and to monitor therapeutic interventions that guide further treatment. The EML may also be used to provide periodic health status evaluations for preventative measures and research objectives.

The functional requirements for ExMC specify that devices included in the EML should have minimized mass, volume, consumables, reagents, and power consumption and that they should be designed for ease of use by the care provider. These requirements align with the goals of POC diagnostics. It is also stated that an instrument included in EML should be readily interfaced with an onboard data storage system and that it should be capable of wireless communications. This can be easily achieved by integration of a MED with the device.

Some of the analyses that are required of EML include the detection and measurement of various biomarkers in bodily fluids such as blood, saliva, or urine. Many of the biomarkers of interest can be measured with LFA technology and, depending on the relevant concentration range and number of different analytes, one of the techniques developed in this thesis.

An example of a medical condition that could occur during an extended human exploration mission that could benefit from rapid simultaneous detection of multiple analytes is a myocardial infarction (MI) in a crewmember [11]. Following a MI, several biomarkers are released from myocardial cells into the bloodstream (see Figure 1) [12]. Elevated levels of creatine kinase myocardial band (CK-MB) and troponin T can be captured with a multiplexed LFA and simultaneously measured and analyzed with a MED using image analysis. When MI can be quickly diagnosed (and differentiated from

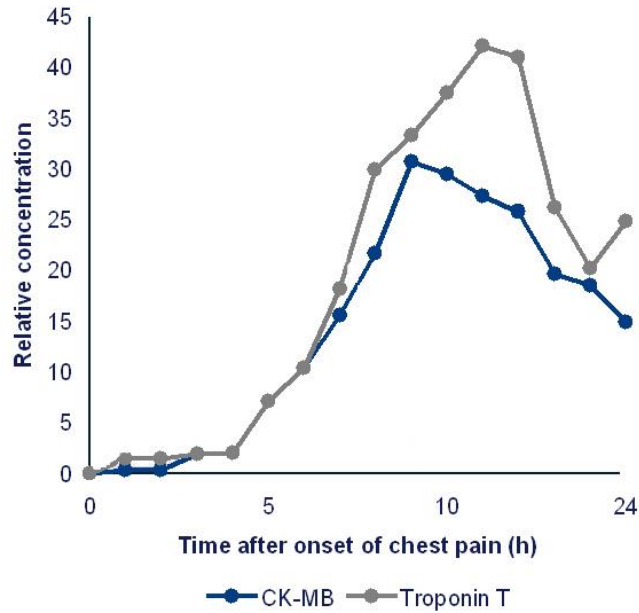


Figure 1. Elevated levels of biomarkers, CK-MB and Troponin T, following myocardial infarction [12].

angina), the likelihood and severity of permanent damage can be significantly reduced [13].

With long-duration deep space missions on NASA’s horizons (such as those to asteroids and Mars), increased autonomy regarding medical diagnostics and treatment is more important than it has been for space shuttle and International Space Station (ISS) missions in LEO. Astronauts assigned to these missions will be potentially many months of travel time away from Earth and up to nearly 45 minutes of round trip communication time delay from Earth (at maximum distance between Earth and Mars of approximately 401×10^6 km). As a general example, Figure 2 shows a proposed 2018/2019 flyby mission to Mars that lasts nearly 16.5 months. In any mission with a Mars landing, that maintains

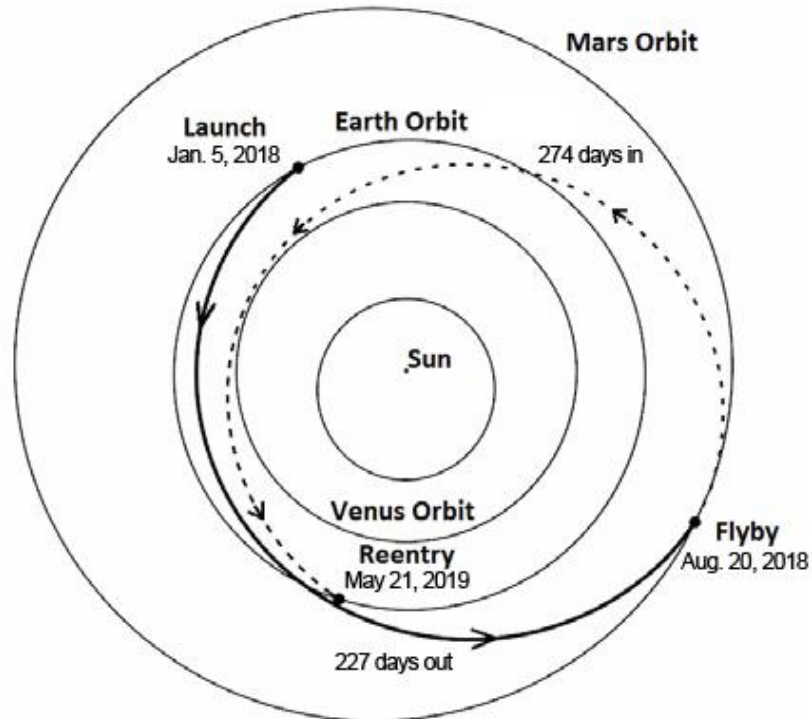


Figure 2. Proposed flight trajectory for a Mars flyby mission lasting 501 days. The solid line shows the outbound path and the dashed line shows the return path [14].

a return flight, the total mission duration will typically be longer because of time spent on the surface of the planet and waiting for a launch window for a relatively low-energy return flight trajectory to Earth.

1.4. Lateral Flow Assays

Lateral flow assays are useful for detecting a wide range of target analytes, including biomarkers that are indicative of the human body's health state. A typical sandwich LFA reports results by capturing and concentrating detector labels in its detection region, and generating a visible response as a color with intensity which

increases proportionately to the concentration of captured labels. Other types of LFAs exist, such as the competitive assay (which reports a decreasingly intense signal in the presence of the analyte, as the capture antibody binds the analyte and inhibits binding with the detector), but they all operate in principle by the formation of a complex between a detector particle that is free in the sample stream and a capture reagent that is immobilized in the detection region in the membrane (see Figure 3) [15].

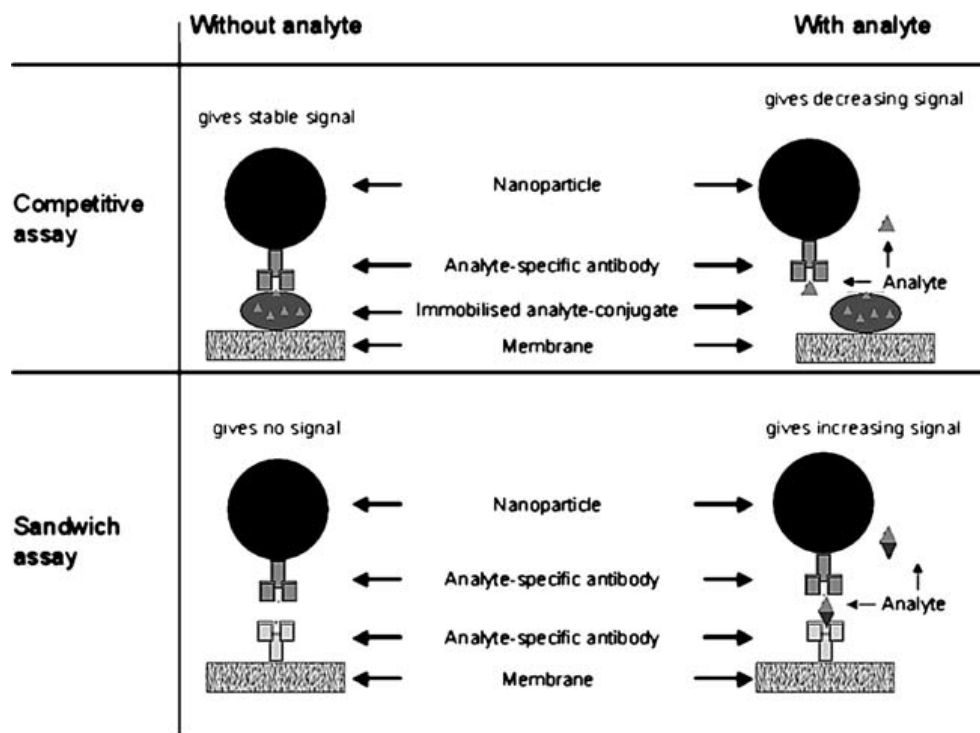


Figure 3. Layout and signal generation of competitive and sandwich LFAs. In the competitive assay, the response is negatively correlated with the presence of analyte in the sample (top); in the sandwich assay the response is proportional to the amount of analyte in the sample (bottom) [16].

Many membrane polymers, including polyvinylidene fluoride, (charge-modified) nylon, and polyethersulfone, are available for use in LFAs, but the one most commonly

used is nitrocellulose (NC). NC has several attributes that make it well suited for use as a membrane in LFAs: it is capable of adsorbing protein at a level much higher than the maximum possible number of detector labels, chemistries that make it wettable with aqueous solution do not significantly diminish its ability to adsorb protein, it can be manufactured in such a way that it has pores sufficiently large to allow lateral flow in relatively short timeframes, and it can be cast directly onto a polyester backing (which provides more robust mechanical properties than the NC alone) without affecting its ability to function as an LFA membrane [17]. Protein binding in NC membranes occurs through the electrostatic interaction of the strong dipoles of nitrate esters and the peptide bonds of proteins [15].

LFAs work by taking advantage of capillary action to spontaneously transport a sample fluid through the porous membrane medium, which eliminates the need for the fluid pumps that are used in many other microfluidic devices. This leads to the concentration of an analyte that is being targeted (if it is present) in a detection region, which results in a signal that can be evaluated. LFAs are made up of the following four main components: sample pad, conjugate pad, membrane, absorbent wicking pad. Typically, a sample is collected and dispensed onto the sample pad, where excess fluid is held as capillary forces pull it into the adjacent component, the conjugate pad. At this point, an antibody with an affinity for the analyte that the assay is testing for has previously been conjugated with a detector label, and dried in the conjugate pad. The sample fluid mixes with the antibody-conjugated detectors as it flows away from the conjugate pad and through the nitrocellulose membrane, and if the targeted analyte is

present in the sample, an antibody binds it. Two lines of additional antibodies have previously been immobilized in the NC membrane, perpendicular to the direction of flow. The first, the test line, captures analytes which have already been bound by the antibody-conjugated detector labels. The second, the control line, is made from a secondary antibody which captures antibody-conjugated detectors which have not bound an analyte. The purpose of the control line is to show that the sample volume was sufficiently large for the assay, the reagents are functional, and that there were enough antibody-conjugated detectors in the conjugate pad to completely capture all of the analyte present in the sample [18]. Figure 4 shows a visualization of how a sandwich LFA works. Some signal amplification occurs due to volume reduction (and therefore increased concentration)

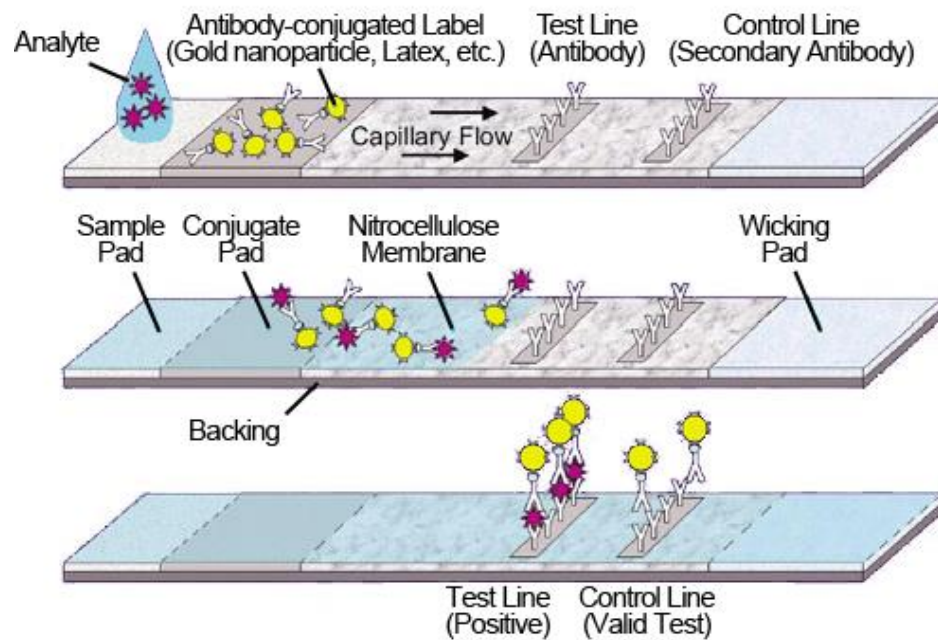


Figure 4. Visualization of typical sandwich LFA architecture, which shows beginning, intermediate, and end states for the assay (NASA).

from the original sample to the detection region (i.e., the test line). Usually the signal that is generated is evaluated visually and the assessment of presence is Boolean (i.e., “yes/no”), but color intensity and magnetic field strength (depending on the detector label used in the assay) have also been measured and used to quantitatively determine analyte concentration [19].

In a home pregnancy test LFA, the analyte that is targeted is human chorionic gonadotropin (hCG), which is a hormone produced at increasing levels by syncytiotrophoblast cells during the first trimester of pregnancy [20]. Detectors are created by conjugating antibodies that target one epitope of hCG to GNP labels. Antibodies that target a different hCG epitope are immobilized in the membrane to form the test line. Finally, the control line is made from an antibody that targets the primary anti-hCG antibody [21]. This assay is a sandwich LFA, so a greater concentration of hCG in the sample gives rise to a more intense signal, up to a maximum, in the detection region.

The main advantages of LFAs over other detection techniques like western blot and ELISA are that they are one-step assays (with a very simple test procedure, and no washing step necessary). They are fast, they are inexpensive, and they use small sample volumes.

The primary limitations of typical LFAs are lack of parallel testing capabilities and subjective qualitative or semi-quantitative results with relatively high LODs [16]. Multiplexed LFAs can be made for a single sample, using hydrophobic barriers to divide and direct fluid flow into multiple assay pathways that are printed with a solid ink printer

[8]. This enables the possibility of simultaneous detection of many analytes from a single sample. Sensitive quantitative and multiplexed detection can be achieved using the conductimetric and optical approaches investigated in this thesis.

1.5. Gold Nanoparticles

Detector labels are chosen for their detectable properties and their ability to bind proteins or other molecules that target and bind analytes of interest. GNPs are the labels most commonly used in LFAs because they produce a particularly strong optical response, due to localized surface plasmon resonance (LSPR), which makes it possible to visually detect them at relatively low levels. This effect results from the metallic bonding within the GNP and its small size (on the order of tens of nanometers in diameter). When a surface plasmon is confined to a nanoparticle of a particular material and size, which is on the order of several times smaller than the wavelength of light, its free electrons participate in a collective oscillation (i.e., a localized surface plasmon) which has a natural resonant frequency (see Figure 5). The particle's optical extinction peaks at this

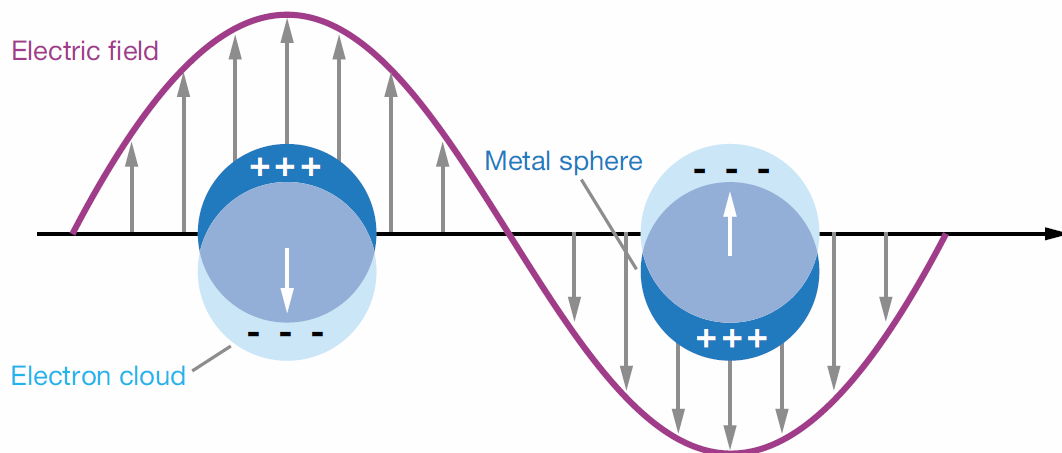


Figure 5. Visualization of a localized surface plasmon [22].

plasmon resonant frequency, which is also affected by the particle's shape and the medium that it is suspended in. Additionally, electric fields near the particle's surface are greatly enhanced, but attenuate rapidly with distance (though there is still some far-field enhancement). LSPR also occurs in other metals, but it produces a response in the visible spectrum only in nanoparticles made from noble metals. Gold is often chosen over other noble metals because it is less reactive and has more ideal chemical workability [23].

A sharply peaking optical extinction spectrum means that light at the wavelength of the peak is very effectively absorbed by the nanoparticle. At its peak wavelength, a GNP is capable of absorbing on the order of 10^5 - 10^6 times more light than a normal dye molecule. For GNPs, the peak absorbance lies in the green part of the visible spectrum (~495-570 nm), which gives rise to intense red colors for smaller particles. As particle size increases the color shifts to longer wavelengths and as particles become sufficiently

large, the peak absorbance shifts into the infrared. This results in purple then blue colors.

Figure 6 shows the colors of small to large GNPs.

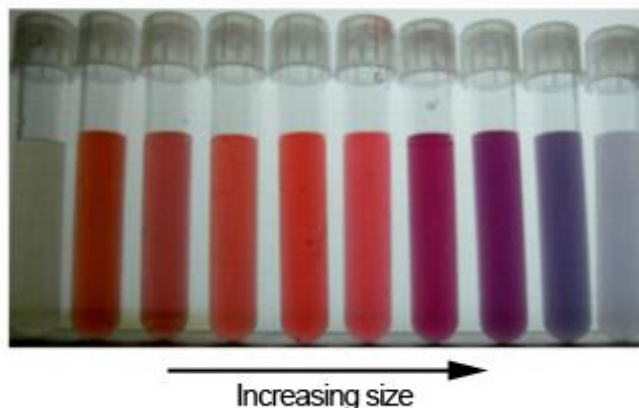


Figure 6. Colors of GNPs of different sizes (credit: Irawati Kandela).

Antibodies can be conjugated to labels covalently with a direct linkage between the surface of the label and the antibody, via adsorption (at the isoelectric point of the antibody through electrostatic interaction), or by using adapter molecules. Covalent attachment offers an advantage over adsorption because it prevents the competitive displacement of attached antibodies by other constituents in the sample, which can occur for adsorbed antibodies. Antibodies have structural components which are termed the fragment crystallizable (Fc) and the fragment antigen-binding (Fab) regions. Ideal conjugation involves the covalent attachment of the Fc region to the label, leaving the antigen-binding Fab region available, in a one-to-one ratio of antibody to label (which enables direct quantification when all sites have bound analytes) [24].

In a NC membrane, labels that are small and spherically shaped work best because they flow freely through the membrane [15]. With GNPs there is little to no impedance on particle mobility as they flow through the membrane [25]. This provides more optimal transport through the membrane, which leads to better mixing with the sample and more complete deposition of detectors downstream in the detection and control regions.

In addition to being highly visible, and well suited for both conjugation with antibodies and transport through NC membranes, GNPs also increase the conductivity of the medium they are suspended in by contributing charge carriers. This makes it possible to detect GNPs by measuring this effect.

2. MATERIALS AND METHODS

2.1. Membrane Preparation

Backed NC, Hi-Flow Plus 135 (catalog number: HF13504XSS), was purchased from EMD Millipore and used as the membrane in all experimental applications for this thesis. This particular membrane was chosen because it lies in the middle of the range of what is available for both sensitivity and speed (flow time is 135 ± 34 seconds per 4 cm). Additionally, the NC in this product exists as a 135 μm thick layer on a 100 μm thick transparent polyester backing, which greatly improves its mechanical properties (it is brittle and easily broken, without the backing) [25].

2.1.1. Printing Solid Ink Patterns

Testing areas of the NC membrane were bounded by hydrophobic barriers that were printed using a Xerox ColorQube 8570 (shown in Figure 7). Rather than using a



Figure 7. Xerox ColorQube 8570 solid ink printer used for printing hydrophobic wax barriers on nitrocellulose.

liquid ink like most inkjet printers or toner powder like a laser printer, this printer uses a waxy solid ink made from a proprietary blend of polyethylene and fatty amide waxes, resin, and dyes [26]. This type of ink is a solid at ambient temperature, but undergoes a phase change and becomes a liquid when it is heated sufficiently. A piezoelectric inkjet printhead with a high operating temperature ejects ink as a liquid, droplets (with volume on the order of ~65-110 pL) of which solidify into a printed pattern almost immediately upon contact with the cooler surface of a printing medium (e.g., paper) [27] [28]. Since the ink freezes on contact with the printing medium, very little is wicked into it (even if it is porous, like paper), resulting in well-defined lines and vibrant colors. When printing on NC, the structural integrity provided by the polyester backing, makes it possible to print without damage to the membrane or risk of jamming in the printer.

2.1.2. Reflowing Solid Ink to Create Complete Hydrophobic Barriers

Because very little wicking perpendicular to the plane of the membrane occurs before cooling, it is necessary to heat the NC after printing on it to reflow the solid ink so that it is wicked through the entire thickness of the membrane to create a complete hydrophobic barrier (which fluid cannot pass underneath). Figure 8 shows an illustration of before and after heating states for a printed-on NC membrane, and demonstrates the necessity for complete penetration of the hydrophobic barrier through the membrane. A

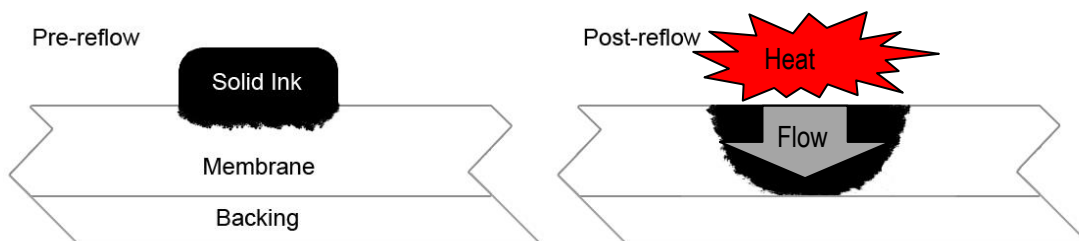


Figure 8. Illustration of pre- and post-heating states for a printed-on NC membrane. This cross-section is perpendicular to the plane of the membrane and the printed line.

procedure that was developed by Lo, et al., was followed to achieve consistent results when melting solid ink into NC membranes [29].

Patterns were designed using the free, open source, scalable vector graphics editor, Inkscape. After patterns were printed on sheets of NC with solid ink, they were heated on an electronically controlled hot plate (IKATHERM C-MAG HP 10) for 5 minutes at 120 °C (after allowing the hot plate to preheat for 10 minutes). The temperature and heating times recommended by Lo, et al., were confirmed to be sufficient to create complete hydrophobic barriers in the membrane (Figure 9

demonstrates the affect that heating has on solid ink penetration into the membrane); much higher temperatures and longer times were found to result in a decrease in membrane surface energy which hindered wetting.

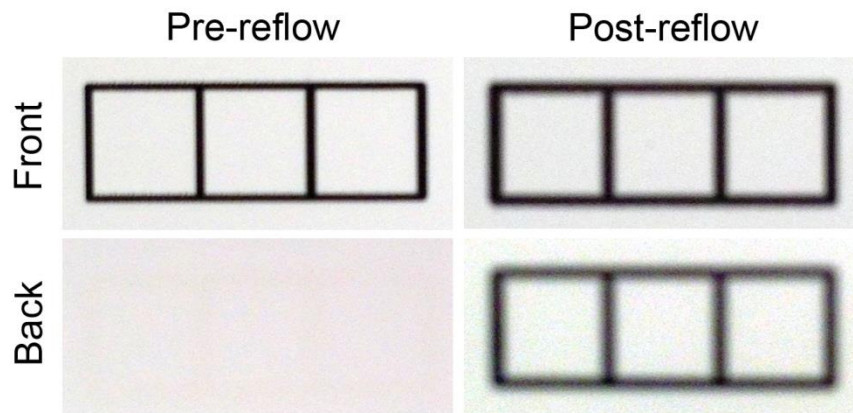


Figure 9. Photos of a solid ink pattern on a NC membrane before and after heating. It is almost impossible to see the pattern through the membrane in the before photo (due to very little penetration and the high opacity of NC).

Figure 10 shows a photo of a hot plate test with a print on a sheet of regular printer paper for demonstrative purposes. Though the hot plate worked well for preparing

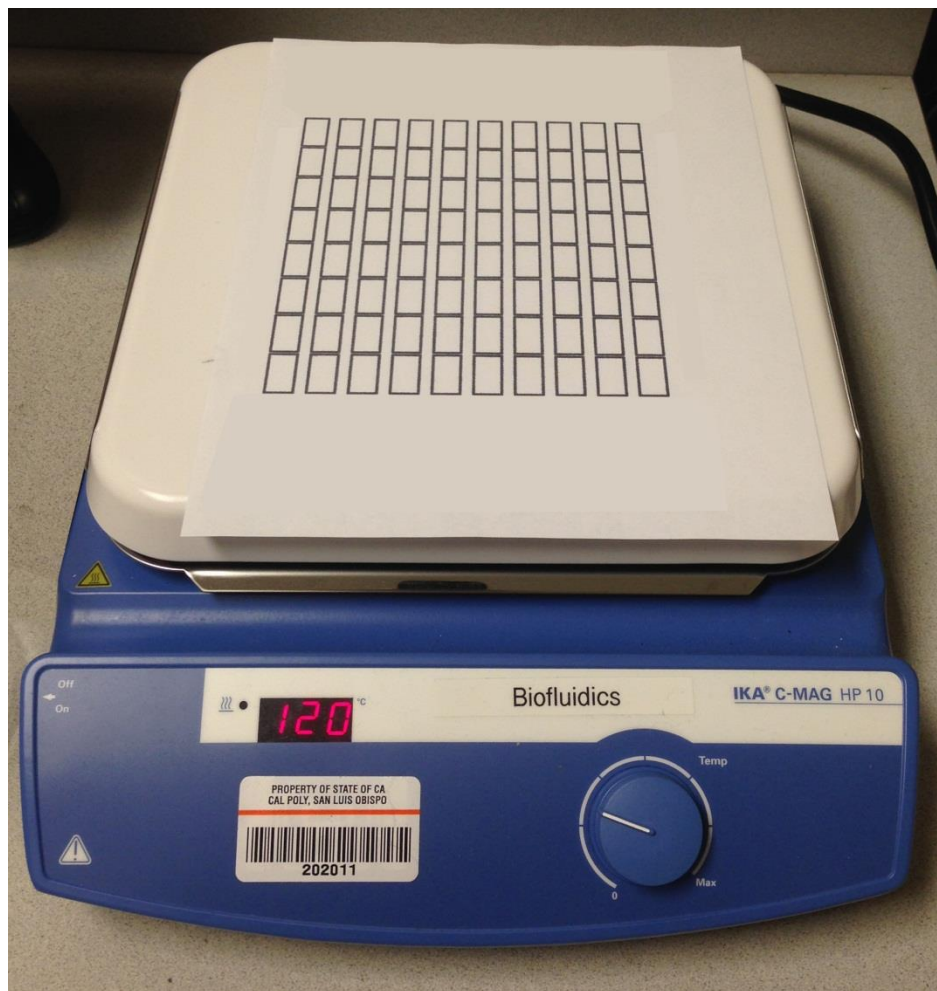


Figure 10. IKA C-MAG HP 10 digitally controlled hot plate used for reflowing solid ink to create complete hydrophobic barriers through the depth of membranes.

NC membranes for the experiments that were performed, variations in temperature were observed at different regions of the surface of the hot plate (the perimeter was cooler than the central area). Additionally minor warping of the polyester backing occurred during heating, which caused some areas to partially lift off the surface of the hot plate, resulting in uneven conductive heating (polyester typically melts between 225 and 263 °C, so even though the backing does become slightly more malleable at the heating temperature, it

does not melt completely). The duration of the heating process was long enough to facilitate even solid ink reflow throughout the membrane (as it is limited by the amount of solid ink present in thin lines) [27]. However, uniform heating throughout could be achieved by using an oven rather than a hot plate to reflow the solid ink. The advantage of the hot plate over an oven is that preheating is quicker.

Spreading of molten solid ink in the membrane wasn't particularly important for the work done in this thesis, but when implementing these types of hydrophobic barriers with more complicated assay architecture, which is necessary to define fluid reservoirs and divide and direct fluid flow through channels into reaction zones for fully functional multiplexed assays, it can be important. This spreading is a process of capillary flow in a porous material, which is described by Washburn's equation in eq. 1,

$$L = \sqrt{\frac{\gamma D t}{4\eta}} \quad (1)$$

where L is the distance that a liquid, with surface tension γ and viscosity η , penetrates a porous membrane with average pore diameter D in time interval t [30]. If the temperature is assumed to be constant, all of the parameters in eq. 1, except for t , are fixed so if the amount of solid ink is not limiting, the heating time interval determines the spreading distance (in the membranes prepared in this thesis, the amount of solid ink was a limiting factor, so the spreading of the molten solid ink reached a maximum before the heating time interval ended). It follows naturally that the width of a hydrophobic barrier can be related to the width of a printed line by the expression in eq. 2,

$$W_B = W_P + 2L \quad (2)$$

where W_B is the width of the barrier after melting, W_P is the width of the original printed line and L is the distance that the molten solid ink spreads from the edge of the printed line. The width of a channel defined by two parallel hydrophobic barriers can be predicted using eq. 3,

$$W_C = W_G - 2L \quad (3)$$

where W_C is the width of the channel, W_G is the width of the gap between the original parallel printed lines before heating, and L is again the distance that the molten solid ink spreads from the edge of each printed line [27].

2.1.3. Concentration Factor and Equivalent Target Concentration

In LFAs, there is an inherent concentration factor due to properties of the NC, dimensions of the capture regions, sample volume, and size and concentration of the conjugated detectors.

Concentration is increased from the sample to the detection region due to volume reduction. Though these values depend on varying requirements for different situations, a typical sample volume can be assumed to be 135 μL , and a test or control line is typically 1 mm long. A typical NC membrane is approximately 1 cm wide and 135 μm thick. The

volume of the detection region is therefore approximately 1.35 μL (1 mm x 10 mm x 0.135 mm). Additionally, because the NC membrane is porous, its porosity (the fraction of void to total volume in the membrane) must be taken into consideration. Porosity can be assumed to be 70% for the NC used. Using eq. 4, the effects that volume reduction and porosity have on the concentration of analyte in the sample can be calculated:

$$C_f = C_i \frac{V_i}{V_f P} \quad (4)$$

In this expression, C_f is the final concentration, C_i is the initial concentration, V_i is the initial volume, V_f is the final volume, and P is the porosity.

Another important consideration is the loading capacity of the membrane for the type of antibody which is immobilized – this determines the number of antibodies that can be immobilized in the detection and control regions. A membrane's protein binding capacity is determined, primarily, by the amount of internal polymer surface area available for immobilization. Surface area is affected by pore size, porosity, and thickness; it decreases nonlinearly with pore size, increases nonlinearly with porosity, and increases linearly with thickness. The internal surface area of porous structures is normally reported in units of m^2/g . Basis weight of a membrane is its planar area density in g/m^2 . The surface area ratio is obtained by multiplying the internal surface area and the basis weight. NC membranes used in LFAs typically have surface area ratios in the range of 50 – 200. The loading capacity of a protein on a surface area depends on its compactness of structure and its Stokes radius. For IgG, the loading capacity is

approximately $1 \mu\text{g}/\text{cm}^2$. The loading capacity can be multiplied by the surface area ratio to determine the approximate IgG binding capacity of the membrane to be $50 - 200 \mu\text{g}/\text{cm}^2$. If the membrane is 1 cm wide and the test line is 1 mm long, the amount of IgG that can be bound is $5 - 20 \mu\text{g}$. IgG's molecular mass is typically $\sim 160 \text{ kDa}$, so the concentration (found by dividing total mass of IgG by its molecular mass and the detection region volume, $1.35 \mu\text{L}$) is approximately $2.3 \times 10^{-5} - 9.3 \times 10^{-5} \text{ M}$, which is many orders of magnitude larger than the highest expected concentration of analyte in most assays. Therefore, protein binding capacity is usually not an issue in assay design (and doesn't affect the concentration factor) [15].

Additional potential influencing factors are the protein binding capacity of the detector labels and the concentration of detector labels, relative to analyte. The surface density of protein adsorbed to GNPs can be estimated (for electrostatic conjugation) using eq. 5:

$$\Gamma = \frac{d(n_p - n_s)}{\frac{dn}{dc}} \quad (5)$$

where d is average protein layer thickness, n_p is average protein layer refractive index, n_s is the refractive index of the buffer solution, and dn/dc is the specific refractivity of the layer of adsorbed protein [31]. Protein layer thickness and refractive index can be determined via optical extinction measurements of the LSPR spectrum of GNPs to be approximately 13 nm and 1.377, respectively, for IgG adsorbed to 50 nm diameter GNPs. The refractive index of the buffer, phosphate buffered saline (PBS), can be assumed to be

1.333 [32]. Specific refractivity can be measured for IgG in bulk solution to be 0.188 cm³/g [33].

The average number of protein molecules adsorbed to the surface of a single GNP can be estimated with eq. 6:

$$N = \frac{4\pi r^2 \Gamma}{m} \quad (6)$$

where r is the radius of the GNP, Γ is the protein density on the surface of a GNP (of radius, r), and m is the molecular mass of the protein. For a GNP with a radius of 25 nm, the protein surface density is ~ 3 mg/m², and for IgG, the molecular mass is ~ 160 kDa. Thus, the number of IgG molecules adsorbed to a GNP of this size is ~ 90 . Using a smaller GNP will result in lower adsorption.

For covalent conjugation, the contact area required per IgG molecule is approximately 45 nm² [34]. Accordingly, the number of IgG molecules per 50 nm diameter GNP is ~ 170 . Again, using a smaller GNP will result in lower adsorption.

If the GNPs used for conjugation are assumed to be concentrated such that their OD = 50 (as is typical), then at the highest concentration in the range tested in this thesis, there would be roughly 10 conjugated detectors for each analyte molecule; at the lowest, there would be nearly 2.6×10^5 detectors per analyte [34]. Since there are many more detectors than analyte molecules, it is unlikely for a detector to bind multiple analyte molecules, even though it has the capacity to do so via many sites. Therefore, protein binding capacity of GNPs doesn't usually affect the concentration factor, either.

Consequently, the factor that the actual label concentration is greater than the equivalent target molecule concentration for the supplies that were used is ~143. This factor, hereafter referred to as k , is used to report GNP concentrations in equivalent target concentrations.

2.2. Optical Detection

2.2.1. Dye and GNPs

Dye was substituted for GNPs wherever possible in optical experiments in order to reduce costs. GNPs with a diameter of 50 nm were purchased from Sigma-Aldrich in a concentration of 3.51×10^{10} particles/mL (low for optical detection) at a quantity of 25 mL, as a stabilized suspension in 0.1 mM phosphate buffered saline (PBS) (SKU: 753645-25ML). The wavelength of maximum absorption for GNPs of this size is ~535 nm, and the molar extinction coefficient is $\sim 1.72 \times 10^{10} \text{ M}^{-1} \text{ cm}^{-1}$ [35]. Though some of the colloidal gold was concentrated for comparison purposes, it would have been cost prohibitive to purchase enough to concentrate and achieve the entire range necessary for optical LOD characterization.

The dye that was used was the disodium salt, erythrosine, which has maximum absorption at a wavelength of ~530 nm and a molar extinction coefficient of $\sim 1.02 \times 10^5 \text{ M}^{-1} \text{ cm}^{-1}$ at that wavelength [36]. Erythrosine was chosen because its peak absorbance wavelength is spectrally close to the peak absorbance wavelength of the GNPs that were used (see Figure 11). A comparison of molar extinction coefficients shows that at the

same absorbance and measured with the same optical path length, a single GNP absorbs roughly as much light as 1.67×10^5 molecules of erythrosine.

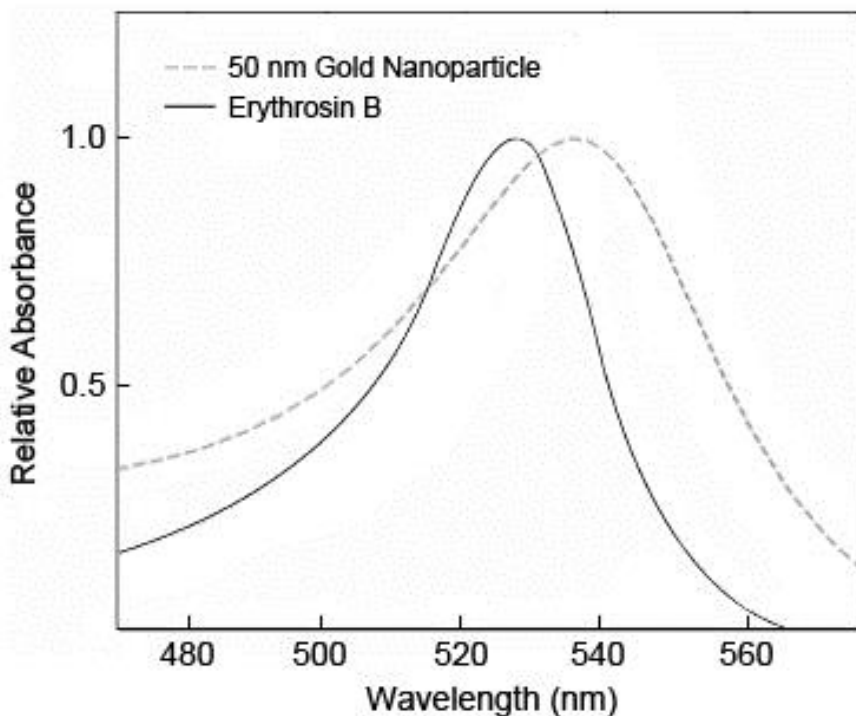


Figure 11. Comparison of absorbance spectra of GNPs and erythrosine dye (approximate) [37].

Serial dilutions were prepared from the full-strength dye, starting at $(1.67 \pm 0.17) \times 10^{-3}$ M and ending at $(2.17 \pm 0.22) \times 10^{-6}$ M, with a total of 13 different sample concentrations, each consecutive concentration $1/1.74$ of the previous. A Thermo Scientific brand Finnpiptette F2 100-1000 μ L single channel pipette was used with 1000 μ L pipette tips to perform these dilutions. According to the manufacturer, this pipette has a maximum systematic error of ± 8 μ L and a maximum random error of ± 3 μ L [38].

Deionized (DI) water (18.4 M Ω -cm at 25°C) was used to dilute the dye, with 1000 μ L of the previous sample and 740 μ L of DI water for each dilution.

The full-strength GNP suspension was concentrated to bring it into the optical detection range. A 2.0 mL flat top microcentrifuge tube was filled with 1000 μ L of GNP suspension. A centrifuge (Eppendorf 5415 C) was used with an 8 cm radius rotor at 4700 rpm for an acceleration of 2000g for 30 minutes, in accordance with recommendations from Cytodiagnosics (see APPENDIX E) [39]. After centrifugation, 875 μ L of supernatant were removed, and the remainder was vortexed to resuspend particles, resulting in a final product eight times the concentration of the original.

2.2.2. *Visual*

For detection with the unaided eye, NC membranes were prepared by printing eleven 1 cm \times 2 cm rectangles with 1 mm line width, and heating according to the protocol described above. One rectangle was loaded with DI water as a blank, and the remaining ten were loaded with samples of dye (see Table 1).

Table 1. Concentrations of Dye Used in Visual Detection Limit Determination

Sample	Erythrosine Concentration (M)
0	0
1	$(1.66 \pm 0.17) \times 10^{-3}$
2	$(9.59 \pm 0.97) \times 10^{-4}$
3	$(5.51 \pm 0.55) \times 10^{-4}$
4	$(3.17 \pm 0.32) \times 10^{-4}$
5	$(1.82 \pm 0.18) \times 10^{-4}$
6	$(1.05 \pm 0.10) \times 10^{-4}$
7	$(6.01 \pm 0.60) \times 10^{-5}$
8	$(3.45 \pm 0.35) \times 10^{-5}$
9	$(1.99 \pm 0.20) \times 10^{-5}$
10	$(1.14 \pm 0.11) \times 10^{-5}$

Samples were dispensed in volumes less than the volume of the sample area of the membrane, using a Thermo Scientific brand Finnpiette F2 1-10 μL single channel pipette with 10 μL pipette tips. The purpose of this was to prevent fluctuations in dispensed volume from affecting dye concentrations in the membrane (if there were more than enough sample to completely fill the sample area, after drying the final concentration would be higher than it would otherwise be). Volumes of samples 4, 5, and 6 were 4.85 μL , 5 μL , and 5.5 μL , respectively, and the remaining samples were 6 μL . The volume to be used for sample 4 was determined by calculating the volume required to fill approximately 30% of the membrane (the sample area after reflowing the wax, the membrane thickness, and the porosity, were used for this calculation, i.e., $19 \text{ mm} \times 9 \text{ mm} \times 0.135 \text{ mm} \times 0.70 \times 0.30 = 4.85 \mu\text{L}$). After dispensing, this was observed to be lower

than desired, so the volume was increased for the next three samples until it was found that 6 μL provided the desired coverage, with sample 7. Higher dye concentrations were used with samples 1, 2, and 3, to provide a wider test range. Figure 12 shows the visual test membranes loaded with dye.

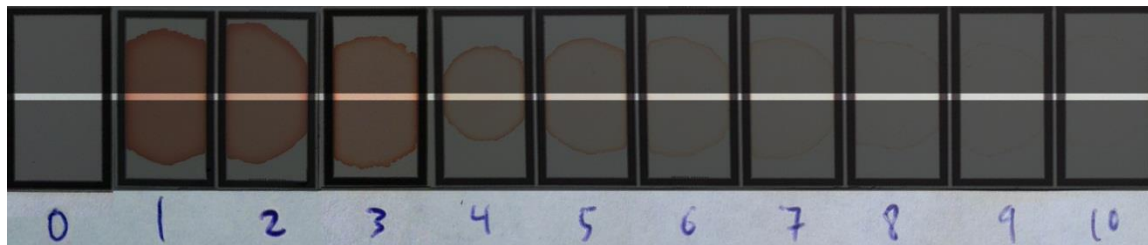


Figure 12. Samples used for visual detection limit determination. The tops and bottoms of the membranes are darkened in this image to highlight the detection areas viewed by test subjects. The darkened areas were completely obscured during testing.

Black construction paper was used to obscure parts of the membrane during visual testing in order to limit the visible portion to the shape and area of what would be visible during evaluation of a typical LFA. This was achieved by creating an opening approximately 1 cm wide and 1.64 mm high, with a piece of blank NC showing approximately 3 mm below it to provide a blank reference. A window was cut above the sample area and covered with a flap of black construction paper to provide means to determine the sample number, via numbers marking each sample, for the test administrator. Figure 13 shows the construction paper construct that was used, with the sample number window open and closed.

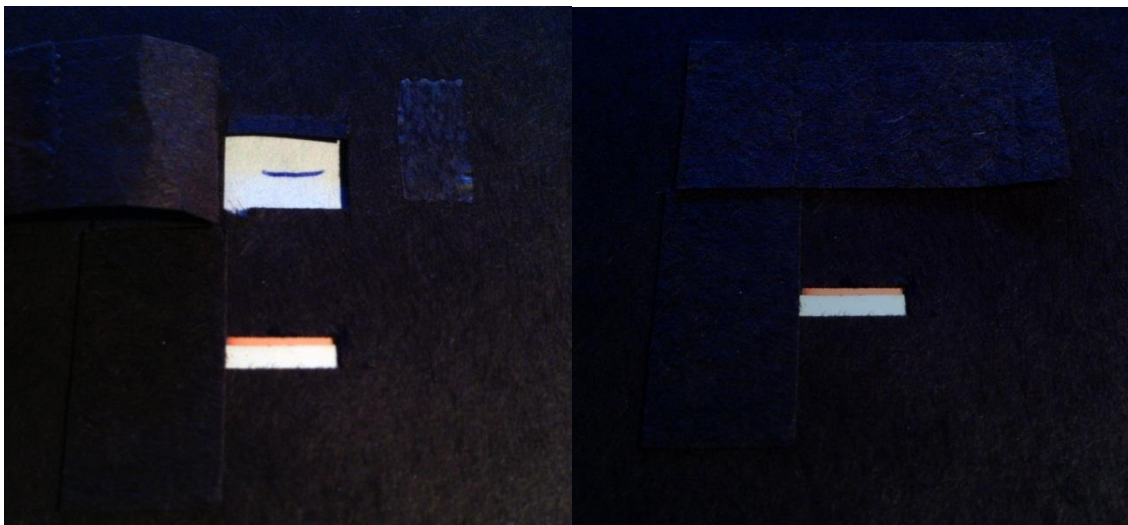


Figure 13. Black construction paper used to mask the samples on the membrane to the shape and area that is found with typical LFAs. Left, window open, showing sample number; right, window closed.

It was found that when viewing a sample from directly above, the edge of the NC and backing were visible as a dark line, which gave a sense of contrast, leading to false enhancement and reported positives even when there was no dye present. The size and shape of the opening through which the sample was viewed was chosen so that when viewed at a 45° angle from the normal of the membrane, and perpendicular to the visible edge of the reference NC, a sample area equivalent to one of 1 cm wide and 1 mm high was visible, and the edge of the reference NC was not visible. The black construction paper on the opposing side was also used to prevent a visible edge (see Figure 14).

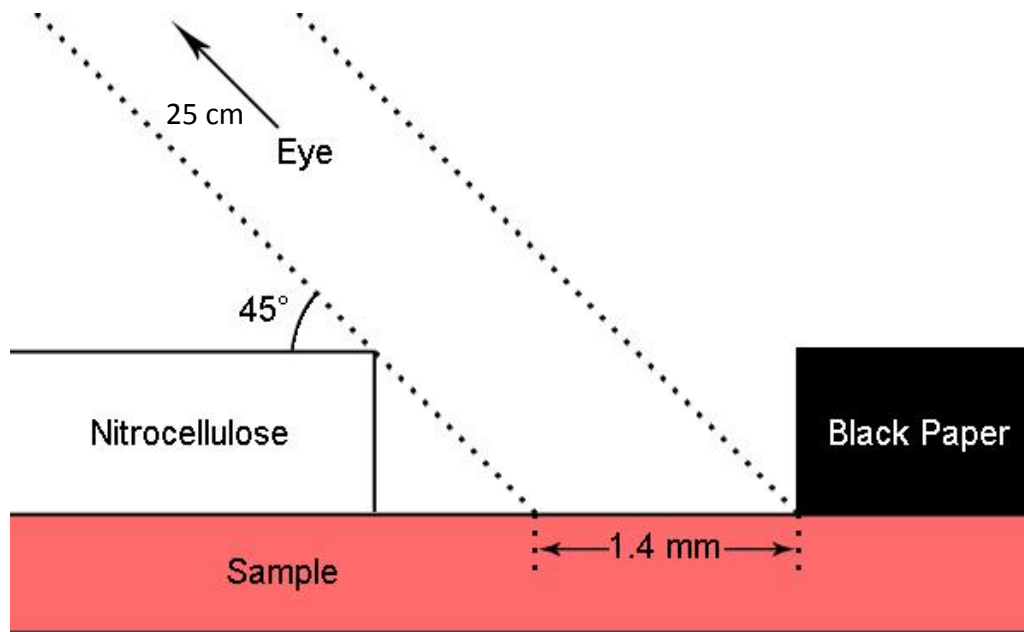


Figure 14. Diagram of construction paper, nitrocellulose reference, and sample in membrane, showing viewing angle and projected sample height.

Individuals were trained to view samples from the correct orientation, and at a distance of approximately 25 cm (from eye to sample). Consistent lighting conditions were used, under fluorescent lamps, in a setting where no shadows were cast on the sample area. Seven individuals were tested and each sample was tested in triplicate with presence reported as either positive or negative, according to the protocol used by Guillén, et al. [40].

2.2.3. Mobile Electronic Device Image Analysis

2.2.3.1. Spectral Sensitivity:

The image analysis technique that was used was developed with multiplexed assays in mind. The platform used for LOD evaluation was laid out as a 10×12 matrix of 120 $1 \text{ cm} \times 2 \text{ cm}$ rectangles with 1 mm line width, surrounded by corner markers and center markers for rows and columns to facilitate automated processing. The rectangle design was chosen to provide sample areas similar to what is found with LFAs (i.e., 1 cm width), while also enabling samples to be dispensed without completely occupying the sample areas (which, as stated above, would result in varying concentrations according to differences in applied sample volumes). Figure 15 shows the design that was used. Since

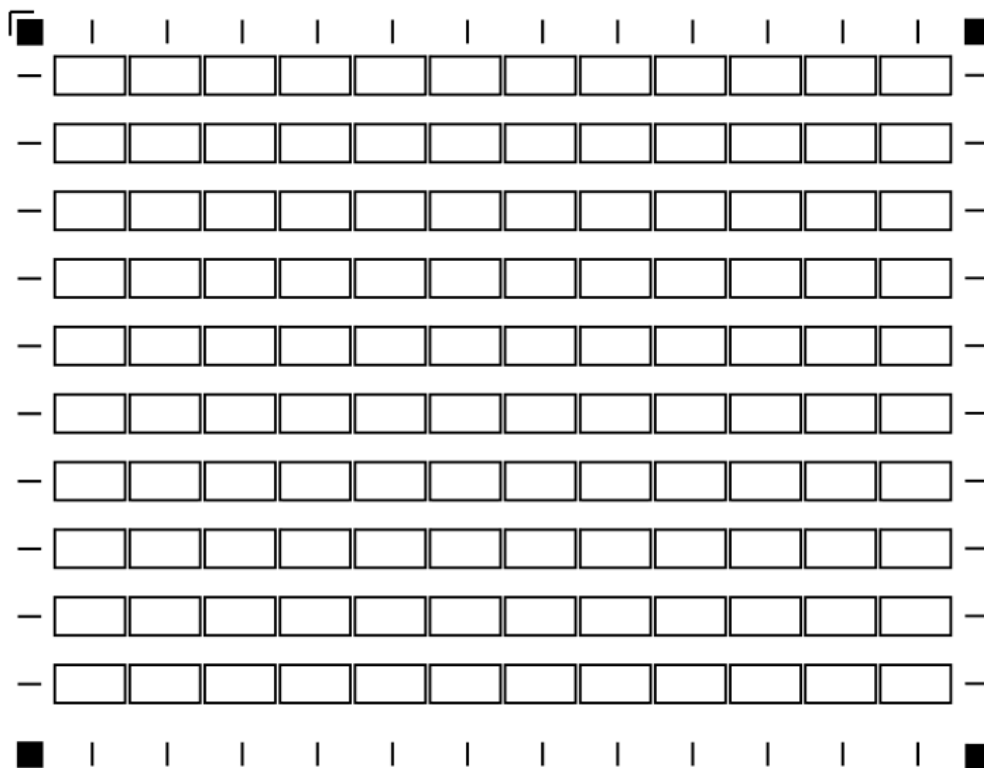


Figure 15. Sample well matrix used for LOD determination via automated image processing of photographs from MED cameras.

all sample areas are analyzed simultaneously and from the same image, it is demonstrated that designs based on this platform architecture, along with the software that was developed, can be used for multiplexed diagnostics. Note that unique white reference areas are positioned directly below each sample area.

Spectral sensitivity was determined for each of the MED cameras that were used. This was achieved with the aid of a simple home-made spectrometer based on the “Public Lab Foldable Mini-spectrometer,” the design for which was released under the CERN Open Hardware License 1.1 [41]. The design was modified by using razor blades, rather than paper, to form the slit where light enters the spectrometer (which provide for a

narrow opening with very clean edges) and a 1000 line/mm linear diffraction grating rather than a piece of a DVD (see Figure 16).

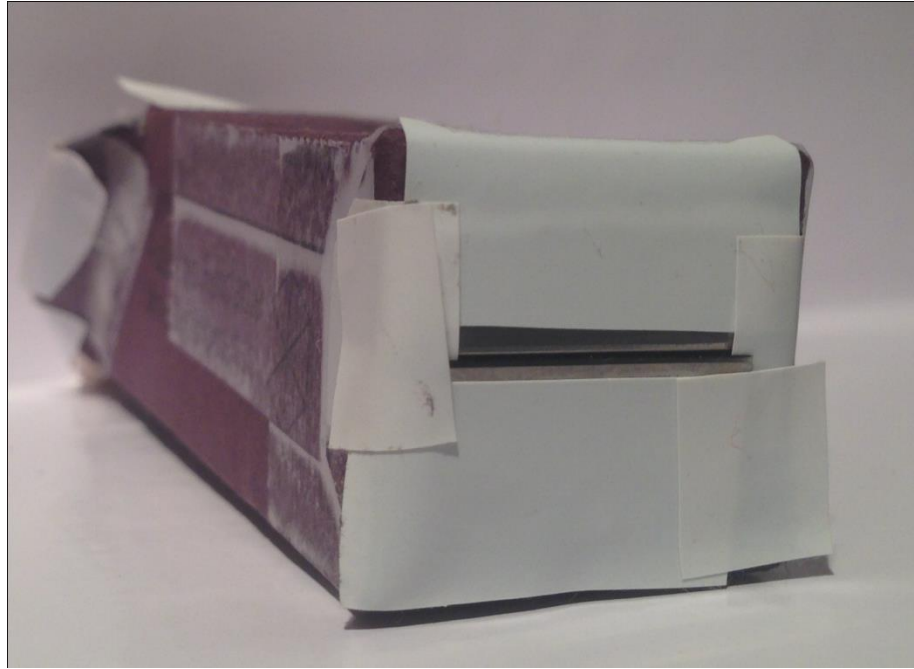


Figure 16. Front view of spectrometer, showing slit, with razor blade edges, where light enters the system.

The spectrometer was attached to MEDs using tape. Figure 17 shows the rear view of the spectrometer, with the diffraction grating visible. The spectrometer was

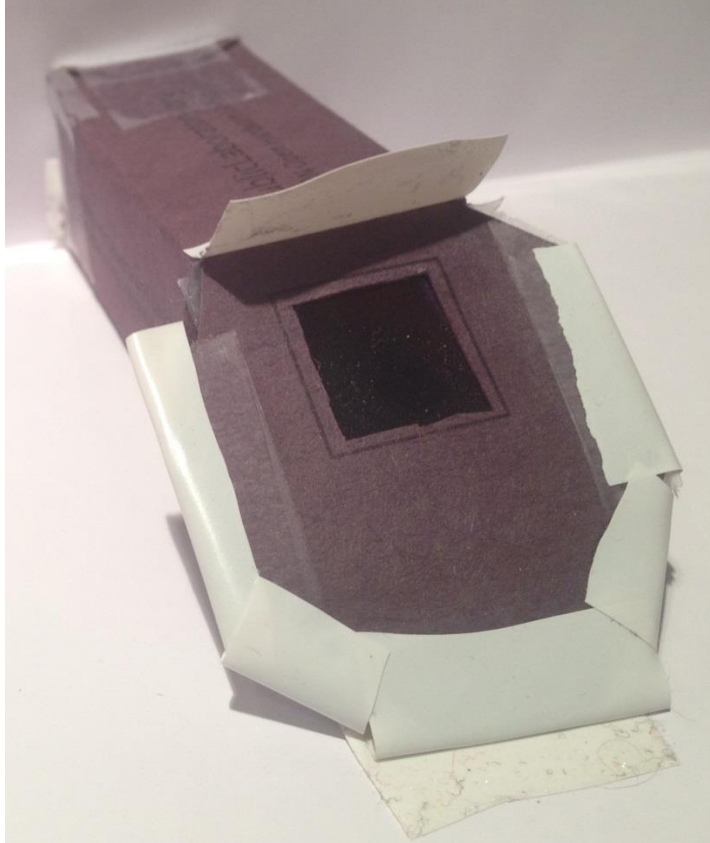


Figure 17. Rear view of spectrometer, showing tape used to attach it to MEDs and the 1000 line/mm diffraction grating.

designed to spread a spectrum across the long axis of a camera sensor. Depending on the camera used, a resolution as good as ~ 0.3 nm/pixel can be achieved. Figure 18 shows the spectrometer attached to a MED.

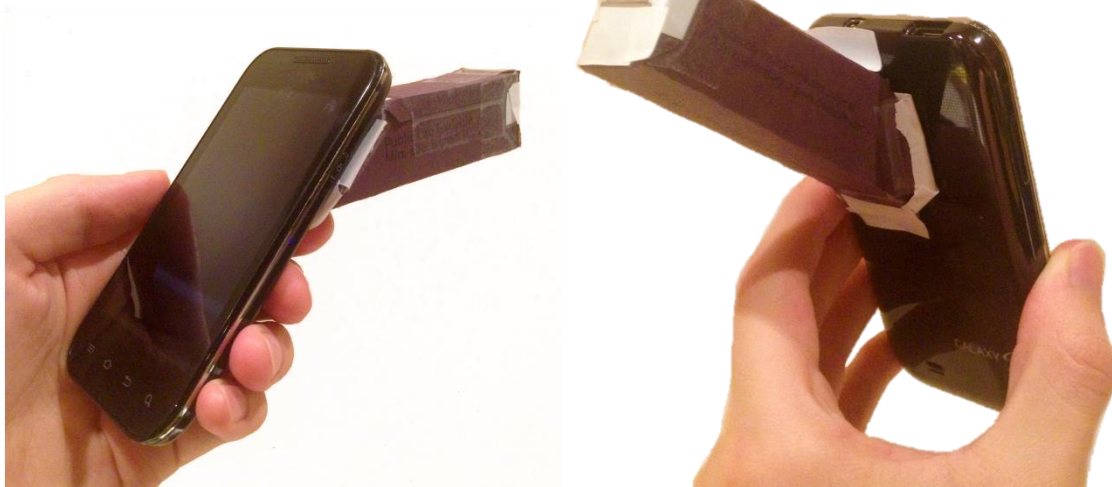


Figure 18. Spectrometer attached to a smartphone in preparation for determining the spectral sensitivity of its camera sensor. Left, front view of the smartphone and spectrometer; right, rear view.

It was necessary to calibrate the spectrometer to determine which pixels corresponded to which wavelengths of light. Calibration was achieved using the prominent 436 nm and 546 nm mercury emission lines of a compact fluorescent lamp as reference points, and scaling linearly, to map pixels to wavelengths in the visible spectrum. Sensitivity was then assessed by capturing the spectrum of a tungsten filament incandescent lamp, and the peak was determined for each color channel.

2.2.3.2. MATLAB:

Each column of the test platform was filled with 10 samples of the same concentration. For the blank and the samples containing dye, a dispensed volume of 6 μL was used. In order to make a comparison to samples containing GNPs, an 8 \times

concentrated GNP suspension (final OD = 8), which was prepared according to the method described above, was used. Since only a small quantity of the concentrated GNP suspension was prepared, a dispensed volume of 4 μL was used. Dye was used for testing in this application because it is available at higher concentrations and at a lower price point than GNPs. Table 2 shows the samples tested and their concentrations.

Table 2. Erythrosine Samples and Their Respective Concentrations Used in LOD Evaluation with MED Images

Sample	Concentration (M)
1	$(9.59 \pm 0.97) \times 10^{-4}$
2	$(5.51 \pm 0.55) \times 10^{-4}$
3	$(3.17 \pm 0.32) \times 10^{-4}$
4	$(1.82 \pm 0.18) \times 10^{-4}$
5	$(1.05 \pm 0.10) \times 10^{-4}$
6	$(6.01 \pm 0.60) \times 10^{-5}$
7	$(3.45 \pm 0.35) \times 10^{-5}$
8	$(1.99 \pm 0.20) \times 10^{-5}$
9	$(1.14 \pm 0.11) \times 10^{-5}$
10	$(6.53 \pm 0.67) \times 10^{-6}$
Blank	0
GNP	$(4.66 \pm 0.47) \times 10^{-10}$

Image processing software was developed using MATLAB (APPENDIX A). After capturing an image of the sample matrix, which can be in any orientation, the location of the file to be used is collected with a GUI and the file is read into the program (see Figure 19). The image is displayed and the user marks the corners by clicking the

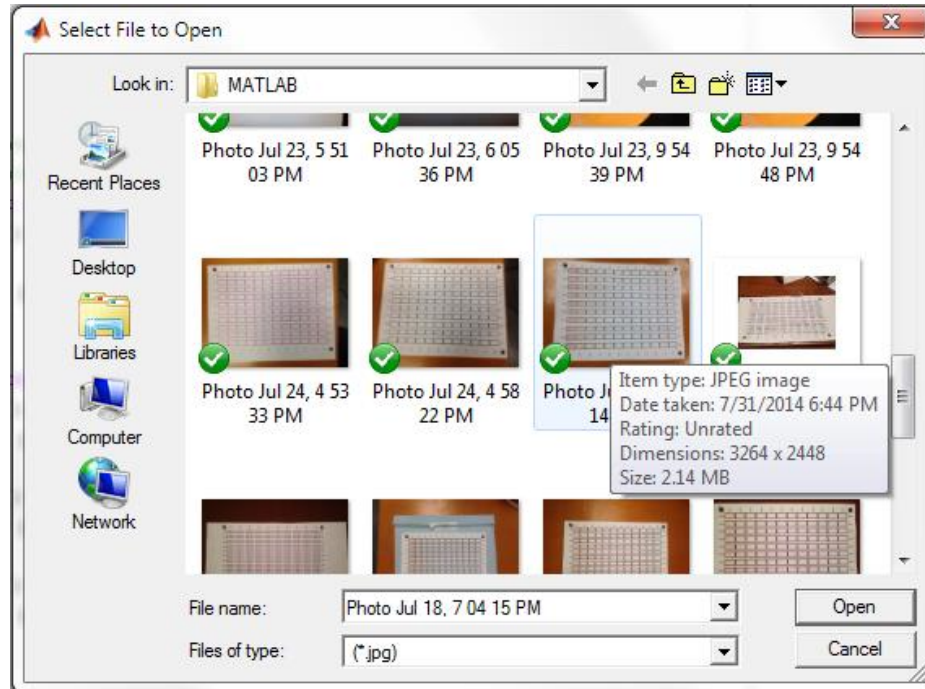


Figure 19. File import for image processing with graphical user interface.

centers of the squares on each (which is the only interaction the user has with the program other than choosing a file to process). The first square that is marked must be the primary corner, which has a right-angle symbol marking its outside corner; the order does not matter for the remaining three. Figure 20 shows the corners being marked on an unprocessed image. The processing algorithm then determines the number of corners

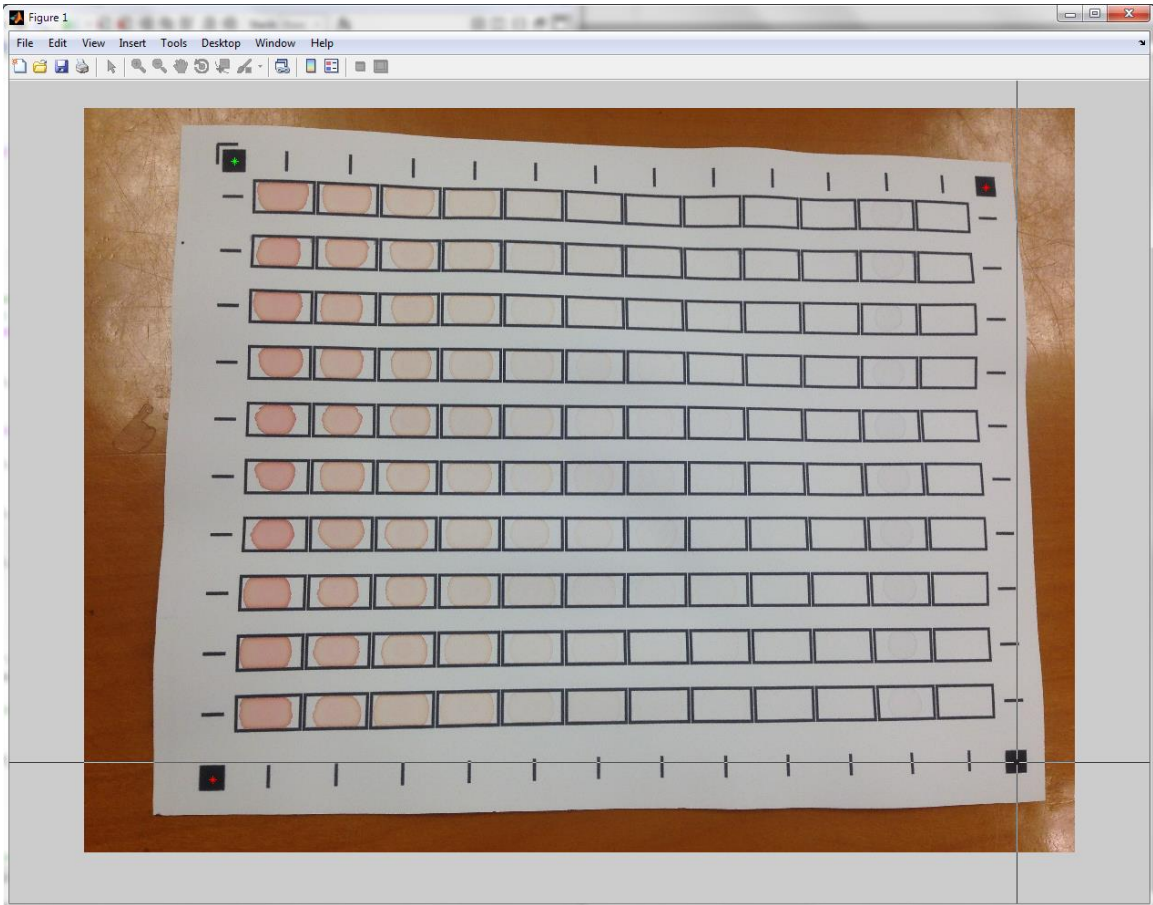


Figure 20. Unprocessed image with three corners marked and the fourth selected to be marked. Rows contain samples of the same concentration, the 10 left columns contain samples of decreasing dye concentrations, the 11th column from the left contains 8 \times concentrated GNP suspension, and the 12th column contains DI water as a blank.

which are to the left of the primary marker, and how far they are from it, and uses this information to calculate the rotation angle required to make the line connecting the two left corners parallel to vertical.

The image is then cropped to the smallest rectangle that can contain all of the corners to reduce its size and decrease the time and memory required for remaining processing. Next, a projective transform is applied to the quadrilateral with vertices

located at the corners of the sample matrix in order to eliminate skew and make a rectangle. The image is again cropped to remove irrelevant information.

The horizontal and vertical ticks which mark the centers of each column and row of the sample matrix are processed linearly to determine the sample and reference areas to collect data from. In order to accomplish this, the image is converted from RGB to grayscale. Next, a gray threshold is determined and the grayscale image is converted to a binary image and then inverted. All objects containing fewer pixels than 1% of the smallest dimension are removed. Remaining objects are then dilated. Tick mark locations on the top and bottom horizontals and left and right verticals are identified by moving pixel by pixel in a top-to-bottom, left-to-right fashion from corner to corner. The intersections of the centerlines of the columns and rows are then used as sample locations for data collection. Reference data is collected for each sample in the region directly below it, along the sample column line and half way between row lines. Sample pixel areas of 11×11 were used, with pixel values averaged. Figure 21 shows a geometrically processed image with column and row centerlines and reference locations marked on it.



Figure 21. Partially processed image displayed in MATLAB, with column and row centerlines (white) and reference locations (black diamonds) superimposed on it. Intersections of the white lines are sample data collection locations.

Absorbance was quantified as the negative logarithm of the ratio the intensity of light reflected from a sample region to the intensity of light reflected from its corresponding reference region (directly below), as described by eq. 7:

$$A = -\log_{10} \left(\frac{I_{sample}}{I_{background}} \right) \quad (7)$$

Reference regions were designed to be as close to their unique sample areas as possible to help compensate for the effects of possible shadows and uneven lighting across the sample matrix.

For every image that was analyzed, average absorbance values were calculated for each column and plotted against their known concentrations. A linear regression was performed to obtain a relationship between concentration and absorbance, in agreement with the Beer-Lambert law, which is defined in eq. 8 as

$$A = \epsilon lc \quad (8)$$

where A is absorbance, ϵ is the molar extinction coefficient of the absorbing particles, l is the optical path length through the sample, and c is the concentration of absorbing particles. Molar extinction coefficient and optical path length were maintained as constants (the former is specific to the absorbing particle and the latter is dependent on the membrane). Figure 22 shows a visualization of absorbance with some variables indicated.

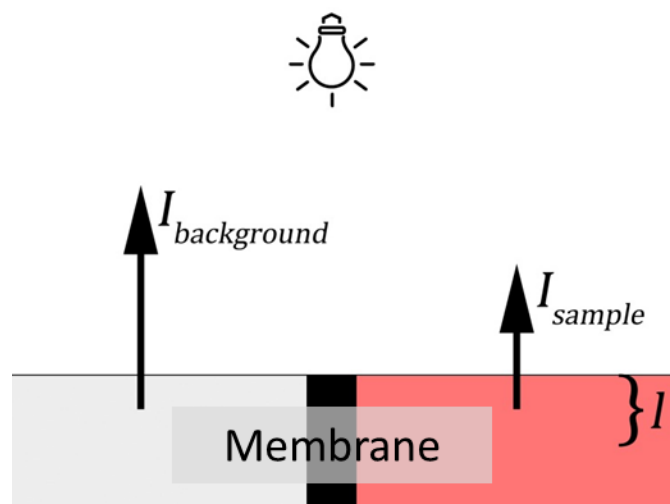


Figure 22. Visualization of absorbance. Light source, reflected light intensities, the membrane, and the optical path length are shown.

The mean and standard deviation were calculated for the blank samples on each image. The standard definition for the LOD is the mean blank signal plus 3 times its standard deviation (see eq. 9).

$$LOD = mean_{blank} + 3 * SD_{blank} \quad (9)$$

For a signal equal to the LOD value, the probability of a false positive is 1% and the probability of a false negative is 50%. To determine the LOD concentration, the equation of the line found with the linear regression is used with the calculated LOD value.

In order to convert the dye concentrations to equivalent target concentrations, the average value of the GNP column is used in the linear relationship that was found. The linear equation is used to calculate the dye concentration that provides an absorbance

equal to that of the 8× concentrated colloidal gold. Since both the dye and the colloidal gold follow the Beer-Lambert law, it is then possible to map GNP concentrations to each dye concentration using eq. 10:

$$[GNP]_{eq} = \frac{[dye]*[GNP]_{8\times}}{[dye]_{[GNP]_{8\times}}} \quad (10)$$

where $[GNP]_{eq}$ is the equivalent GNP concentration of dye, $[dye]$ is the dye concentration to be converted, $[GNP]_{8\times}$ is the 8× concentrated GNP suspension, and $[dye]_{[GNP]_{8\times}}$ is the concentration of dye that produces an absorbance that is equal to the 8× concentrated colloidal gold. Dividing $[GNP]_{eq}$ by k gives the equivalent target concentration.

Resolution, bit depth, image compression, lighting conditions, exposure, and color balance are variables that can potentially affect the data collected in images captured with different devices and at different times; however, providing that there is no over- or under-exposure, it is possible to obtain a consistent result. Devices that can capture images with more consistency in terms of lighting conditions and exposure will tend to lead to lower LODs.

The outputs of the image analysis program are an LOD value and a plot, with concentration as the independent variable and absorbance as the dependent variable, fitted with a linear regression.

2.2.3.3. Mobile Electronic Device Cameras:

Images were captured using three different mobile electronic devices, an Apple iPhone 5 (model A1429), an Apple iPad mini (model A1432), and a Samsung Galaxy S (model SCH-i500). The iPhone has an 8 megapixel main camera with an f/2.4 maximum aperture and utilizes image compression which results in an 8 bit/channel RGB JPEG [42]. The iPad and Galaxy S both have 5 megapixel main cameras with f/2.4 and f/2.8 maximum apertures, respectively, and also utilize image compression which results in 8 bit/channel RGB JPEGs.

2.2.4. *Image Analysis – Microscope*

An Olympus incident light microscope with an illumination source powered by a TH3 halogen power supply and DP12 3 megapixel camera and recorder unit were used to capture images of samples of different dye concentrations, as well as GNPs and DI on NC. Figure 23 shows the microscope setup that was used.



Figure 23. Olympus microscope with camera unit used for capturing images of samples on NC.

LODs were evaluated using objective magnifications of 5 \times and 10 \times . The light source and microscope were set up once before collecting data and left the same for all testing. The white balance and exposure were manually set for the camera unit and kept constant throughout testing. Using this setup, it was possible to achieve highly consistent lighting conditions.

Test cards were prepared according to the membrane preparation protocol described above. Each card was designed to hold 10 samples of the same concentration. The geometric properties of the sample wells were the same as those which were used

elsewhere in this project (i.e. 1 cm × 2 cm rectangles with 1 mm line width). Figure 24 shows an example of a test card that has been loaded with a sample. Dispensed volumes

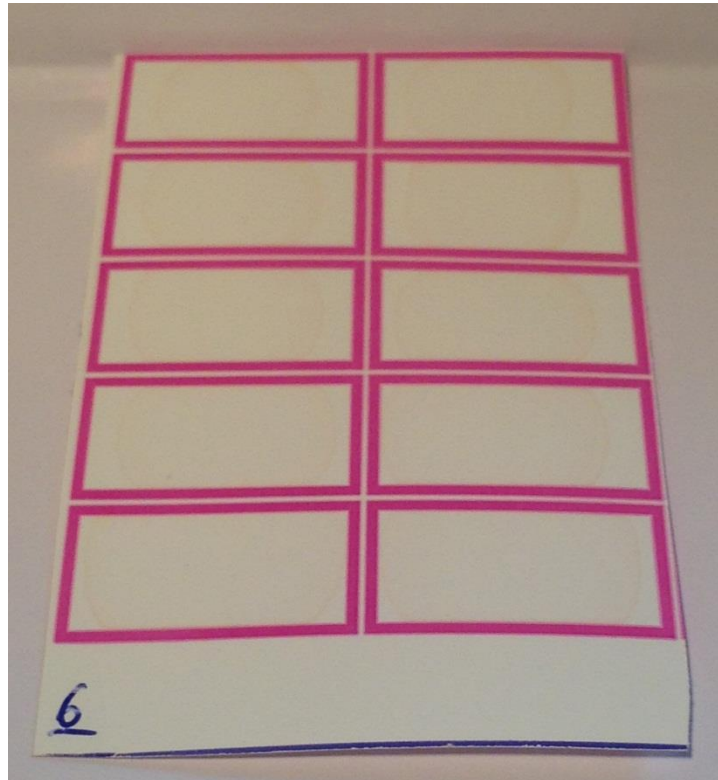


Figure 24. Test card used for collecting data with microscope, loaded with dye sample number 6.

of 5 μL for all dye and DI samples, and 2.5 μL for the 8 \times GNP suspension were used.

Eleven dye samples were tested, along with one DI, one GNP, and plain NC.

Table 3 shows samples and their respective concentrations. Each sample on each test

Table 3. Samples and Concentrations Used With Microscope LOD Evaluation

Sample	Concentration (M)
1	$(9.59 \pm 0.97) \times 10^{-4}$
2	$(5.51 \pm 0.55) \times 10^{-4}$
3	$(3.17 \pm 0.32) \times 10^{-4}$
4	$(1.82 \pm 0.18) \times 10^{-4}$
5	$(1.05 \pm 0.10) \times 10^{-4}$
6	$(6.01 \pm 0.60) \times 10^{-5}$
7	$(3.45 \pm 0.35) \times 10^{-5}$
8	$(1.99 \pm 0.20) \times 10^{-5}$
9	$(1.14 \pm 0.11) \times 10^{-5}$
10	$(6.53 \pm 0.67) \times 10^{-6}$
11	$(3.75 \pm 0.84) \times 10^{-6}$
Blank (DI)	0
GNP	$(4.66 \pm 0.47) \times 10^{-10}$
Reference (plain NC)	0

card was imaged individually. In order to collect data for a particular sample, pixel values for the color channel of interest were averaged over the entire image area ($\sim 1.28 \text{ mm}^2$ for $5\times$ and $\sim 0.32 \text{ mm}^2$ for $10\times$).

Since it was possible to keep the lighting conditions and camera settings consistent throughout testing, it was only necessary to collect reference data once (rather than for each sample like with MED images), after allowing the lamp and camera unit to warm up for 20 minutes.

A simple program was written in MATLAB (APPENDIX B) to automate the process of collecting data from captured images. All files were saved into one directory which was selected to input to the program. The files were then processed and a single cell matrix with two columns containing the name and measured value for each file was output. Absorbance was computed in the same way as with MED images, using eq. 7, with $I_{background}$ equal to the average reference value and used for all samples. LOD was determined using eq. 9, and equivalent GNP concentrations were determined using eq. 10.

2.3. Conductance Based Detection

The conductimetric approach was hypothesized to be capable of detection at a lower level than optical methods, in part because it tests samples through their volume, while, due to the opacity of NC, optical methods only penetrate ~10 μm of a membrane thickness of 135 μm [15].

2.3.1. Initial Approach

This approach was initially conceptualized and tested using screen printed electrodes on either side of the test region of each sample. The test platform was designed, like the sample matrix shown above in Figure 15, to hold multiple samples and enable measurement with color intensity, with the added capability of electrical impedance measurement through the screen printed electrodes. Figure 25 shows a diagram of the layers of the initial design of the conductimetric test platform.

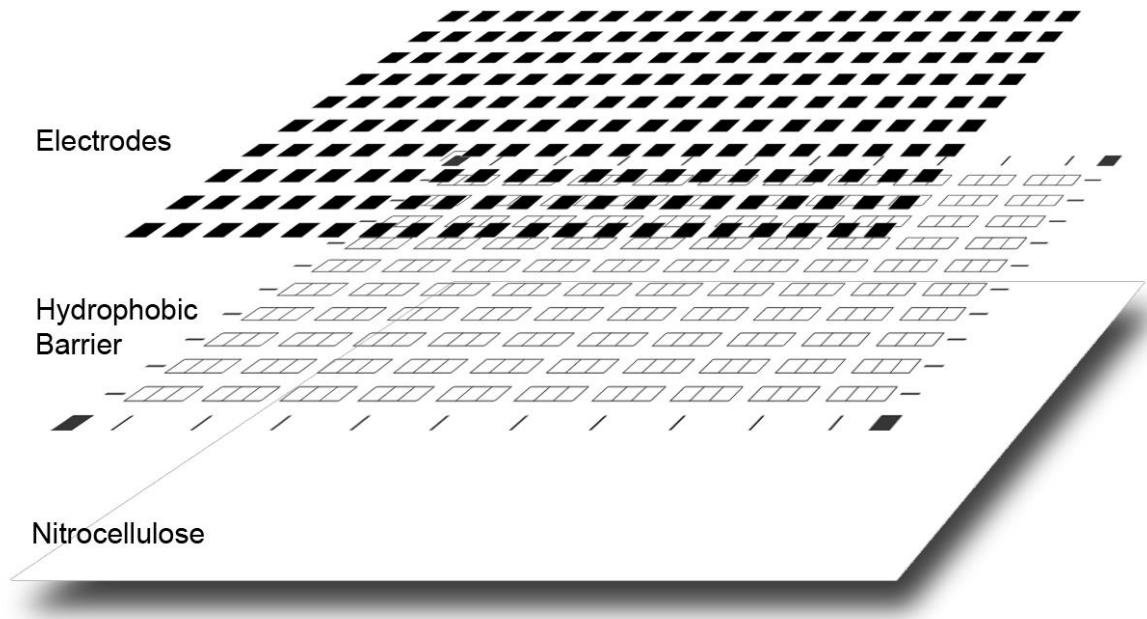


Figure 25. Exploded diagram showing the layers of the initial conductimetric test platform, which was designed to enable both optical and impedance measurements of samples.

The electrode pattern was designed, based on the test platform design, to provide a means to individually integrate each sample into an electric circuit to measure its impedance. In this design, one electrode is positioned on either side of each sample region. Two conductive inks were tested as electrode materials: PELCO Conductive Graphite in an isopropanol base (2400 Ω /sq/mil), and CAIG Laboratories, Inc., CircuitWriter Conductive Ink (0.017 Ω /sq/mil) [43] [44].

The electrodes were printed onto the paper after the membrane preparation process using screen printing techniques, including the photoemulsion image transfer method. A 110 mesh count monofilament polyester screen was coated with a thin layer of photoemulsion and set, horizontally, to dry in a dark room with a small desktop fan

nearby to circulate air. Three copies of the electrode design were printed in black ink on transparencies, then carefully aligned and layered to ensure opacity. After drying for 24 hours, the screen was exposed. To accomplish this, the screen was laid on top of black fabric, then the positive electrode design was laid on top of the screen and covered with a 2 mm thick sheet of glass (to ensure complete and uniform contact between the positive design and the screen). The surface of the screen was positioned approximately 6 inches away from two parallel 40 watt fluorescent tube lamps and exposed for 8 minutes, curing the exposed photoemulsion. Finally, the screen was washed out using a medium pressure stream of water to remove the unexposed emulsion, revealing the electrode design. A minor moiré pattern was observed in the electrode negative on the screen due to the mesh count of the screen and the detail and alignment of the electrode design (see Figure 26). Although the effect of this was not significant, it could be resolved, at least to some degree, by using a screen with a higher mesh count.



Figure 26. Close-up photograph of electrode negative used for screen printing.

Electrodes were printed using the prepared screen by sandwiching the test platform between a rigid working surface and the screen, then applying conductive ink to the screen and squeegeeing it across its surface to extrude it through the mesh and into the NC. Careful registration of the electrode design on the screen and the printed test platform design was necessary. Figure 27 shows printed graphite and silver electrodes.

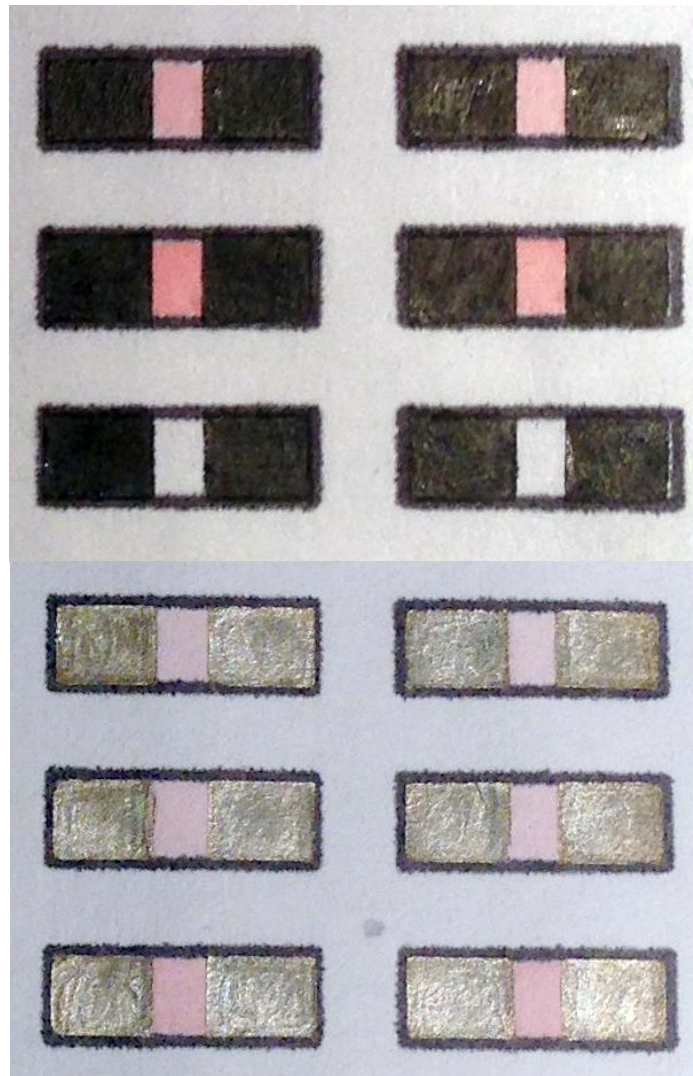


Figure 27. Screen printed electrodes. Top, conductive graphite ink; bottom, conductive silver ink. Images were adjusted to improve visibility.

Preliminary testing revealed technical flaws with this approach. It was not possible, with the methods that were used, to maintain consistent application thicknesses of conductive ink, which resulted in greatly varying electrode resistances. Probe placement on the electrodes also had an effect on electrode resistance. The silver electrodes were found to be superior to the graphite electrodes, however, there was still contact resistance at the electrode-sample interface.

2.3.2. Refined Conductance Based Detection Approach

Like with optical methods, the membrane sample volumes used for evaluation of LODs with the conductimetric approach were greater than the dispensed sample volumes that were tested. This was done in order to prevent variations in dispensed sample volume from resulting in concentration differences.

The 50 nm diameter GNP suspension that was purchased from Sigma-Aldrich was initially at a concentration of 3.51×10^{10} particles/mL, and suspended in 0.1 mM PBS. Concentrated PBS (10×) was purchased from Fisher Scientific (Catalog No.: BP3994) and diluted to 0.1 mM with DI water. This diluted PBS was then used to prepare a series of dilutions of GNPs and as a blank (see Table 4).

Table 4. Samples, Concentrations and Buffer Concentration Used for Conductimetric Testing (Note that PBS concentration is listed as combined salt and phosphate concentration – suspended GNP concentration is zero)

Sample	Concentration (M)	Concentration (M/k)
1	$(5.83 \pm 0.58) \times 10^{-11}$	$(4.08 \pm 0.41) \times 10^{-13}$
2	$(2.91 \pm 0.29) \times 10^{-11}$	$(2.04 \pm 0.20) \times 10^{-13}$
3	$(1.46 \pm 0.15) \times 10^{-11}$	$(1.02 \pm 0.11) \times 10^{-13}$
4	$(7.29 \pm 0.73) \times 10^{-12}$	$(5.10 \pm 0.51) \times 10^{-14}$
5	$(3.64 \pm 0.36) \times 10^{-12}$	$(2.55 \pm 0.25) \times 10^{-14}$
6	$(1.82 \pm 0.18) \times 10^{-12}$	$(1.27 \pm 0.13) \times 10^{-14}$
7	$(9.11 \pm 0.91) \times 10^{-13}$	$(6.37 \pm 0.64) \times 10^{-15}$
8	$(4.55 \pm 0.45) \times 10^{-13}$	$(3.19 \pm 0.31) \times 10^{-15}$
9	$(2.28 \pm 0.23) \times 10^{-13}$	$(1.59 \pm 0.16) \times 10^{-15}$
10	$(1.14 \pm 0.11) \times 10^{-13}$	$(7.96 \pm 0.77) \times 10^{-16}$
PBS	$(1.00 \pm 0.09) \times 10^{-4}$	$(1.00 \pm 0.09) \times 10^{-4}$

Rather than screen-printed electrodes directly on the membrane, reusable, but inexpensive electrodes were incorporated into a clamping device and used for testing. Eliminating screen-printed electrodes reduces the complexity and cost of manufacturing membranes, and leads to a more robust and consistent system.

Using silver-based electrodes with large contact areas can help counter the effect of contact resistance. Contact resistance can be effectively mitigated by using a four-terminal sensing approach. Four nickel-plated steel electrodes were used. They were arranged linearly with a distance of 1.8 mm between each adjacent pair. The exterior electrodes were used to inject current and as a reference and the interior pair were each used to measure potential. Figures 28 and 29 show the four-terminal electrode clamp that

was built, which provides consistent electrode spacing and pressure at contact points during measurements.

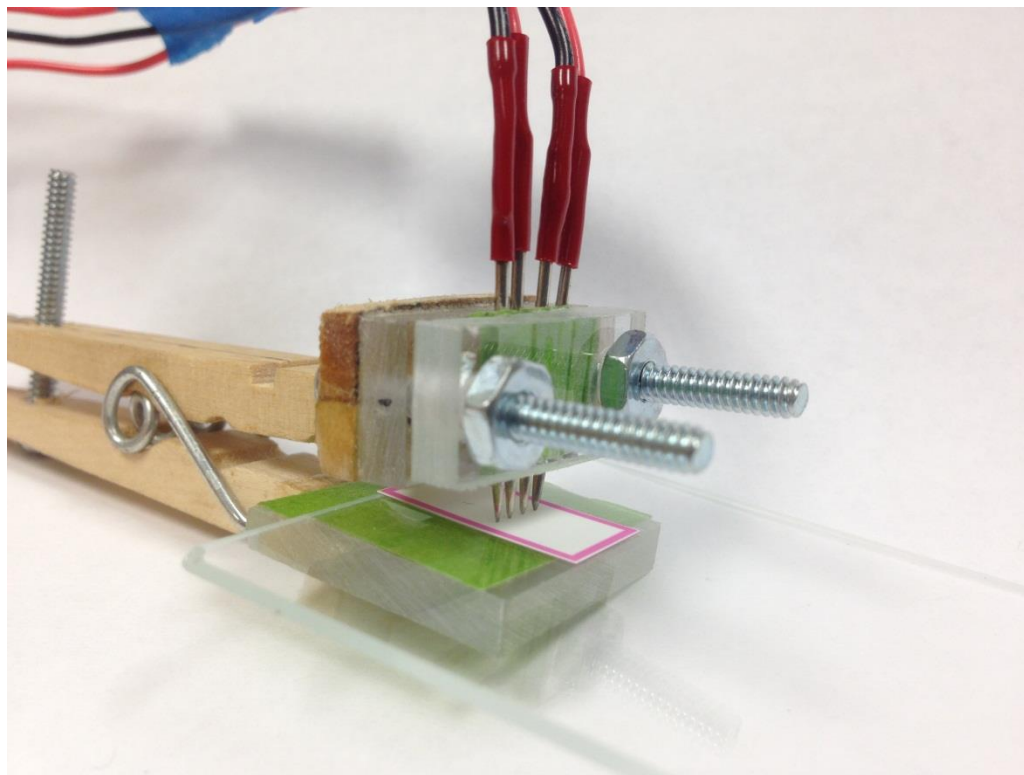


Figure 28. Four-terminal electrode clamp used for conductimetric measurements (perspective view).

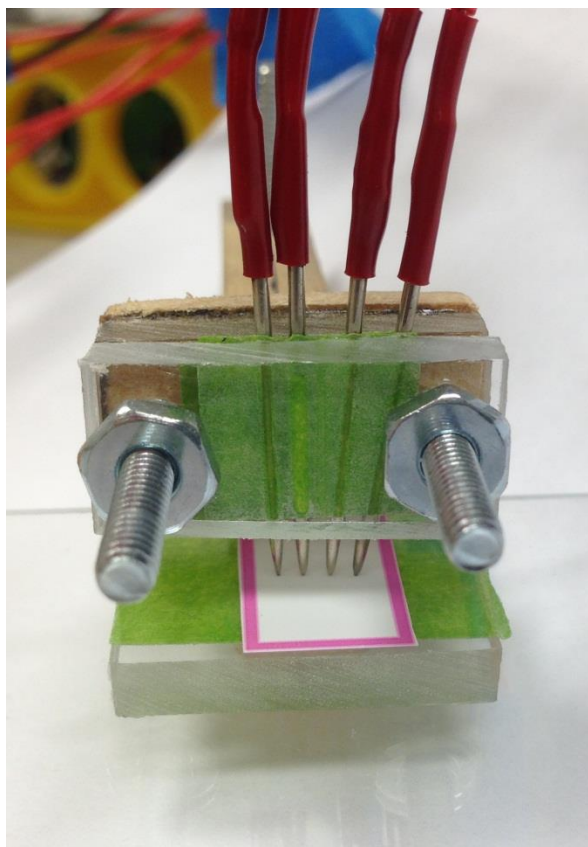


Figure 29. Four-terminal electrode clamp used for conductimetric measurements (frontal view).

2.3.2.1. Electrode Cleaning:

The reusable electrodes were cleaned with cotton-tipped applicators saturated with DI water. Each electrode was soaked and scrubbed with the applicator for 5 seconds while rotating it to constantly expose clean cotton. The electrodes were cleaned before each data collection run and then set to dry for 5 minutes before use.

2.3.2.2. Contact Resistance:

Two terminal sensing revealed that contact resistance was much larger than the resistances resulting from the samples. This can lead to a situation where the signal of interest is effectively indistinguishable from noise. Four terminal sensing provides a way to compensate for contact resistance and measure the signal of interest in spite of it.

2.3.2.3. Temperature Control System:

Since temperature can have a significant influence on how effectively samples are able to conduct, a simple temperature control system was set up to make it possible to take all measurements at a constant temperature. Also incorporated into this system was a physical barrier which helped to mitigate the effects of air currents.

The sensor was placed on a platform that was constructed with a glass slide and masking tape inside of a 1000 mL beaker, which was laid on its side. A cover was cut out of heavy construction paper and used to close the open end of the beaker. A temperature probe was taped into place inside the beaker, so that it was near where the sensor was placed and not touching any surfaces (see Figure 30).

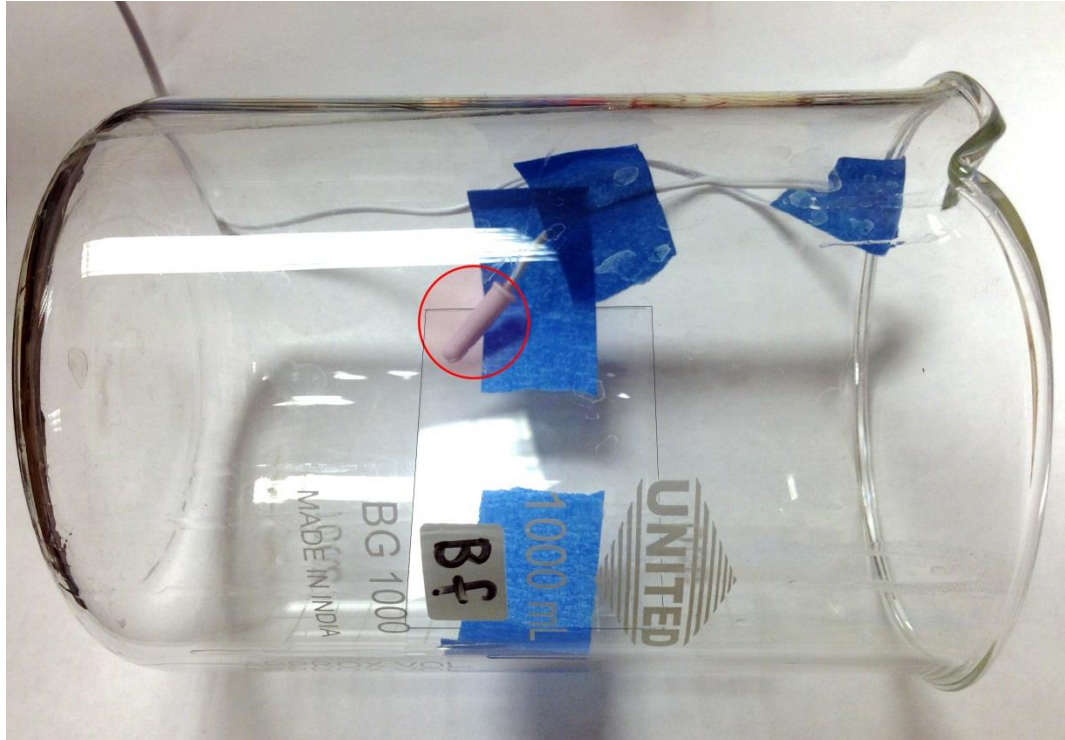


Figure 30. Beaker with platform and temperature probe taped in place. Temperature probe is marked with a red circle.

To achieve temperature control, the beaker was placed near a vent on the back of a desktop computer that exhausted air that was $\sim 38^{\circ}\text{C}$ under normal conditions. The laboratory where experiments took place was temperature controlled to $\sim 22^{\circ}\text{C}$. The beaker was positioned so that it received some heated air from the exhaust vent and was moved, slightly, further in or out of the stream of exhaust in order to maintain a target temperature of 25°C , within about 1%. The readout of the digital thermometer that was used was set to Fahrenheit in order to increase resolution, and then converted to Celsius after recording. The temperatures at the start and finish of each measurement run were recorded and then averaged to give a temperature for each measurement. Figure 31 shows the temperature control system setup.

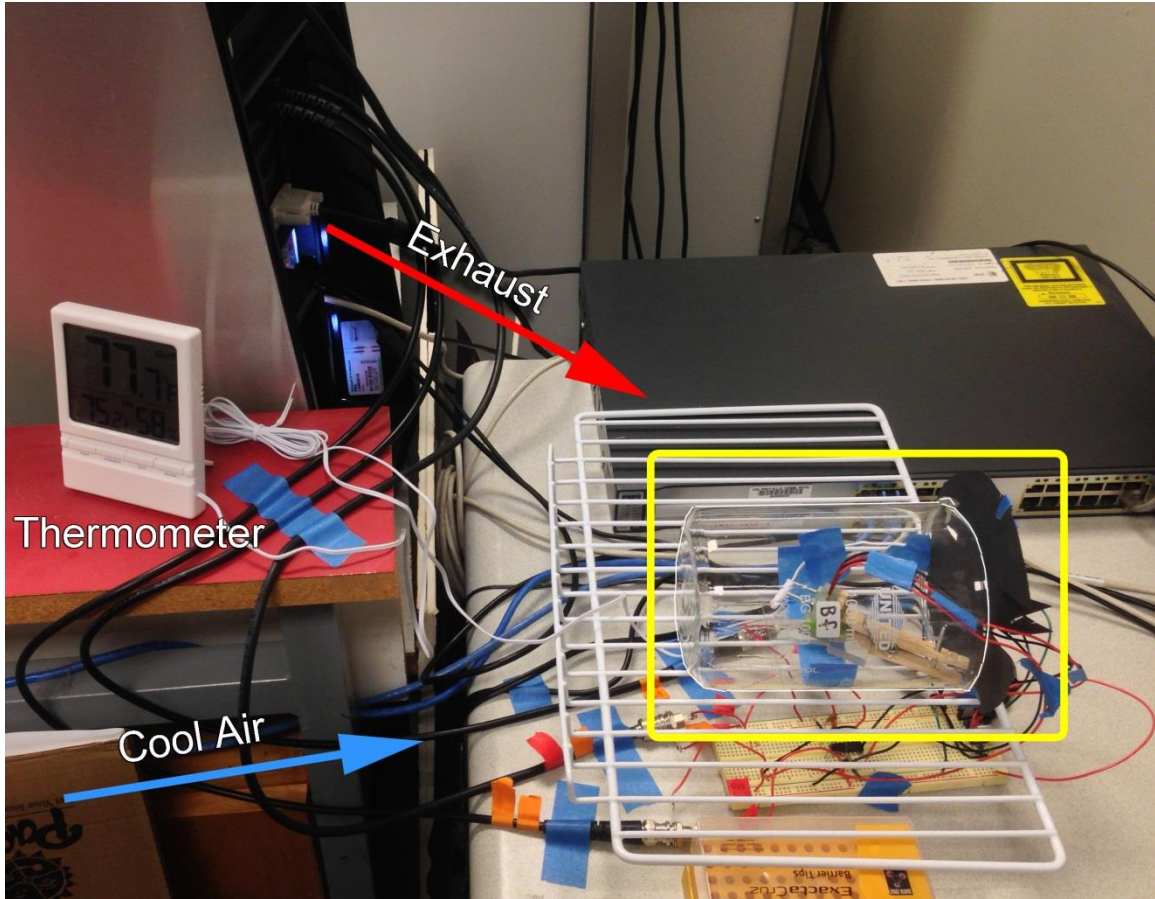


Figure 31. Temperature control system setup. The beaker is marked with a yellow rectangle. The thermometer is labeled, and approximate warm exhaust and cool air directions are indicated.

2.3.2.4. Electronics and Measurement Strategies:

Instrumentation amplifiers (IAs) were employed to achieve high input impedance and differential amplification. High input impedance was necessary to eliminate loading from the relatively low impedance of the NI digitizer inputs ($1\text{ M}\Omega$) compared to the samples (up to $\sim 500\text{ k}\Omega$). The IAs that were used (Texas Instruments INA2126, purchased from Digi-Key Corp., part number INA2126PA-ND) essentially add a unity

gain buffer with an impedance of 1 G Ω to each input. Since this is much larger than the sample impedance, loading is negligible. The differential amplifier function of the IA was useful, primarily because it reduces the number of inputs from four to two by taking the difference of each pair. This was necessary because the digitizer that was used had only 2 inputs available. Initially, two IAs were assembled with individual op-amps on a breadboard (see Figure 32), but for actual data collection, a circuit was assembled which incorporated the INA2126, a dual IA integrated circuit (see Figure 33). The upgraded circuit greatly reduces complexity.

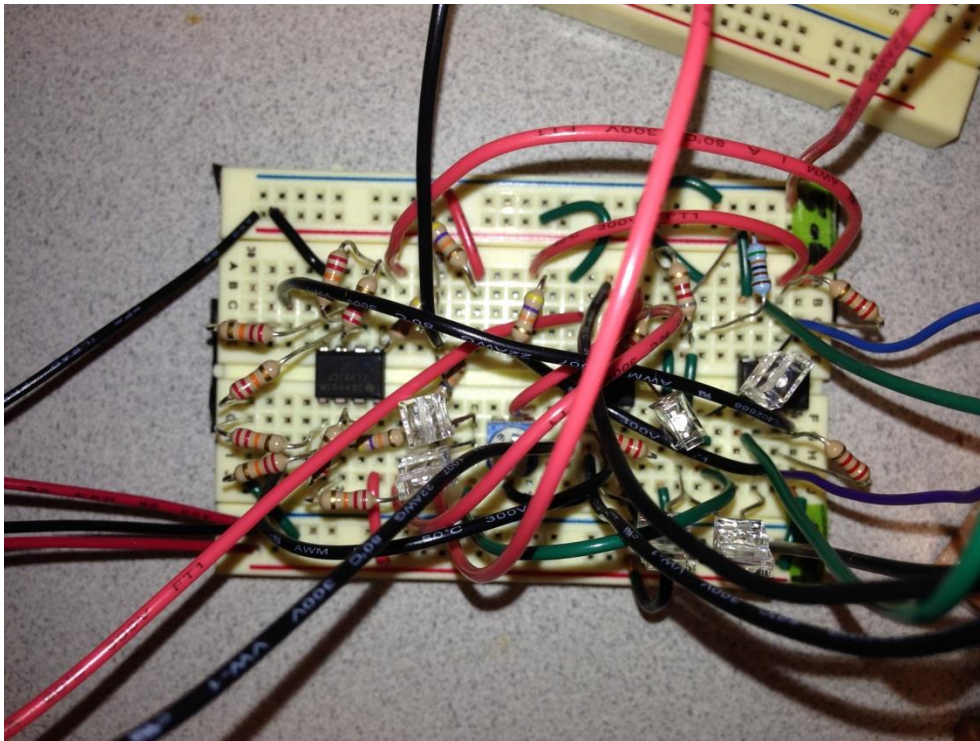


Figure 32. Original dual instrumentation amplifiers which were used for testing purposes. This design uses three op-amps per instrumentation amplifier. Potentiometers are present to provide adjustable gain for each channel and safety diodes are visible.

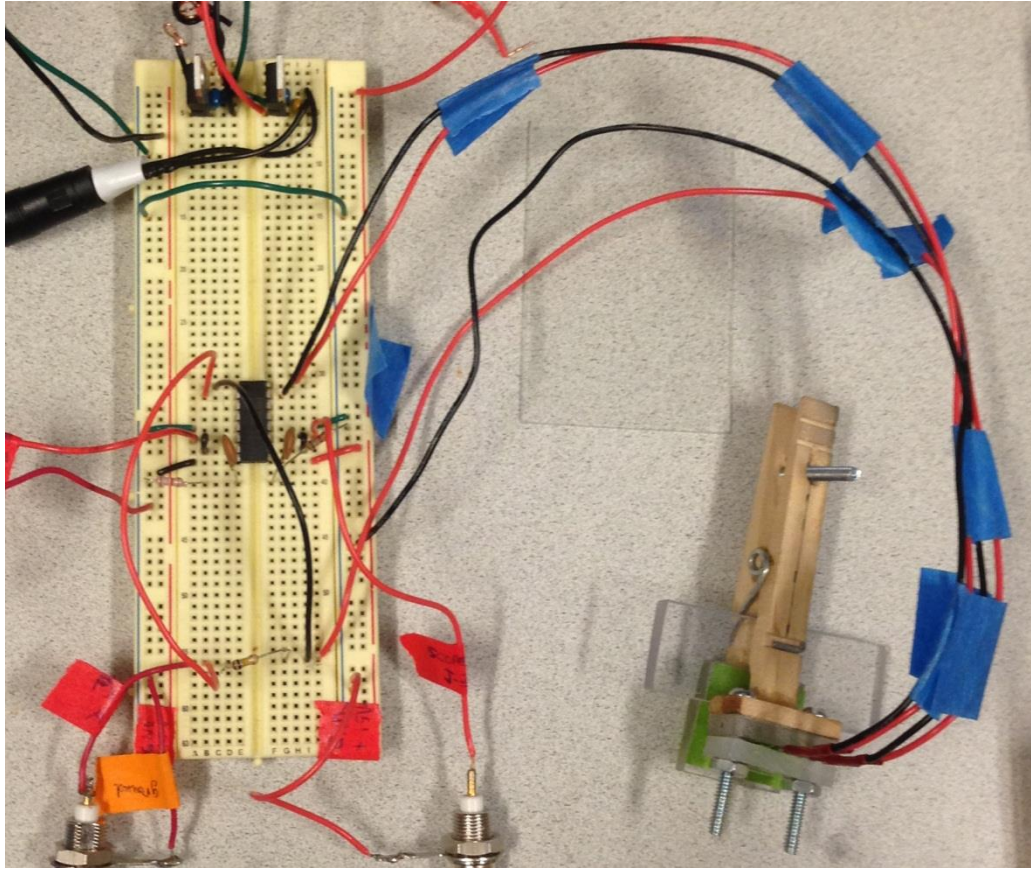


Figure 33. Upgraded measurement circuit incorporating a dual instrumentation amplifier integrated circuit.

The INA2126 uses two op-amps, connected by a network of resistors, to form an IA. A schematic for the circuit that is formed is shown in Figure 34.

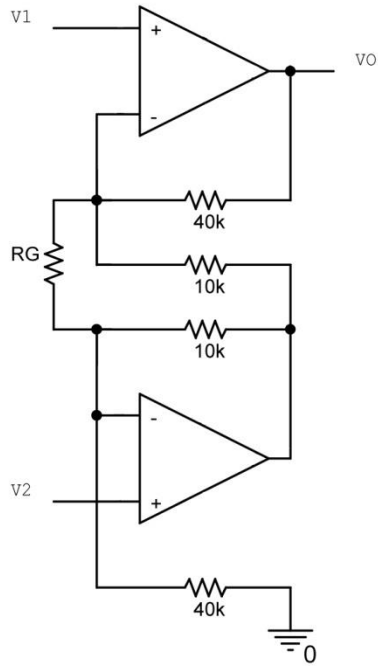


Figure 34. Schematic for two-op-amp instrumentation amplifier circuit used in INA2126.

The equation for the output at VO , in terms of the inputs, $V1$ and $V2$, and the external gain resistor, RG , is given in eq. 11 as:

$$VO = (V1 - V2) \left(\frac{80k\Omega}{RG} + 5 \right) \quad (11)$$

No resistor was placed for RG , so it was left as an open circuit, resulting in a differential gain of 5.

Figure 35 shows a simplified schematic of the circuit used for measurement including the sensor, dual power supply, IA, function generator, and digitizer.

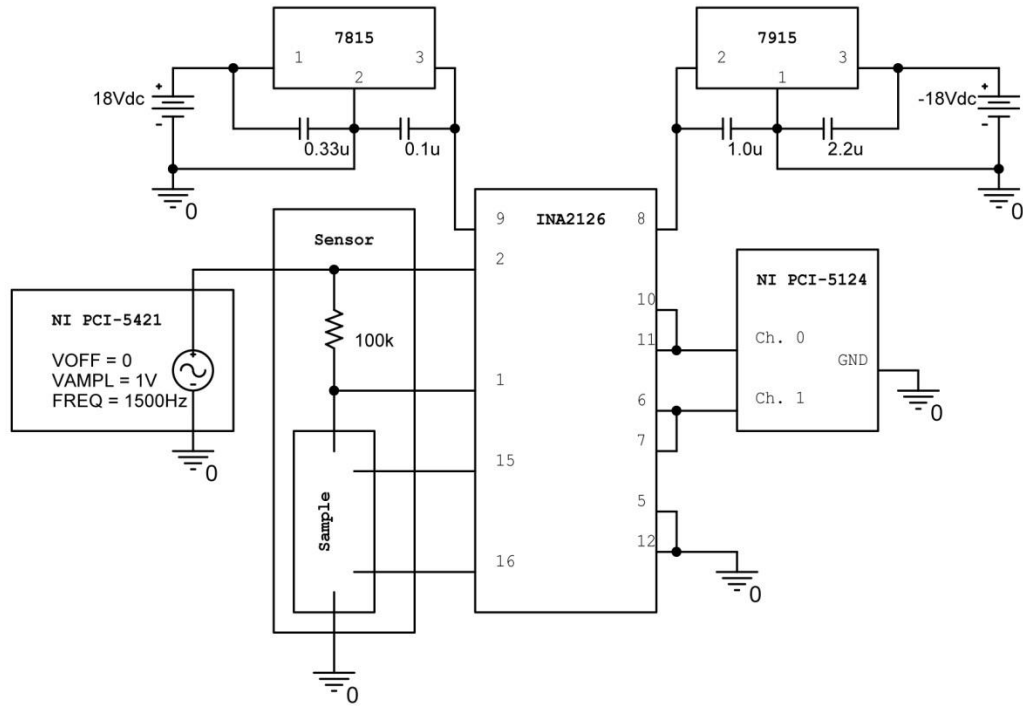


Figure 35. Simplified schematic of sensing circuitry used for conductimetric detection.

Impedance was determined by measuring the voltage across a resistor of known value in what is essentially a voltage divider circuit and calculating the current through it, then applying Ohm's law to find the unknown impedance in the sample region using measured potentials. The value of the resistor was chosen after initial testing showed that sample impedance magnitudes ranged from $\sim 100\text{ k}\Omega$ to $\sim 500\text{ k}\Omega$. The resistor value was selected to be on about the same order as this range in an attempt to maximize the resolution on both digitizer channels. Equations 12, 13, and 14 show the calculated impedance magnitude value, Z_{sample} , in terms of the fixed-value resistor, R_{100k} (which was measured with a multimeter to be $98.6\text{ k}\Omega$), voltages at pins 2, 1, 15, and 16 on the INA2126, and at channels 0 and 1 on the digitizer.

$$V_{CH\ 0} = 5(V_{pin15} - V_{pin16}) \quad (12)$$

$$V_{CH\ 1} = 5(V_{pin2} - V_{pin1}) \quad (13)$$

$$Z_{sample} = \left(\frac{V_{CH\ 0}}{V_{CH\ 1}}\right) R_{100k} \quad (14)$$

Conduction occurs through mobile charge carriers, which GNPs provide. A linear relationship between conductance and concentration was expected, as each GNP contributes a fixed and constant amount to the ability of a sample to conduct. Other factors that influence conductivity are buffer composition and concentration (which can be predicted by Kohlrausch's law), membrane conductivity, and temperature.

2.3.2.5. LabVIEW:

A program was developed in LabVIEW and run on a computer with National Instruments 16 bit arbitrary waveform generator (NI PCI-5421) and 12 bit digitizer (NI PCI-5124) cards. The function generator was used to drive the sensor circuit with a 1.5 kHz 1 V sine wave source, and the two-channel digitizer was used to measure the potential difference across the known-value resistor and between the interior sensor probes through IAs. Current through the circuit was computed, and impedance magnitude and phase data for the unknown sample were output. (LabVIEW block diagram is in

APPENDIX C.) The front panel for the LabVIEW program is shown in Figure 36 and a close-up of settings is shown in Figure 37.

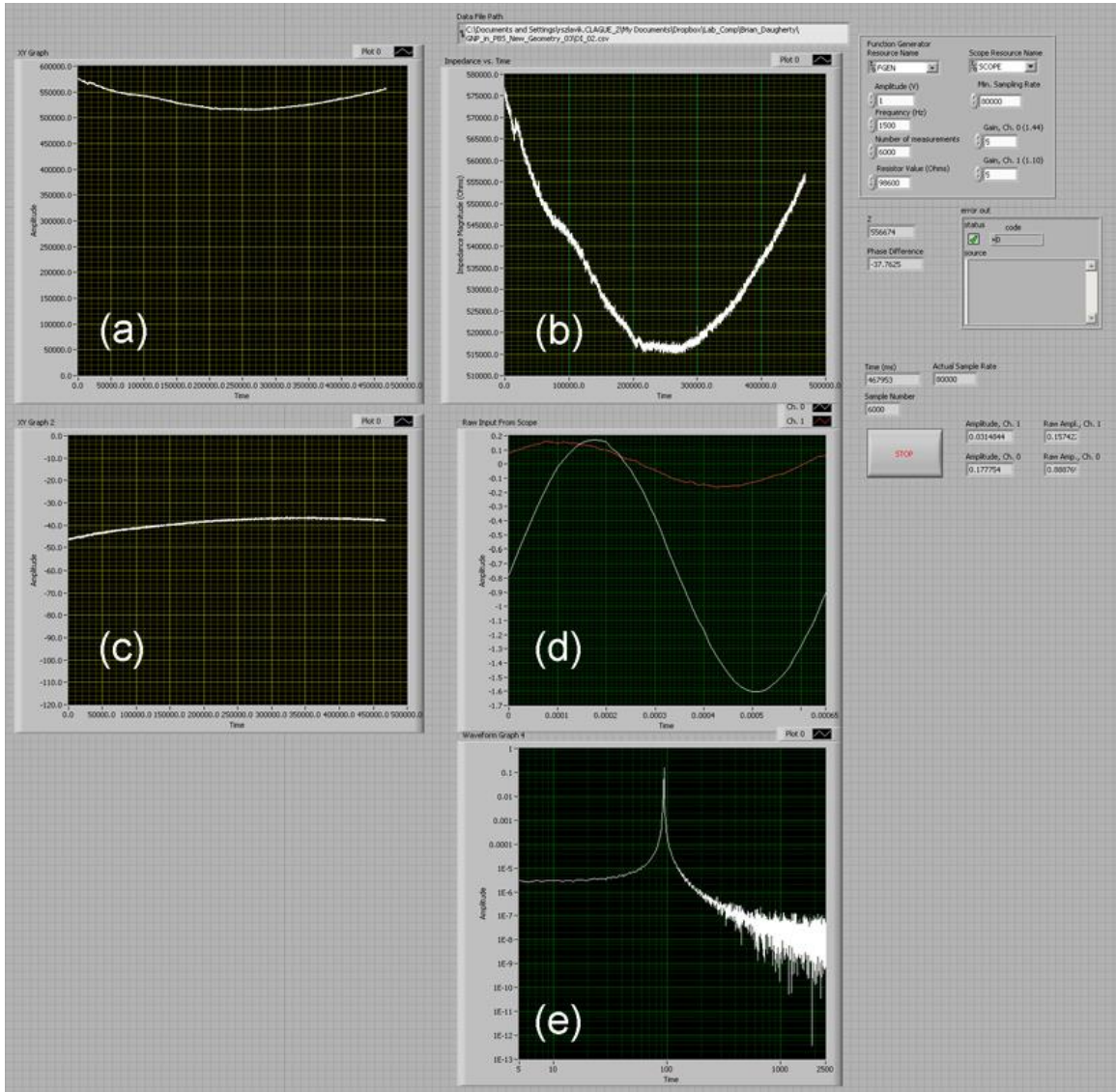


Figure 36. Front panel of LabVIEW conductimetric data acquisition software. (a) Full-scale impedance magnitude (Ω) vs. time (ms); (b) scaled impedance magnitude (Ω) vs. time (ms); (c) scaled phase angle (degrees) vs. time (ms); (d) scaled raw input from oscilloscope, potential (V) vs. time (s), Ch. 0 is white (sensor), Ch. 1 is red (resistor); (e) scaled power spectrum of Ch. 0, power (V_{rms}^2) vs. frequency (Hz).

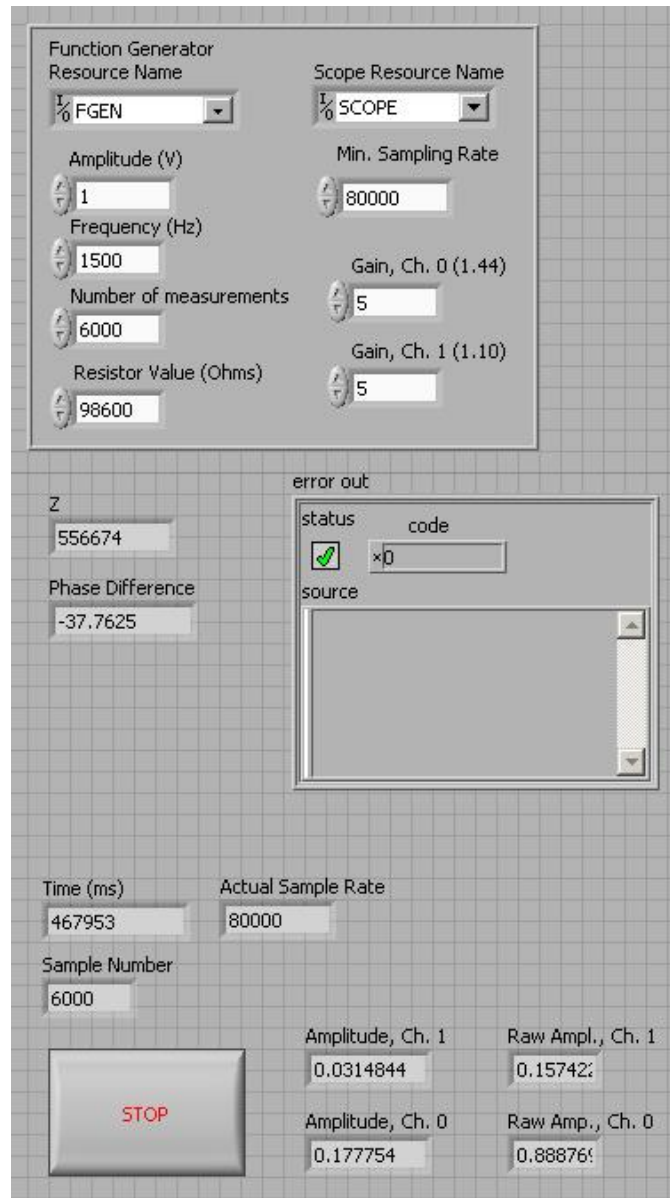


Figure 37. Settings and readouts on front panel. Note that a maximum number of measurements can be set, but the “STOP” button can initiate an interrupt to cease acquisition and save data.

Since the sensor is driven with a 1500 Hz AC source, it is possible to digitally process the incoming signal to remove noise above and below this frequency. For each channel, the tone with the highest amplitude is detected and used for measurement. The

root mean square potential across the fixed-value resistor provides the information to calculate current through the sensor circuit and the root mean square potential across the interior sensor probes can be divided by this current to calculate the impedance magnitude. Phase difference is determined using LabVIEW's built-in phase detection and subtracting the Ch. 1 phase angle from the Ch. 0 phase angle. Additionally, the 1500 Hz source prevents electrolysis, which could be an issue with a DC source (especially because of the sample buffer).

Each sample measurement was run for approximately 5 minutes with a data collection rate of ~13 values/second, and a predetermined maximum set to 6000 data points. The 1500 Hz waveform was sampled at 80 kHz, which is much greater than its associated Nyquist frequency. At the end of the data collection run for each sample, the impedance information (magnitude and phase) and the time since the start of the run for each data point were automatically saved to a .CSV file (with the file path and name determined by the user).

Another program was written in MATLAB to process the data collected in each sample measurement run and extract a single impedance magnitude value. Each sample, and the blank, were run 10 times, and impedance magnitude values were determined for each, then inverted to give conductance (and averages and standard deviations were calculated). These values were then plotted against their corresponding concentrations and used to determine the conductimetric LOD of GNPs in NC.

The collected data for each run was fit with a 2nd order polynomial and the minimum was determined. After importing a .CSV file to the MATLAB program, the

limits on the horizontal axis were defined through a graphical user interface and the data were cropped to the window of interest, if necessary (code is presented in APPENDIX D). The calculated minimum impedance magnitude value and R^2 for the fit are output to the MATLAB Command Window. Figure 38 shows an example of a plot and polynomial fit generated by the program (minimum impedance magnitude = 461970 Ω , $R^2 = 0.9968$).

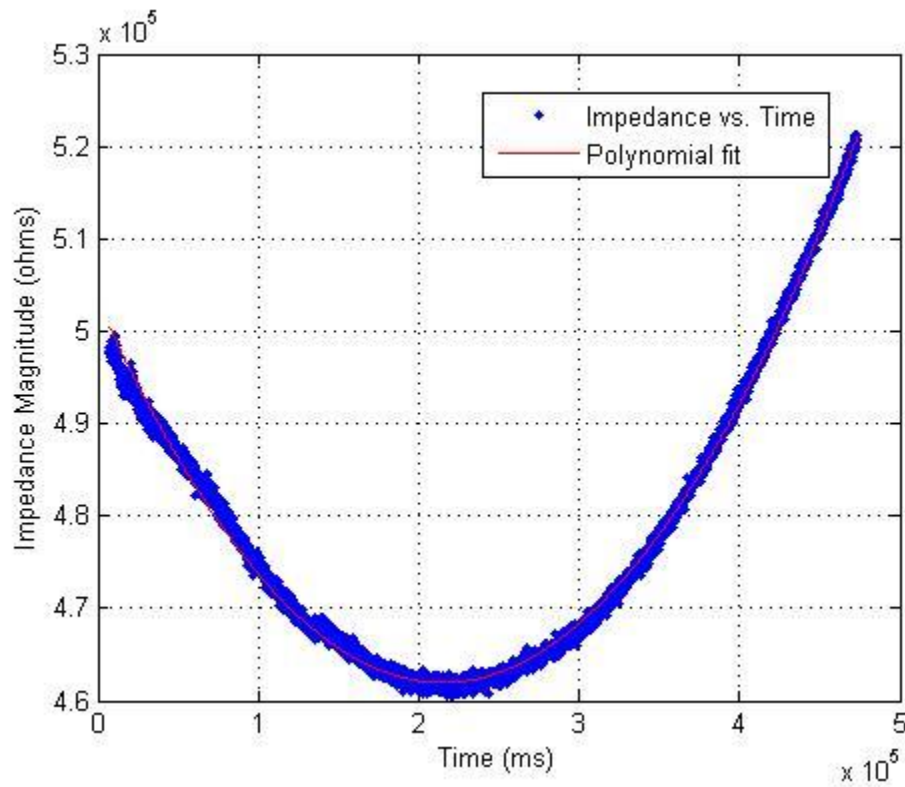


Figure 38. Example of plot and second order polynomial fit generated from collected data.

2.3.2.6. Cell Constant:

In order to convert conductance values into conductivity, it was necessary to establish a cell constant for the system. This was accomplished by measuring the conductance of a substance which had a known conductivity. DI water was used, which had a reported resistivity of 18.4 M Ω -cm at a temperature of 25°C. Ten samples of DI were measured, following the same methods described for other samples above.

2.3.3. *Peripheral Device Design*

A peripheral device to directly measure electrical impedance, that works using the same principles as the LabVIEW impedance meter but is specially designed to interface with a smartphone, was designed. This device is designed to be generic, with the capability to work with MEDs that have stereo headphone outputs and microphone line inputs. It utilizes low-power electronics, and draws power from one of the MED's audio output lines. The second output line drives the sensor. The microphone input receives two waveforms as a combined analog signal that is digitized using the MED's built-in analog to digital converter and then decomposed in software using digital signal processing (i.e., Fourier analysis).

3. RESULTS

3.1. Visual

The methods described in the section above were used to determine the visual detection limit. A series of dilutions of red dye were prepared and each was tested in triplicate, on an absence/presence basis, with 7 individuals. The visual detection limit for erythrosine was determined to be $(9.59 \pm 0.97) \times 10^{-4}$ M (bold in Table 5), which has an equivalent GNP concentration of $(3.98 \pm 0.40) \times 10^{-11}$ M. This concentration ensures 95% positive responses.

Table 5. Visual Detection Limit

Sample	Erythrosine Concentration (M)	GNP Concentration (M/k)
0	0	0
1	$(1.66 \pm 0.17) \times 10^{-3}$	$(6.92 \pm 0.70) \times 10^{-11}$
2	$(9.59 \pm 0.97) \times 10^{-4}$	$(3.98 \pm 0.40) \times 10^{-11}$
3	$(5.51 \pm 0.55) \times 10^{-4}$	$(2.28 \pm 0.23) \times 10^{-11}$
4	$(3.17 \pm 0.32) \times 10^{-4}$	$(1.31 \pm 0.13) \times 10^{-11}$
5	$(1.82 \pm 0.18) \times 10^{-4}$	$(7.55 \pm 0.76) \times 10^{-12}$
6	$(1.05 \pm 0.10) \times 10^{-4}$	$(4.34 \pm 0.44) \times 10^{-12}$
7	$(6.01 \pm 0.60) \times 10^{-5}$	$(2.49 \pm 0.25) \times 10^{-12}$
8	$(3.45 \pm 0.35) \times 10^{-5}$	$(1.49 \pm 0.14) \times 10^{-12}$
9	$(1.99 \pm 0.20) \times 10^{-5}$	$(8.23 \pm 0.83) \times 10^{-13}$
10	$(1.14 \pm 0.11) \times 10^{-5}$	$(4.73 \pm 0.48) \times 10^{-13}$

3.2. Image Analysis

3.2.1. MED

The response of the green channel was used for all measurements because it was found to be most sensitive to light at the wavelengths of interest. The peak sensitivities for the green channel of each MED camera were spectrally close to the peak absorbance wavelengths of GNPs and erythrosine. Figures 39, 40, and 41 show the spectral responses of each of the color channels of the cameras that were used.

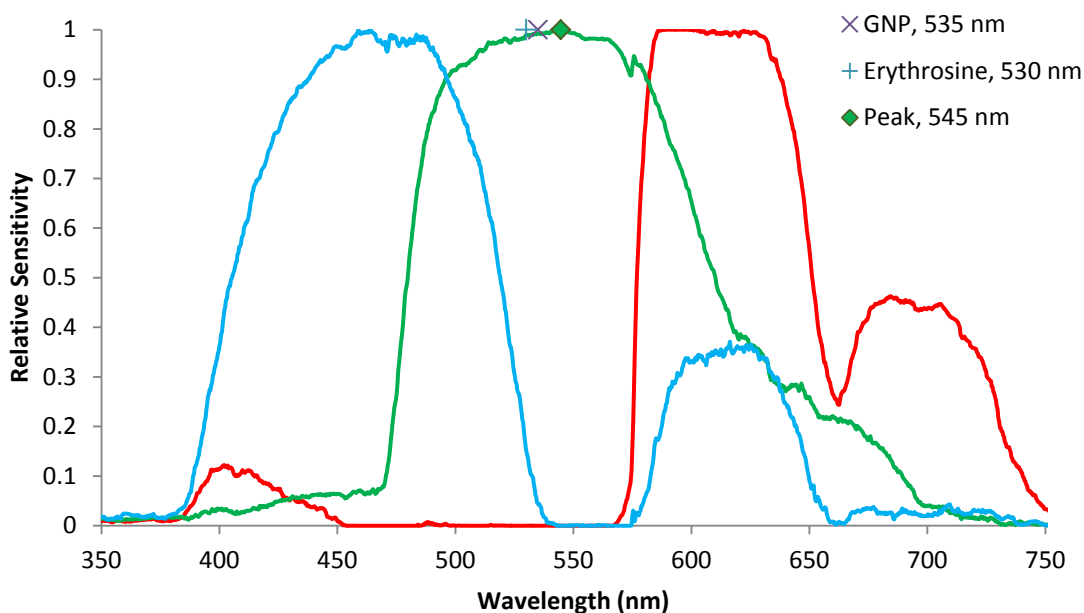


Figure 39. Spectral sensitivity of camera from Samsung Galaxy S smartphone. The peak sensitivity and the peak absorbance wavelengths for the GNPs and dye that were used are indicated.

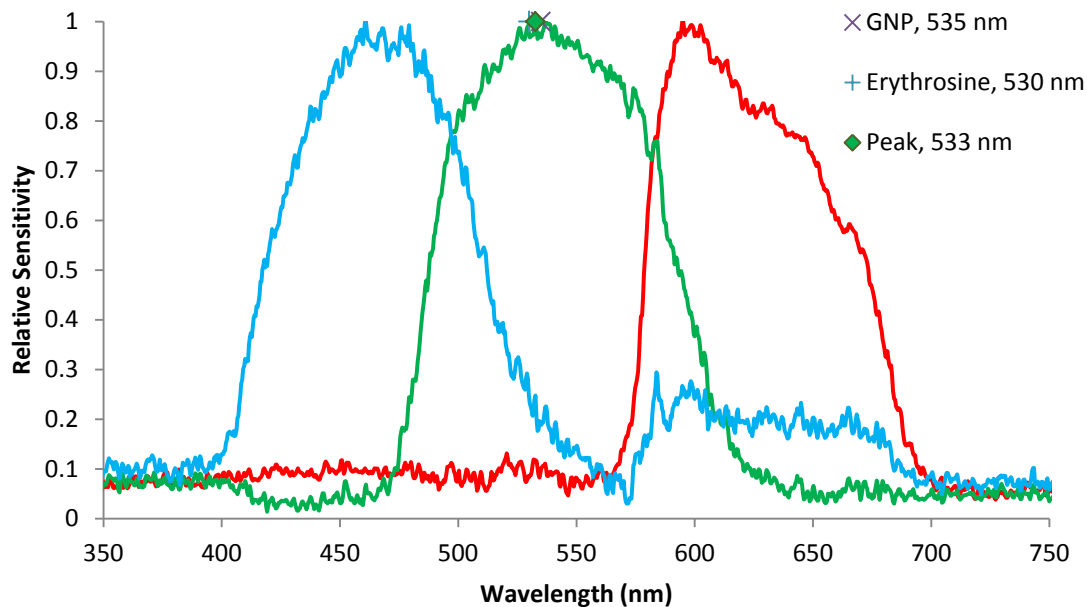


Figure 40. Spectral sensitivity of camera from iPad mini. The peak sensitivity of the green channel and the peak absorbance wavelengths for the GNPs and dye that were used are indicated.

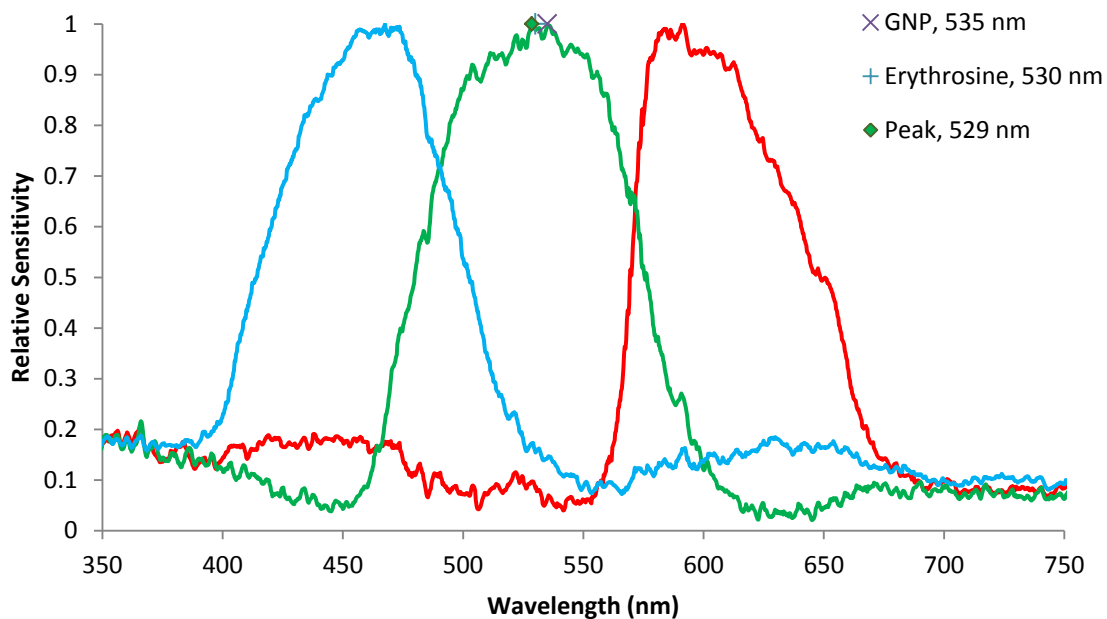


Figure 41. Spectral sensitivity of iPhone 5 camera. The peak green channel sensitivity and the peak absorbance wavelengths the GNPs and dye are indicated.

Data collected using a Samsung Galaxy S are presented in Figure 42. The GNP LOD was determined to be $(2.23 \pm 0.22) \times 10^{-11}$ M.

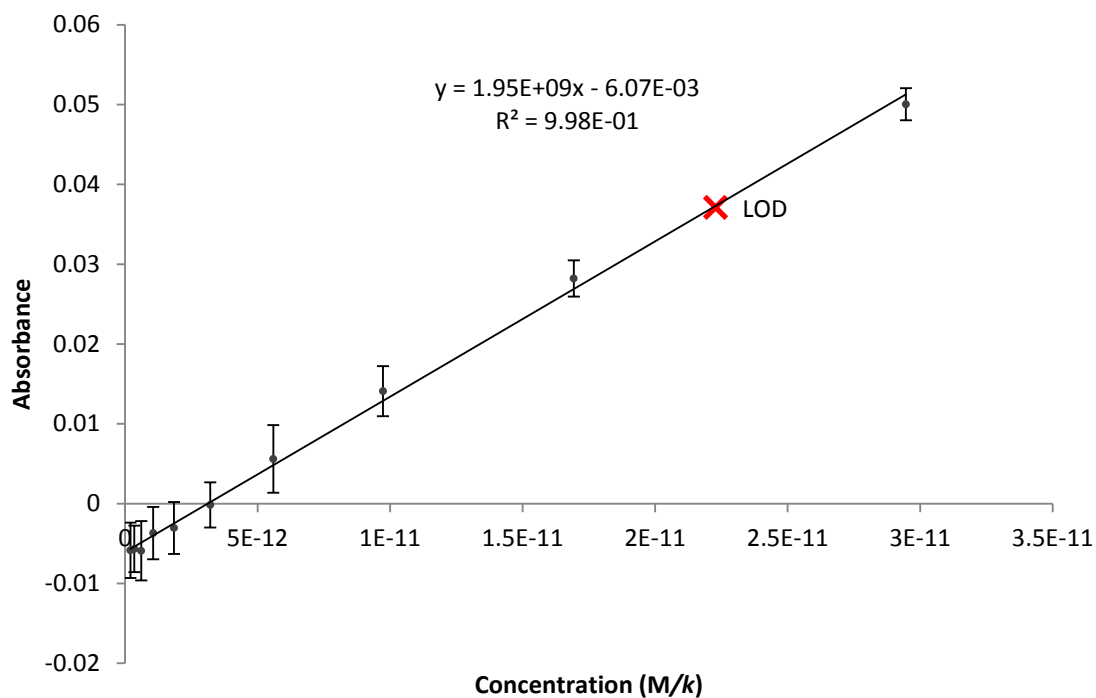


Figure 42. Linear regression of data collected from analysis of image captured with Galaxy S with erythrosine dye. The absorbance values of 8× concentrated GNP were measured, plotted, and used to calculate equivalent GNP concentrations for dye. Error bars represent the standard error of the mean (SEM) absorbance from ten replicates.

Data collected using an Apple iPad mini are presented in Figure 43. The GNP LOD for this device was found to be $(1.25 \pm 0.13) \times 10^{-11}$ M.

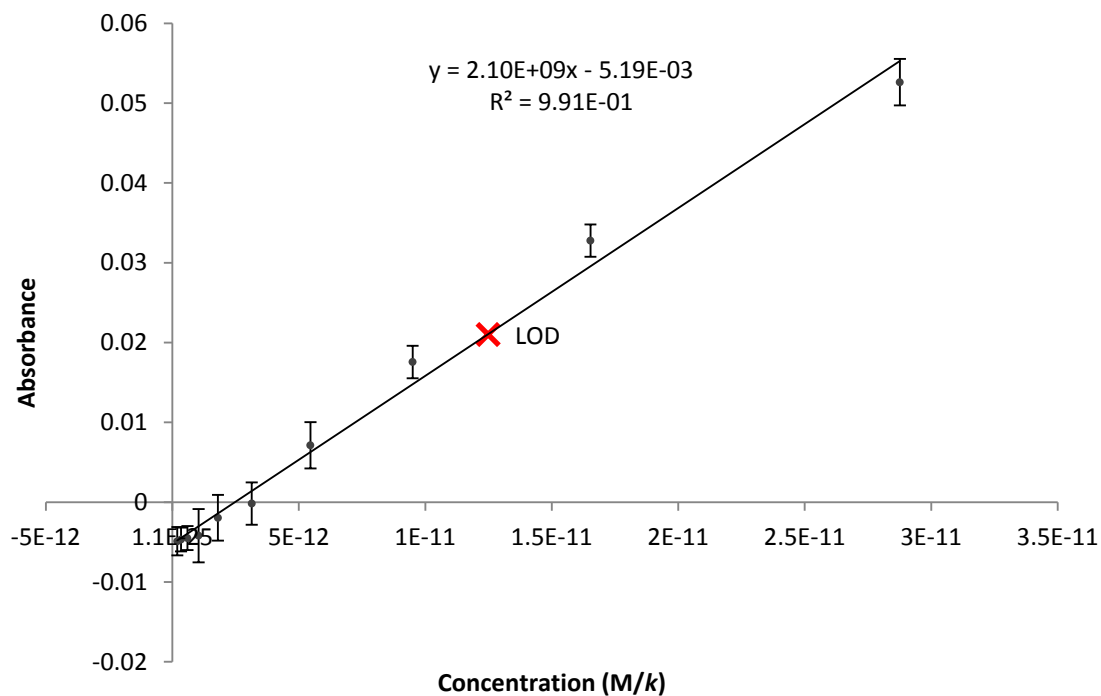


Figure 43. Linear regression of data collected from analysis of image captured with iPad mini with erythrosine dye. The absorbance values of 8× concentrated GNP were measured, plotted, and used to calculate equivalent GNP concentrations for dye. Error bars represent the SEM absorbance from ten replicates.

Data collected using an Apple iPhone 5 are presented in Figure 44. The GNP

LOD for this device was found to be $(1.41 \pm 0.14) \times 10^{-11}$ M.

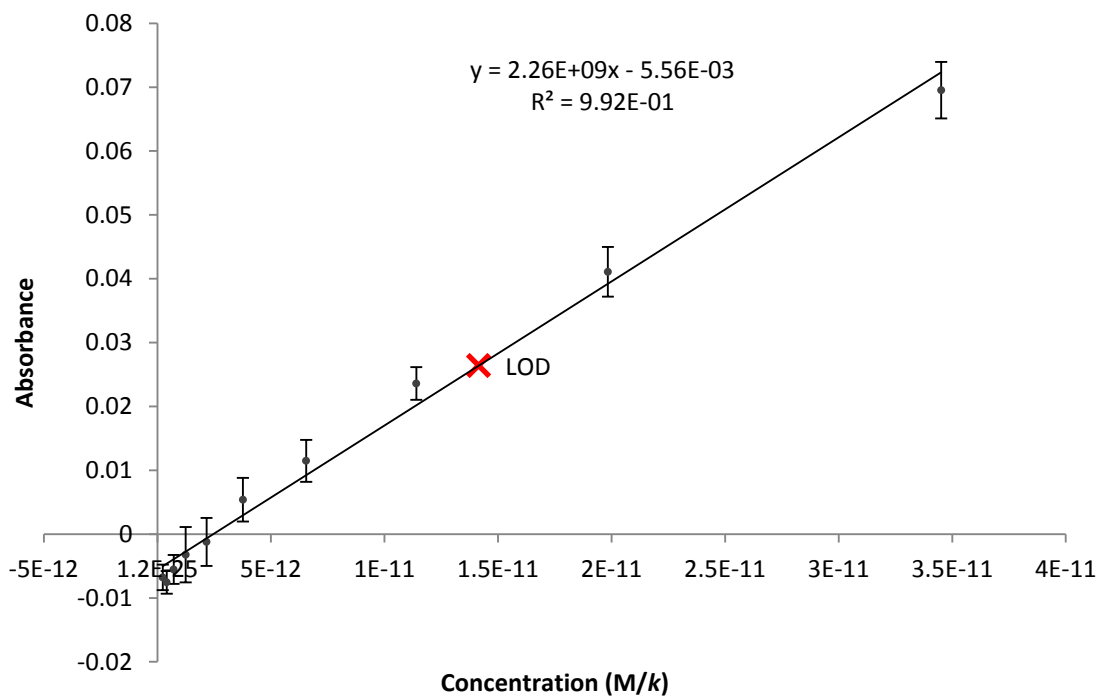


Figure 44. Linear regression of data collected from analysis of image captured with iPhone 5 with erythrosine dye. The absorbance values of 8× concentrated GNP were measured, plotted, and used to calculate equivalent GNP concentrations for dye. Error bars represent the SEM absorbance from ten replicates.

3.2.2. Microscope 5×

Figure 45 shows the result of analysis of images collected with the microscope, using a 5× objective. Ten instances of each sample were measured individually, including the blank and the gold colloid. Ten pieces of plain NC were also measured to provide a reference. The GNP LOD was determined to be $(1.16 \pm 0.12) \times 10^{-12}$ M.

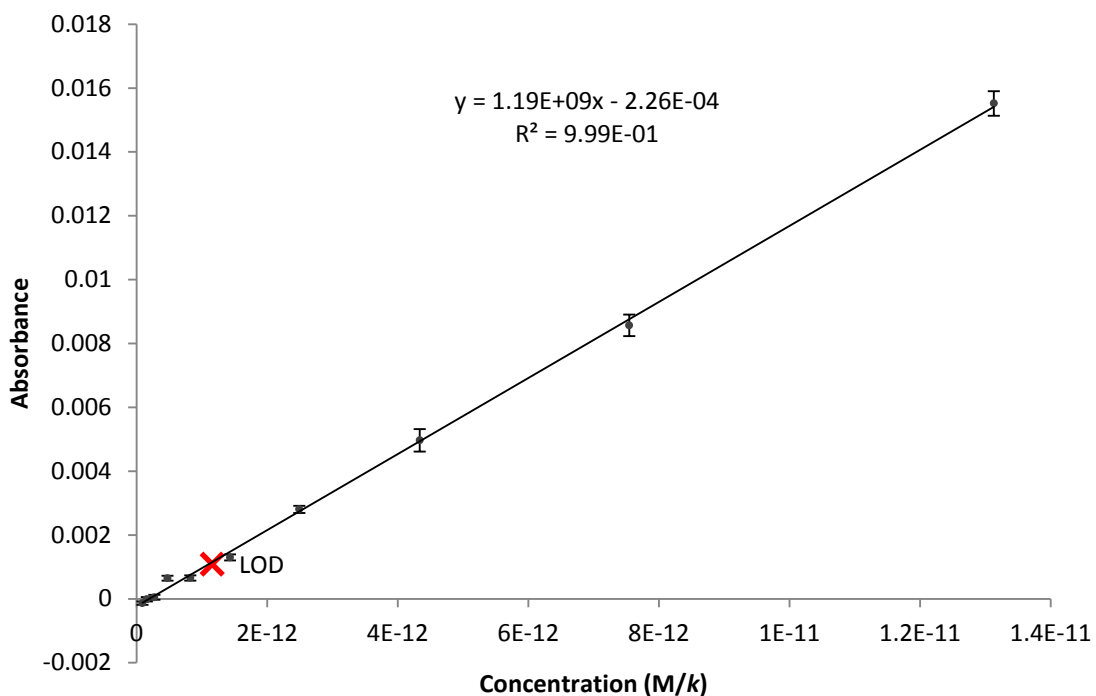


Figure 45. Result of analysis of images collected from the microscope using a 5× objective and using erythrosine. The absorbance values for 8× GNP were measured and plotted and then used to calculate equivalent concentrations of dye. Error bars represent the SEM absorbance from ten replicates.

3.2.3. Microscope 10×

Figure 46 shows the results of analysis of images collected with the microscope, using a 10× objective. The same measurement procedure was followed as with the 5× objective. The GNP LOD was found to be $(9.56 \pm 0.96) \times 10^{-13}$ M.

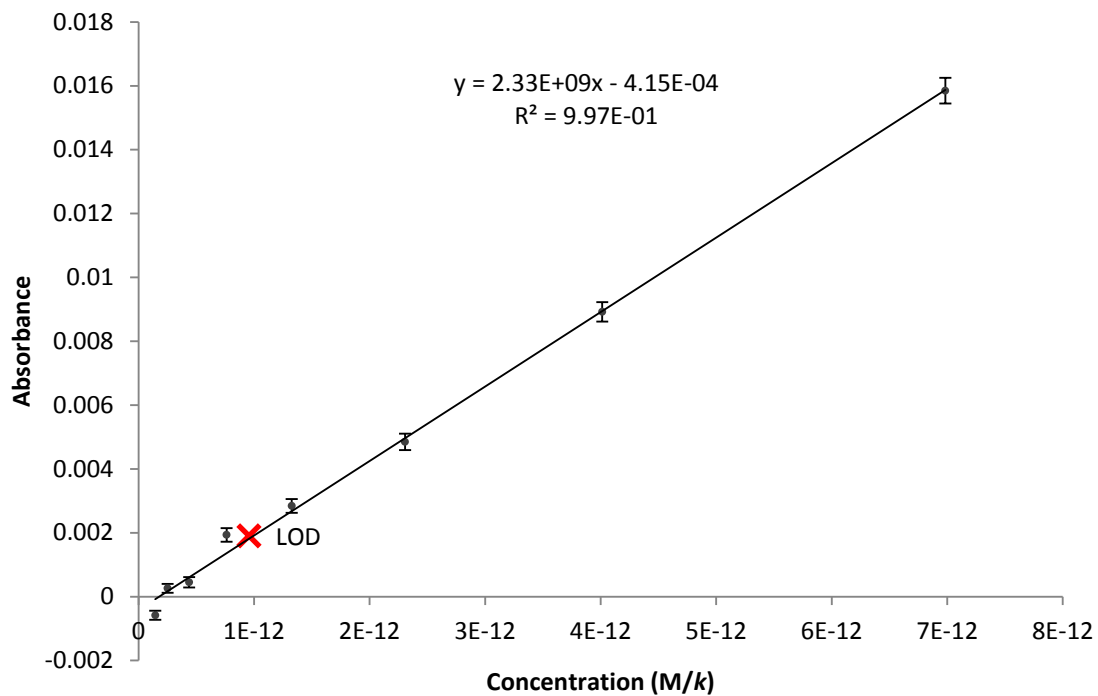


Figure 46. Result of analysis of images collected from the microscope using a 10× objective and using erythrosine. The absorbance values for 8× GNP were measured and plotted and then used to calculate equivalent concentrations of dye. Error bars represent the SEM absorbance from ten replicates.

3.3. Conductimetric Detection

A comparison was made between the two- and four-terminal measurement approaches to show the benefit of four terminals. The data shown in Figure 47 were collected for the same GNP sample.

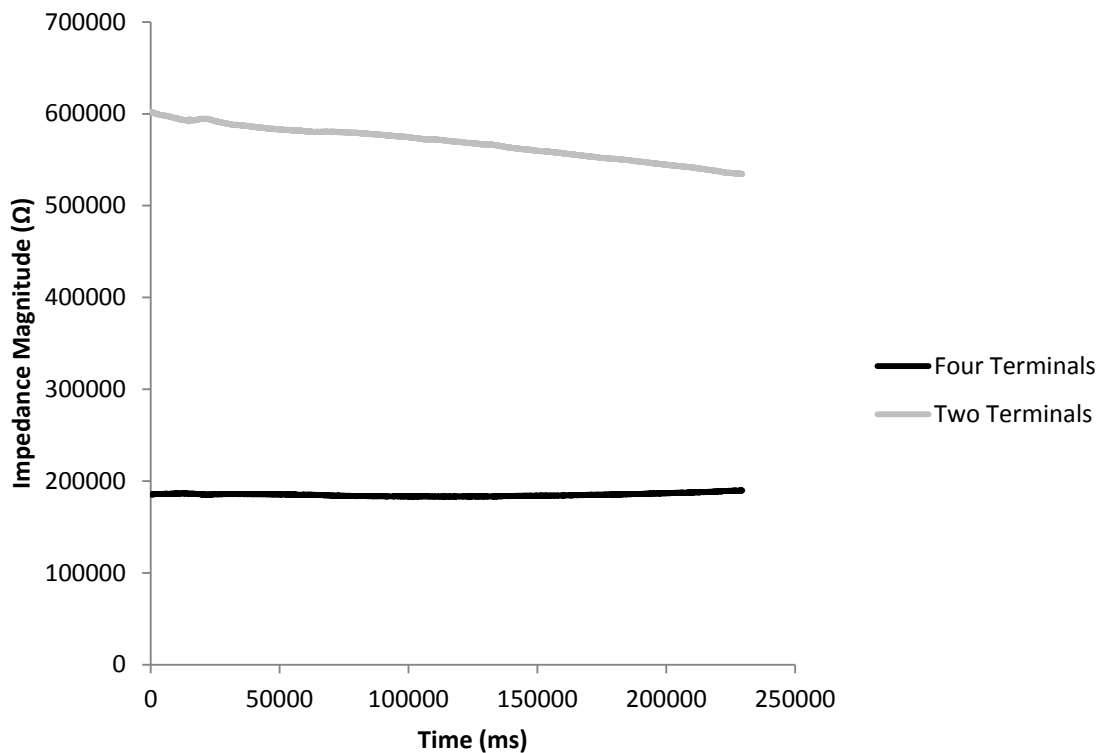


Figure 47. Comparison of two- and four- terminal sensing measurements.

Figure 48 shows data collected using the conductimetric approach. Ten samples of each concentration, including the blank, were measured. The temperature was maintained at $(25.1 \pm 0.25)^\circ\text{C}$. The LOD was found to be $(2.66 \pm 0.27) \times 10^{-14}$ M.

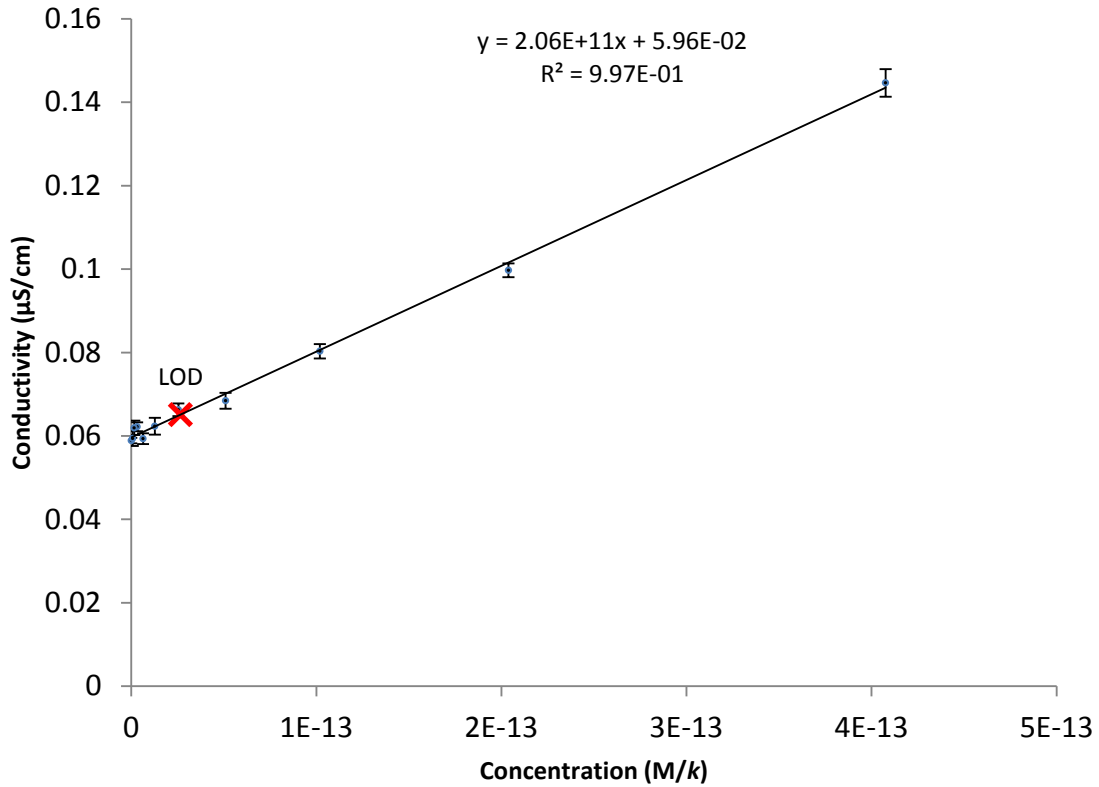


Figure 48. Data collected using the conductimetric approach, fitted using a linear regression. Error bars represent the SEM conductivity.

A cell constant for the measurement system was calculated by measuring 10 samples of DI water with an externally verified resistivity of 18.4 MΩ-cm at 25°C. The cell constant, which was measured with the same temperature constraints, was determined to be (38.4 ± 0.6) cm.

3.4. Peripheral Device Design

Figure 49 shows a block diagram of the peripheral device that was designed to interface with MEDs to provide them with the capability to measure electrical impedance. The device was designed using low-power electronics and to be powered

with one of the two audio channels of a MED. The second channel drives the sensor, and the microphone input collects data from the device. This design utilizes the analog to digital converter (ADC) and digital to analog converters (DAC) available on MEDs and thus reduces cost and complexity.

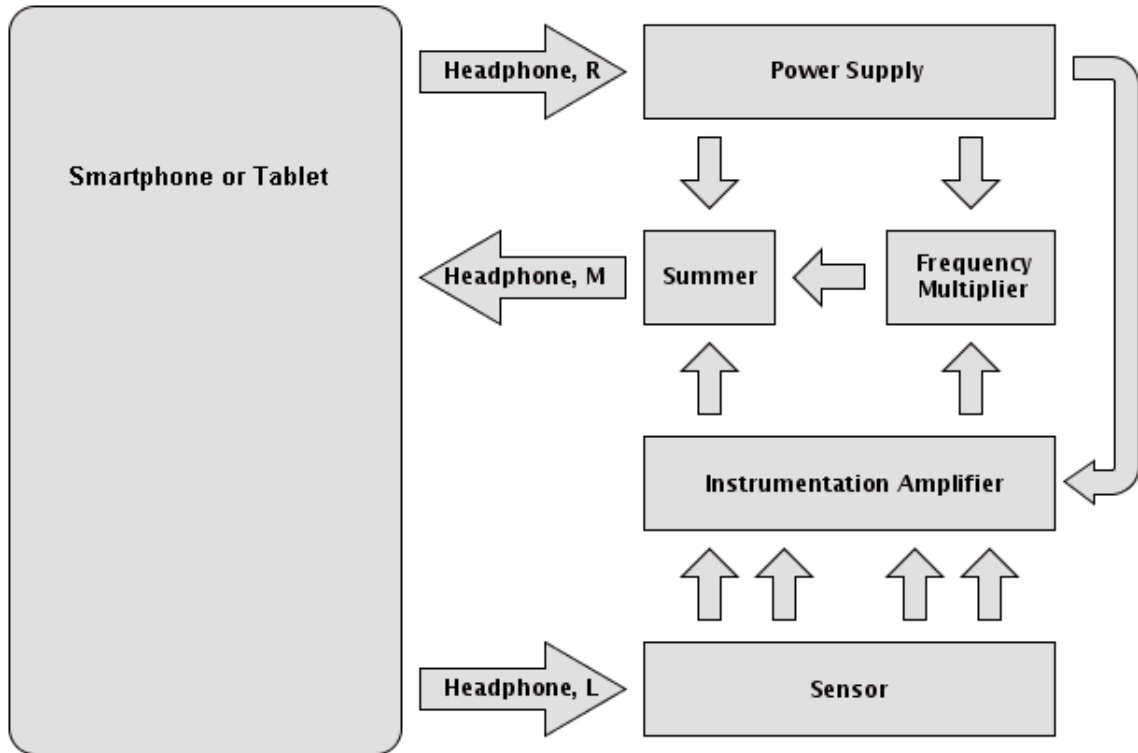


Figure 49. Block diagram for peripheral device design to provide MEDs with electrical impedance measurement capabilities.

Figure 50 shows a simplified schematic of the peripheral device. Part numbers for components that could be used to realize this device are indicated.

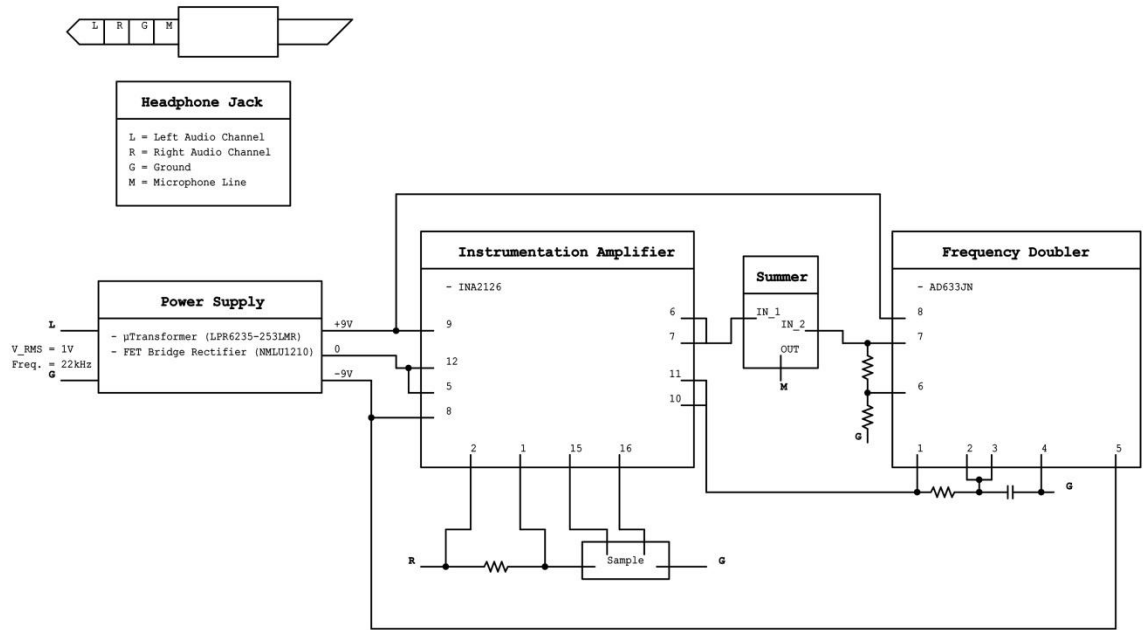


Figure 50. Simplified schematic for peripheral device with part numbers indicated.

4. DISCUSSION

The differences in color intensity between adjacent concentrations are subtle, and the lowest several concentrations are not discernible with the human eye; however, many more differences and concentration levels can be discerned and detected using image analysis and conductimetry.

4.1. Visual

The unaided eye is capable of a low detection limit equivalent to a GNP concentration of $(3.98 \pm 0.40) \times 10^{-11}$ M. This is sufficient for many diagnoses, e.g., pregnancy, which requires hCG detection at a level of $\sim 10^{-11}$ M to be considered positive [20] [45]. However, it is significantly higher than other methods that were tested and it lacks a capability for objective quantitative results.

4.2. Image Analysis

Analysis of the spectral responses of the cameras in each of the MEDs revealed that the peak sensitivity for the green channel in each case was closer to the wavelengths of interest than that of either the red or blue channel (as was expected). The Galaxy S showed a higher LOD than either of the other MEDs. This can possibly be explained by its green channel being more sensitive to a broader range of wavelengths, which could result in more reflected light not specifically at the wavelength of interest being detected by the sensor, decreasing the difference in intensity between the white reference and the sample.

Data collected with the MED and microscope cameras were observed to follow the Beer-Lambert law (eq. 8). They were highly linear, with $R^2 > 0.99$ in all cases. Some deviation from theory was observed to varying degrees in the y-intercepts, which should be null to match the law. Since this doesn't affect the linearity of the relationships, it is unimportant to LOD determination or quantifiability of measurements. This deviation is likely caused by the NC in the sample areas being more reflective after being wetted and dried, regardless of sample content, compared to the white reference areas which were never wetted. Wetting probably has an effect of settling surface features, making the surface smoother and allowing it to reflect light more coherently. The reflection is still diffuse, but is more specular than it would otherwise be. Illumination probably also plays a role in this effect. The lighting setup used a lamp about 45° from normal to prevent shadows from being cast by the camera.

The microscope, with both $5\times$ and $10\times$ objectives, was able to achieve a lower LOD than the MEDs most likely because of the high degree of consistency with the lighting conditions. The microscope used light from a dedicated lamp which was routed through an internal optical system then focused into a beam emanating from the objective. The beam was reflected off of the subject, reentering the objective and being routed to and projected onto the image sensor. Incident light intensity, focus, and exposure were set manually, and remained constant, throughout all data collection.

Image processing and analysis was executed on a computer with a 2.2 GHz dual core processor and 2 GB of memory and suffered from no significant slowing. These

specifications are comparable to many modern MEDs, so there is no foreseeable problem with porting the programs to mobile applications and running them on MEDs.

4.3. Conductimetric Detection

Comparison of two- and four-terminal measurement approaches showed that contact resistance was significant and variable. Since this was the case, smaller impedances resulting from the measurement target, and changes to these values, were lost within the larger values obtained when two-terminals were used. The use of four terminals separates the current and voltage electrodes and eliminates contact resistance from measurements.

The lowest LOD of any method that was tested was achieved with the conductimetric approach. Like with the other quantitative methods that were tested, a highly linear relationship was observed between concentration and response ($R^2 > 0.99$). The y-intercept is the result of several physical variables which were maintained constant throughout testing, and is the conductivity of the colloidal gold at infinite dilution. These include the PBS which was used to dilute the colloidal gold and the NC. According to the relationship that was observed, each GNP contributes a constant amount to sample conduction. The shape of the relationship also provides reassurance that the variable affecting conductivity really is GNP concentration and not electrolyte concentration in the buffer (which would be the case if the PBS was a different concentration from the 0.1 mM that the GNPs were suspended in). If a very different concentration of PBS were used to dilute the colloidal gold, and GNPs did not contribute to conduction, a

relationship following Kohlraush's law would be expected (conductivity would change proportionally with concentration raised to the $3/2$ power). With experimentation, it would be possible to determine which variables and physical constants are represented in the linear equation that was found and to form a theoretically meaningful relationship.

As shown in Figure 38, the impedance magnitude data collected in time for the samples follow a parabolic form. The hypothesized reason for this relationship is that as the concentration of GNPs increases as sample water evaporates, conductance increases; however, eventually a critical point is reached where there is not a sufficient amount of water present to effectively conduct and impedance starts increasing again. The impedance magnitude value that was used was taken from the minimum of the second order polynomial that was fit to the parabola formed by the data. This was chosen as the measurement point because even in cases where evaporative rate is inconsistent, the point where the effects of increasing concentration and decreasing fluid for conduction balance each other is the same.

The output on the instrumentation amplifier that measures the voltage between the two center probes occasionally showed some slightly erratic behavior at certain times during measurement, characterized by wandering DC offset. One possible solution would be to place high pass filters at the inputs to the amplifier, which would attenuate low frequencies to keep the signal centered on the horizontal axis. Under most circumstances, this DC offset posed no problem because signal amplitude was the value that was being measured, but occasionally the DC offset would wander far enough to cause saturation

and the signal's amplitude would drop to zero, rendering some measurements useless and necessitating repeats.

The factor, k , which was used to present actual label concentrations that were tested in terms of equivalent sample target concentrations, was calculated for the parameters that were used. This effort allows data and results to be presented in a meaningful way, where comparison with other work is easily facilitated (all one has to do is convert the analyte concentration of interest to or from units of M). For specific assays of interest, it may be useful to recalculate k , considering the relevant variables discussed above, including sample volume, detection region volume, membrane porosity, conjugate concentration, conjugate pad volume and porosity, range of possible sample analyte concentrations, label binding capacity, and immobilized capture antibody concentration.

4.3.1. Peripheral Device

The driving idea behind the design of the peripheral device was to bring conductimetric measurement capabilities to MEDs with simplicity. Initially, a concept was devised which would incorporate measurement instrumentation, a digital to analog converter, memory, a processor, a power source, and a transmitter and receiver for communications via Bluetooth. This device would be fairly complex and expensive. With the goal of reduced complexity, a better design was conceptualized which provided better compatibility, adequate functionality, and reduced the number of parts needed leading to a low projected cost.

This design utilizes the onboard digital to analog and analog to digital converters found on MEDs and computers to draw power and for communications. The stereo audio output and microphone line in are connected to these converters which are accessible through MED headphone jacks. One of the audio channels would be used as a function generator to drive the sensor. A dual instrumentation amplifier is used to acquire the current through the sensor and the voltage across the two central terminals. This IA has two outputs, while the MED only has one microphone line in. To transmit the information from these outputs simultaneously over the same line, the frequency for one signal was shifted using a multiplier. The same signal was applied to both the multiplier inputs, but a constant 90° phase delay is introduced to one input, the effect being a doubling of the original frequency, and a gain of 0.5. The second audio channel was used to supply power to the peripheral device. This doubled output and the other unmodified output from the IA were then summed. After the signal was received by the MED, it was decomposed to its original component waveforms in software using Fourier analysis.

Low-power electronics were chosen for the design to not exceed the power limitation that the audio channel is capable of supplying. This allows a MED to power the peripheral device solely from its battery without requiring an external power source.

4.4. Comparison to Literature

The lowest reported LOD with standard LFA technology (GNP labeled antibody, dried into a conjugate pad and run on a nitrocellulose membrane) that was found in the literature was 3×10^{-11} M, which is on par with the visual detection limit that was found,

$(3.98 \pm 0.40) \times 10^{-11}$ M. The absolute lowest LOD that was found reported in the literature was 10^{-16} M, which is about two orders of magnitude more sensitive than the LOD determined for the conductimetric approach, $(2.66 \pm 0.27) \times 10^{-14}$ M; however, this low detection limit was achieved using an alternative fluorescent label and a mix and run technique [46]. It should be noted that the LOD values that were determined are considered to be optimal and that further testing would be necessary to determine LODs for specific assays.

4.5. LOD Comparison

An important result of this work is the comparison of the LODs possible with each measurement approach. Figure 51 shows the LODs that were determined.

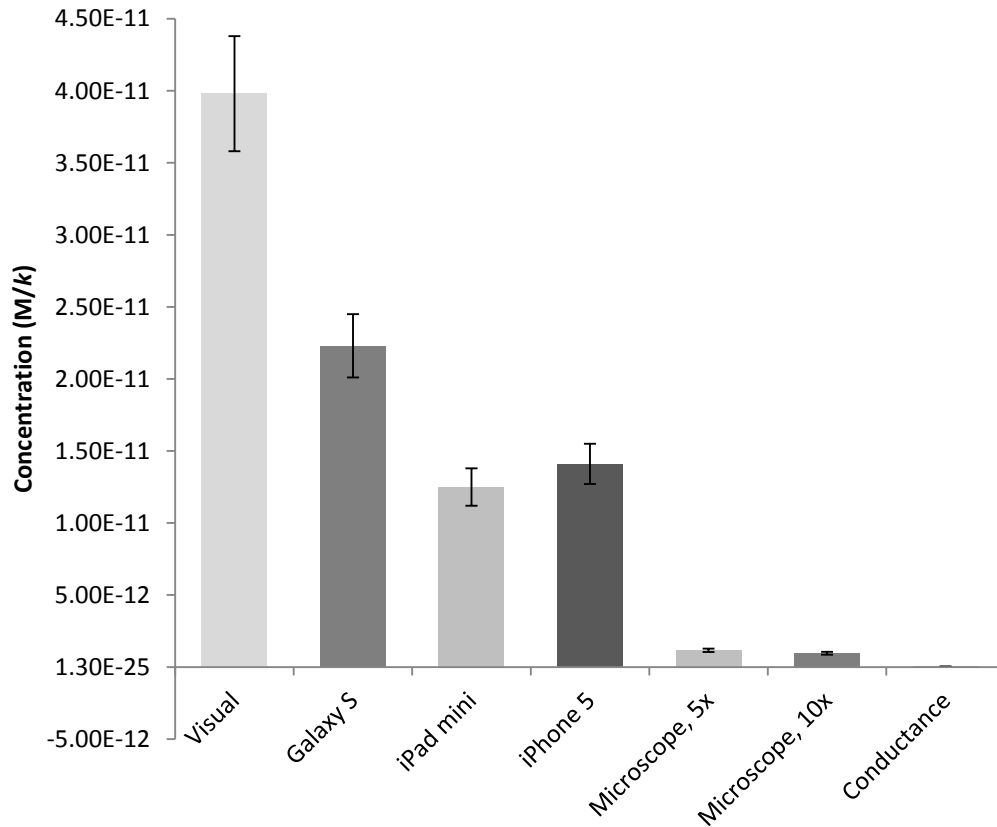


Figure 51. Comparison of LODs obtained with different measurement approaches. Error bars represent SEM.

Levene's test showed that the sample groups had unequal variances ($p < 0.001$). This was resolved through logarithmic transformation of the data (Levene; $p = 0.192$). One-way ANOVA was used to determine that there were significant differences in the LODs ($F(6,63) = 453.83, p < 0.0001$) and Tukey's test was used to find locations. Figure 52 shows the LODs with significant differences indicated.

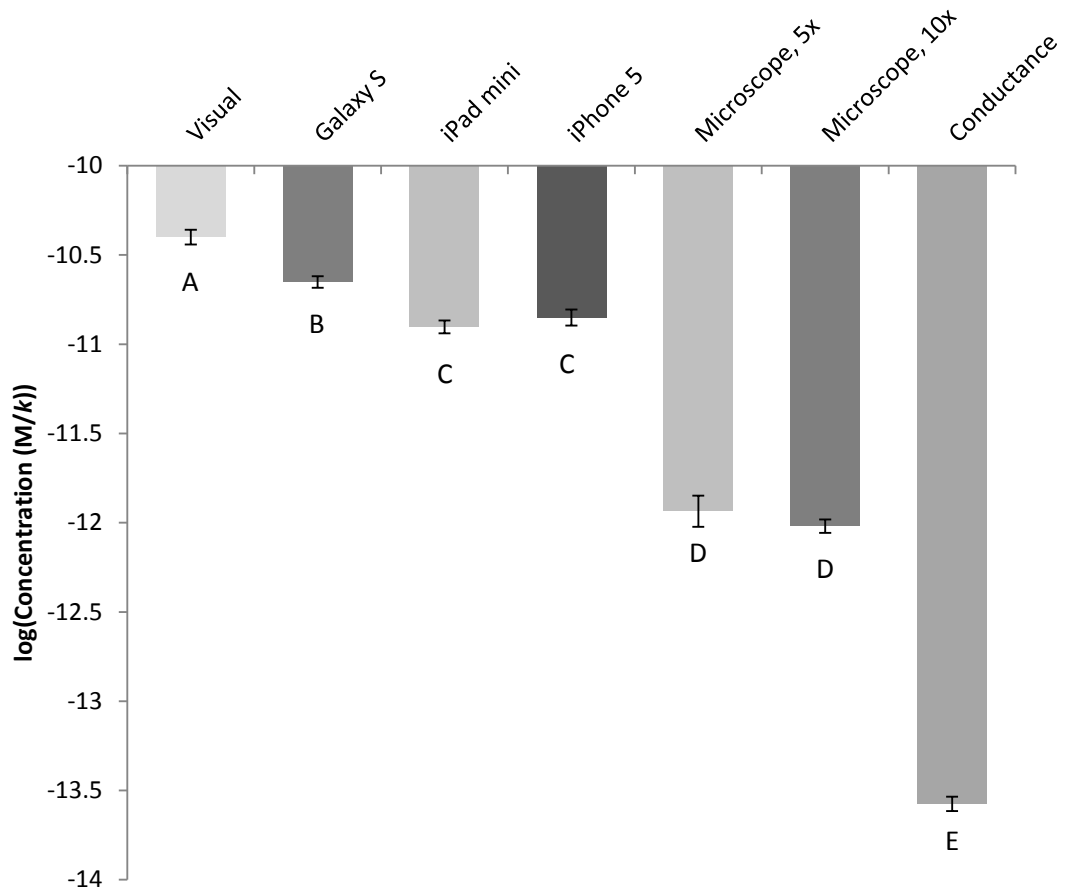


Figure 52. Comparison of LODs obtained with each approach (after logarithmic transformation of the data). Error bars represent SEM. Tukey results are shown as letters below each column. Groups not sharing letters are significantly different ($p < 0.01$).

5. CONCLUSIONS

The results from MED testing show that these devices can be used to achieve lower LODs than the unaided eye and with the quantified data. Additionally, these results show that it is feasible to use these devices for simultaneous measurements with multiplexed assays.

Each method that was tested has its own set of advantages and disadvantages. Circumstances also dictate which method is most appropriate. The unaided eye method requires very few resources and can be quickly and easily performed. One downside is that training is required to obtain consistent results, and even so, it is a subjective process. Also, this approach lacks the capability to generate quantified data, and compared to the others that were tested, its LOD is high.

The use of MEDs with image analysis is quick and very straightforward. This technique enables simultaneous quantitative measurements on multiplexed assays. The LOD that is possible with this approach is better than the visual detection limit, but it is not as low as with some of the other techniques that were tested.

The microscope approach offered low LODs compared to the other optical techniques. Quantitative measurement was possible, but only for a single sample at a time. This process is also much slower than the MED or visual approaches.

The conductimetric approach was capable of a very low LOD and quantitative measurement. Disadvantages to this approach were that it is fairly slow, and requires more effort than the others that were tested. Additionally, measurements are sensitive to more environmental variables like temperature.

In most situations, the MED image analysis approach is ideal since it provides a reasonably low LOD, is user friendly, the required equipment is relatively inexpensive and ubiquitous, and it can output objective, quantified data for multiplexed assays. If the peripheral device design which is proposed is further developed, it could be implemented for conductimetric measurement with MEDs. This would provide a capability for detection with lower LODs for assays where the image analysis approach is not capable of detecting at a sufficiently low concentration.

5.1. Future Work

One important continuation of this work would be to determine the full linear range for each of the methods (except for visual). In order to accomplish this, it would be necessary to extend the concentration range of erythrosine and colloidal gold to include higher concentrations. Data would need to be collected and fit to the established linear models for each of the methods. At some concentration for each, measurements are expected to deviate from linear. Experimental absorbance versus concentration data typically deviate from the Beer-Lambert law by becoming more horizontal at high concentrations, but it is unclear how experimental conductivity versus concentration data would deviate from the relationship that was observed for the concentration range that was tested.

Adding a narrow band pass color filter to the MED cameras and microscope would likely result in decreased variance in measurements and lower LODs. These cameras already employ filters to restrict incident light collected by the image sensor to a

particular range of wavelengths for each color channel. Further restricting this to a narrower range around the wavelength of interest would reduce reflected light at wavelengths that cannot be absorbed by detector labels from being detected by the image sensor.

The experiments that were performed with detectors should be repeated with the complete biochemistry that would be used with actual diagnostic assays. This would include an analyte, detectors conjugated with antibodies, and immobilized primary and secondary antibodies. A simple and inexpensive way to complete experiments with these considerations might be to use modified commercial home pregnancy tests. Dilutions could be prepared with hCG and then administered to assays. Analysis with the MED image analysis approach would be straightforward. If tests that utilize GNPs as detectors are used, it would be possible to test the conductimetric approach and make a comparison.

The possible effects of constituents of biofluids, especially on conductivity, should be explored. This could be done by using buffers formulated to match the conductivities of biofluids of interest.

A consideration that should be explored for conductimetric measurements is that when working with biological (or simulated biological) fluids, other constituents may contribute significantly to conduction. It may be necessary to follow the sample with DI to carry away constituents that are not the target of measurement. Simultaneous measurement of the detection region and the sample, directly, may also provide a way to

make measurements in this type of environment – one would measure the signal above the baseline of the sample. This would also allow for a way to compensate for temperature.

The software that was developed in MATLAB and LabVIEW should be ported and further developed in iOS and Android applications so that it can be used directly with MEDs. This can be easily achieved for the image analysis algorithms using MATLAB Coder. The LabVIEW program can be implemented directly in Xcode and Android Studio.

BIBLIOGRAPHY

1. Chin, Curtis D., Vincent Linder, and Samuel K. Sia. "Lab-on-a-chip devices for global health: Past studies and future opportunities." *Lab on a Chip* 7.1 (2007): 41-57.
2. World Health Organ. 2005. *World health report 2005: making every mother and child count*. Geneva: World Health Organ.
3. World Health Organ. 2014. *Fact Sheet N°310 - Death: Top 10 Causes*. Geneva: World Health Organ.
4. Yager, Paul, Gonzalo J. Domingo, and John Gerdes. "Point-of-care diagnostics for global health." *Annu. Rev. Biomed. Eng.* 10 (2008): 107-144.
5. Dheda, Keertan, et al. "Point-of-care diagnosis of tuberculosis: Past, present and future." *Respirology* 18.2 (2013): 217-232.
6. Hay Burgess DC, Wasserman J, Dahl CA. 2006. *Global health diagnostics*. *Nature* 444(Suppl. 1):1-2.
7. Girosi F, Olmsted SS, Keeler E, Hay Burgess DC, Lim YW, et al. 2006. *Developing and interpreting models to improve diagnostics in developing countries*. *Nature* 444(Suppl. 1):3-8.
8. Martinez, Andres W., et al. "Diagnostics for the developing world: microfluidic paper-based analytical devices." *Analytical chemistry* 82.1 (2009): 3-10.
9. Morse, Stephen A., et al. "Detecting biothreat agents: the laboratory response network." *ASM News-American Society for Microbiology* 69.9 (2003): 433-437.
10. Watkins, Sharmila D., Tammie McGrath. "Exploration Medical Condition List." NASA/Johnson Space Center (2013).

11. Polk, J.D. "Exploration Medical Capability Functional Requirements Document."
NASA/Johnson Space Center (2011).
12. Peetz, Dirk, et al. "Glycogen phosphorylase BB in acute coronary syndromes."
Clinical Chemical Laboratory Medicine 43.12 (2005): 1351-1358.
13. De Luca, Giuseppe, et al. "Time delay to treatment and mortality in primary
angioplasty for acute myocardial infarction every minute of delay counts."
Circulation 109.10 (2004): 1223-1225.
14. Tito, Dennis A., et al. "Feasibility analysis for a manned mars free-return mission in
2018." Aerospace Conference, 2013 IEEE. IEEE, 2013.
15. Millipore. "Rapid Lateral Flow Test Strips: Considerations for Product
Development." (2008).
16. Posthuma-Trumpie, Geertruida A., Jakob Korf, and Aart van Amerongen. "Lateral
flow (immuno) assay: its strengths, weaknesses, opportunities and threats. A
literature survey." Analytical and bioanalytical chemistry 393.2 (2009): 569-582.
17. Mansfield, Michael A. "The use of nitrocellulose membranes in lateral-flow assays."
Drugs of Abuse. Humana Press, 2005. 71-85.
18. Gessler, Frank, et al. "Evaluation of lateral flow assays for the detection of botulinum
neurotoxin type A and their application in laboratory diagnosis of botulism."
Diagnostic microbiology and infectious disease 57.3 (2007): 243-249.
19. Virekunnas, Laura. "Colloidal Gold and Paramagnetic Labels in Lateral Flow Assay
Detecting Ricin."

20. Cole, Laurence A. "New discoveries on the biology and detection of human chorionic gonadotropin." *Reprod Biol Endocrinol* 7.8 (2009): 1-37.
21. Butler, Stephen A., Sarah A. Khanlian, and Laurence A. Cole. "Detection of early pregnancy forms of human chorionic gonadotropin by home pregnancy test devices." *Clinical Chemistry* 47.12 (2001): 2131-2136.
22. Willets, Katherine A., and Richard P. Van Duyne. "Localized surface plasmon resonance spectroscopy and sensing." *Annu. Rev. Phys. Chem.* 58 (2007): 267-297.
23. Mayer, Kathryn M., and Jason H. Hafner. "Localized surface plasmon resonance sensors." *Chemical reviews* 111.6 (2011): 3828-3857.
24. Arruebo, Manuel, Mónica Valladares, and África González-Fernández. "Antibody-conjugated nanoparticles for biomedical applications." *Journal of Nanomaterials* 2009 (2009): 37.
25. Millipore. "Hi-Flow Plus Membranes and Surewick Pad Materials." (2012).
26. Xerox. "Material Safety Data Sheet: Solid Ink - Black, Cyan, Yellow, Magenta." (2011).
27. Carrilho, Emanuel, Andres W. Martinez, and George M. Whitesides. "Understanding wax printing: a simple micropatterning process for paper-based microfluidics." *Analytical chemistry* 81.16 (2009): 7091-7095.
28. Jaeger, C.W. "Colorant compounds, phase change ink compositions and methods of printing." CA2355533C Canada, July 11, 2006. Grant.

29. Lo, Katey, et al. (MIT OpenCourseWare: Massachusetts Institute of Technology), 6.S079 Nanomaker, Spring 2013. (Accessed 21 Jul, 2014). License: Creative Commons BY-NC-SA.
30. Washburn, Edward W. "The dynamics of capillary flow." *Physical review* 17.3 (1921): 273.
31. De Feijter, J. A., D. J. Benjamins, and F. A. Veer. "Ellipsometry as a tool to study the adsorption behavior of synthetic and biopolymers at the air–water interface." *Biopolymers* 17.7 (1978): 1759-1772.
32. Kaur, Kanwarjeet, and James A. Forrest. "Influence of particle size on the binding activity of proteins adsorbed onto gold nanoparticles." *Langmuir* 28.5 (2012): 2736-2744.
33. Malmsten, Martin. "Ellipsometry studies of the effects of surface hydrophobicity on protein adsorption." *Colloids and Surfaces B: Biointerfaces* 3.5 (1995): 297-308.
34. Cytodiagnostics. "Covalent Conjugation to Cytodiagnostics Carboxylated Gold Nanoparticles - Tech Note #105." (2014).
35. Sigma-Aldrich. "Product Specification: Gold Nanoparticles - 50 nm Diameter, OD = 1, Stabilized Suspension in 0.1 mM PBS, Reactant Free." (2014).
36. Sigma-Aldrich. "Product Specification: Erythrosin B - Dye Content \geq 95%." (2014).
37. Bhowmik, Benoy B., and Papia Ganguly. "Photophysics of xanthene dyes in surfactant solution." *Spectrochimica Acta Part A: Molecular and Biomolecular Spectroscopy* 61.9 (2005): 1997-2003.
38. Thermo Scientific. "Finnpipette - Good Laboratory Pipetting Guide." (2010).

39. Cytodiagnostics. "Gold Nanoparticle Storage & Handling - Tech Note: #101."
(2014).
40. Guillén, Isabel Guillén, et al. "Development of Lateral Flow Immunoassay for Rapid
Detection of Oxytetracycline in Honey Samples." *Tc* 16: 17.
41. PublicLaboratory.org. "Public Lab Foldable Mini-spectrometer." (2012).
42. Wilson, Tracy V. "How the iPhone works." Retrieved from:,(Jan. 2007) (2007).
43. PELCO. "Technical Notes: PELCO Conductive Graphite - Isopropanol Based,
Product No. 16053." (2014). .
44. CAIG Laboratories, Inc. "Data Sheet: CircuitWriter CW100L Liquid." (2014).
45. Sigma-Aldrich. "Product Specification: Chorionic gonadotropin human." (2011). .
46. Gordon, Julian, and Gerd Michel. "Analytical sensitivity limits for lateral flow
immunoassays." *Clinical chemistry* 54.7 (2008): 1250-1251.
47. Hu, Min, et al. "Gold nanostructures: engineering their plasmonic properties for
biomedical applications." *Chemical Society Reviews* 35.11 (2006): 1084-1094.
48. Jiang, Jun, et al. "What is the space of spectral sensitivity functions for digital color
cameras?." *WACV*. 2013.
49. Malmsten, Martin. "Ellipsometry studies of the effects of surface hydrophobicity on
protein adsorption." *Colloids and Surfaces B: Biointerfaces* 3.5 (1995): 297-308.
50. Kim, Jeong-Hwan, et al. "Conductimetric membrane strip immunosensor with
polyaniline-bound gold colloids as signal generator." *Biosensors and
Bioelectronics* 14.12 (2000): 907-915.

APPENDICES

Appendix	Page
A : Image Analysis Code (MATLAB).....	102
B : Microscope Image Processing Code (MATLAB)	111
C : Electrical Impedance Measurement Block Diagram (LabVIEW)	112
D : Impedance Value Extraction Code (MATLAB).....	113
E : GNP Concentration Protocol.....	115

APPENDIX A: Image Analysis Code (MATLAB)

```
clear all
close all
clc

% Read Image
image = imread(uigetfile('*.jpg'));

% Get image dimensions
size_pre = size(image);

% Show Image
imshow(image);
clc

% Input corners from user mouseclicks
disp('Select center of upper left corner marker, |' square ...')
point_1 = ginput(1);
hold on
plot(point_1(1,1), point_1(1,2), 'g*')
clc

disp('Select centers of remaining three corner markers, squares ...')
point_2 = ginput(1);
plot(point_2(1,1), point_2(1,2), 'r*')

point_3 = ginput(1);
plot(point_3(1,1), point_3(1,2), 'r*')

point_4 = ginput(1);
plot(point_4(1,1), point_4(1,2), 'r*')
hold off
clc
pause(0.1)

% Determine angle and rotate
disp('Rotating. Please wait...')
corners = [point_2; point_3; point_4];

% Determine number of points to the left of the primary marker
n = 0;
for i = 1:3
    if corners(i,1) < point_1(1,1)
        n = n+1;
    end
end

% If 0 corners lie to the left of the primary marker, use
% the corner with the smallest y value to determine angle
```

```

% to rotate
if n == 0
    for i = 1:3
        if corners(i,2) == min(corners(:,2))
            min_y = corners(i,:);
        end
    end
    a = atand((min_y(1,2) - point_1(1,2))/(min_y(1,1) - ...
        point_1(1,1)));
    image = imrotate(image, a, 'loose');

% If 1 corner lies to the left of the primary marker, use
% the corner with the largest x value to determine angle
% to rotate
elseif n == 1
    for i = 1:3
        if corners(i,1) == max(corners(:,1))
            max_x = corners(i,:);
        end
    end
    a = atand((max_x(1,2) - point_1(1,2))/(max_x(1,1) - ...
        point_1(1,1)));
    image = imrotate(image, a, 'loose');

% If 2 corners lie to the left of the primary marker, use
% the corner with the largest x value to determine the angle
% to rotate
elseif n == 2
    for i = 1:3
        if corners(i,1) == max(corners(:,1))
            max_x = corners(i,:);
        end
    end
    a = atand((max_x(1,2) - point_1(1,2))/(max_x(1,1) - ...
        point_1(1,1)));
    image = imrotate(image, a, 'loose');

% If 3 corners lie to the left of the primary marker, use
% the corner with the largest y value to determine the angle
% to rotate and add 90 degrees
elseif n == 3
    for i = 1:3
        if corners(i,2) == max(corners(:,2))
            max_y = corners(i,:);
        end
    end
    a = 90 + atand((point_1(1,1) - max_y(1,1))/(max_y(1,2) - ...
        point_1(1,2)));
    image = imrotate(image, a, 'loose');

end

% Show rotated image and plot corner markers at new positions

```

```

imshow(image)
size_post = size(image);
x_correction = (size_post(2) - size_pre(2))/2;
y_correction = (size_post(1) - size_pre(1))/2;
hold on
markers = plot(point_1(1,1)+x_correction, point_1(1,2) ...
              +y_correction, 'g*', corners(:,1)+x_correction, ...
              corners(:,2)+y_correction, 'r*');
hold off
rotate(markers, [0 0 1], -a)

pause(0.1)

clc

% Extract new marker point locations
marker = findobj('Marker', '*', '-and', 'Color', 'g');
x = get(marker, 'Xdata');
y = get(marker, 'Ydata');
point_1 = [x(1), y(1)];

marker = findobj('Marker', '*', '-and', 'Color', 'r');
x = get(marker, 'Xdata');
y = get(marker, 'Ydata');
point_2 = [x(1), y(1)];
point_3 = [x(2), y(2)];
point_4 = [x(3), y(3)];

% Crop area outside of selection (to decrease processing time
% for transform)
min_x = min([point_1(1), point_2(1), point_3(1), point_4(1)]);
min_y = min([point_1(2), point_2(2), point_3(2), point_4(2)]);
max_x = max([point_1(1), point_2(1), point_3(1), point_4(1)]);
max_y = max([point_1(2), point_2(2), point_3(2), point_4(2)]);

rect = [min_x, min_y, max_x - min_x, max_y - min_y];
image = imcrop(image, rect);
imshow(image)

% Set new marker point locations
point_1 = [point_1(1) - min_x + 1, point_1(2) - min_y + 1];
point_2 = [point_2(1) - min_x + 1, point_2(2) - min_y + 1];
point_3 = [point_3(1) - min_x + 1, point_3(2) - min_y + 1];
point_4 = [point_4(1) - min_x + 1, point_4(2) - min_y + 1];

% Plot marker points at new locations
hold on
plot(point_1(1,1), point_1(1,2), 'g*', point_2(1,1), ...
     point_2(1,2), 'r*', point_3(1,1), point_3(1,2), 'r*', ...
     point_4(1,1), point_4(1,2), 'r*')
hold off

```



```

corners(1,:) = point_2;
corners(2,:) = point_3;
corners(3,:) = point_4;

% Apply projective transform to eliminate image skew
disp('Eliminating skew. Please wait...')
% Identify individual corners
for i = 1:3
    if corners(i,2) == min(corners(:,2))
        min_y = corners(i,:);

        elseif corners(i,1) == min(corners(:,1))
            min_x = corners(i,:);

        else
            max_xy = corners(i,:);
        end
    end
end

tform = maketform('projective', [point_1; min_y; min_x ...
    ; max_xy], [point_1; min_y(1,1), point_1(1,2); ...
    point_1(1,1), min_x(1,2); min_y(1,1), min_x(1,2)]);

image = imtransform(image, tform, 'XData', [1 ...
    size(image, 2)], 'YData', [1 size(image,1)]);
imshow(image)

corners = [min_y(1,1), point_1(1,2); point_1(1,1), ...
    min_x(1,2); min_y(1,1), min_x(1,2)];
hold on
plot(point_1(1,1), point_1(1,2), 'g*', corners(:,1), ...
    corners(:,2), 'r*');
hold off
pause(1.0)

clc

% Crop image to relevant area
disp('Cropping. Please wait...')
points = [point_1; corners];
rect = [min(points(:,1)), ...
    min(points(:,2)), ...
    max(points(:,1)) - min(points(:,1)), ...
    max(points(:,2)) - min(points(:,2))];
image = imcrop(image, rect);
imshow(image)
hold on
plot(1, 1, 'g*', [size(image, 2), size(image, 2), 1], ...
    [1, size(image, 1), size(image, 1)], 'r*');
hold off

clc

```

```

% Determine locations to sample

% Convert RGB to grayscale
bin_image=rgb2gray(image);

% Convert to black and white and invert
threshold = graythresh(bin_image) - 0.1;
bin_image = ~im2bw(bin_image, threshold);

% Remove all objects containing fewer pixels than 1% of
% the smallest dimension
bin_image = bwareaopen(bin_image, round(min(size ...
    (bin_image))*0.01));

%Dilate objects in image
se = strel('square', 8);
bin_image = imdilate(bin_image, [se]);

% Identify tick marks on top of image
n = 1;
m = 1;
for i = 1:size(bin_image,2)
    if bin_image(1,i) == 1
        tick(n) = i;
        n = n+1;
    elseif bin_image(1,i) == 0 && bin_image(1,i) ~= ...
        bin_image(1,i-1)
        tick_location_top(m) = round(mean(tick));
        m = m+1;
        tick = [];
        n = 1;
    end
end
if bin_image(1,1) == 1
    tick_location_top(1) = [];
end

% Identify tick marks on bottom of image
n = 1;
m = 1;
tick = [];
for i = 1:size(bin_image,2)
    if bin_image(size(bin_image,1),i) == 1
        tick(n) = i;
        n = n+1;
    %Note: Errors if starting point is black
    elseif bin_image(size(bin_image,1),i) == 0 && ...
        bin_image(size(bin_image,1),i) ~= ...
        bin_image(size(bin_image,1),i-1)
        tick_location_bottom(m) = round(mean(tick));
        m = m+1;
        tick = [];
    end
end

```

```

        n = 1;
    end
end
if bin_image(size(bin_image,1),1) == 1
    tick_location_bottom(1) = [];
end

% Identify tick marks on left side of image
n = 1;
m = 1;
tick = [];
for i = 1:size(bin_image,1)
    if bin_image(i,1) == 1
        tick(n) = i;
        n = n+1;
    elseif bin_image(i, 1) == 0 && bin_image(i, 1) ~= ...
        bin_image(i-1, 1)
        tick_location_left(m) = round(mean(tick));
        m = m+1;
        tick = [];
        n = 1;
    end
end
if bin_image(1,1) == 1
    tick_location_left(1) = [];
end

% Identify tick marks on right side of image
n = 1;
m = 1;
tick = [];
for i = 1:size(bin_image,1)
    if bin_image(i,size(bin_image,2)) == 1
        tick(n) = i;
        n = n+1;
    elseif bin_image(i,size(bin_image,2)) == 0 && ...
        bin_image(i,size(bin_image,2)) ~= ...
        bin_image(i-1,size(bin_image,2))
        tick_location_right(m) = round(mean(tick));
        m = m+1;
        tick = [];
        n = 1;
    end
end
if bin_image(1,1) == 1
    tick_location_right(1) = [];
end

% Plot grid (intersections are sample locations)
hold on
for i = 1:size(tick_location_top,2)
    plot([tick_location_top(i); tick_location_bottom(i)], ...
        [1; size(bin_image, 1)], '-w')
end

```

```

for i = 1:size(tick_location_left,2)
    plot([1; size(bin_image, 2)], [tick_location_left(i); ...
        tick_location_right(i)], '-w')
end
hold off

% Find intersection points
sample_point = zeros(size(tick_location_left,2), ...
    size(tick_location_top,2), 2);
for i = 1:size(tick_location_left,2)
    for j = 1:size(tick_location_top,2)
        if tick_location_top(j) == tick_location_bottom(j)
            %Modify vertical lines by a pixel to avoid problems
            tick_location_bottom(j) = tick_location_bottom(j) + 1;
        end
        m1 = (size(bin_image,1) - 1)/(tick_location_bottom(j) - ...
            tick_location_top(j) + eps);
        b1 = 1 - m1*(tick_location_top(j));
        m2 = (tick_location_right(i) - ...
            tick_location_left(i))/(size(bin_image,2) - 1);
        b2 = tick_location_left(i) - m2*(1);
        lin_sys = [m1, 1, b1; m2, 1, b2];
        rref_lin_sys = rref(lin_sys);
        sample_point(i, j, 1) = -round(rref_lin_sys(1,3));
        sample_point(i, j, 2) = round(rref_lin_sys(2,3));
    end
end

% Note that values in sample_point(:, :, 1) are 'x'
% locations and their corresponding values in
% sample_point(:, :, 2) are 'y'

% Find background location points (use white region
% directly below each sample point)
wb_point = zeros(size(sample_point,1),size(sample_point,2),2);
for j = 1:size(sample_point,2)
    for i = 1:size(sample_point,1)
        if i ~= size(sample_point,1)
            wb_point(i, j, 1) = round(mean(sample_point(i, ...
                j, 1), sample_point(i+1, j, 1)));
            wb_point(i, j, 2) = sample_point(i, j, 2) + ...
                round((sample_point(i+1, j, 2) - ...
                    sample_point(i, j, 2))/2);
        elseif i == size(sample_point,1)
            wb_point(i, j, 1) = sample_point(i, j, 1);
            wb_point(i, j, 2) = sample_point(i, j, 2) + ...
                round((sample_point(i, j, 2) - ...
                    sample_point(i-1, j, 2))/2);
        end
    end
end

% Extract samples and background regions (use 11x11 pixel area)

```

```

current_sample = zeros(1,3);
current_wb = zeros(1,3);
for j = 1:size(sample_point,2)
    for i = 1:size(sample_point,1)
        for k = 1:3
            current_sample(i, j, k) = ...
                (mean(mean(image(sample_point(i,j,2)-5: ...
                    sample_point(i,j,2)+5, sample_point(i,j,1)-5: ...
                    sample_point(i,j,1)+5, k)))));
            current_wb(i, j, k) = (mean(mean(image ...
                (wb_point(i,j,2)- 5:wb_point(i,j,2)+5, ...
                wb_point(i,j,1)-5:wb_point(i,j,1)+5, k)))));
        end
    end
end

% Plot background locations
hold on
plot(wb_point(:, :, 1), wb_point(:, :, 2), 'k.');
```

```

current_sample = uint8(current_sample);

current_wb = uint8(current_wb);

% Use green channel (RGB, 2)
sample_g = current_sample(:, :, 2);
wb_g = current_wb(:, :, 2);

% Determine mean and standard deviation for each column, 1 through 10.
absorbance = -log10(double(sample_g)./double(wb_g));
for i = 1:10
    absorbance_avg(i) = mean(absorbance(:,i));
    absorbance_std(i) = std(absorbance(:,i))/sqrt(10);
end

% Input concentrations. First 10 columns are dye, 11th is GNP, 12th is
% blank. Also input concentration factor, k.
prompt = {'Column 1:', 'Column 2:', 'Column 3:', 'Column 4:', ...
    'Column 5:', 'Column 6:', 'Column 7:', 'Column 8:', ...
    'Column 9:', 'Column 10:', 'Column 11 (GNP):', 'k:'};
dlg_title = 'Concentrations and Inputs';
num_lines = 1;
def = {'0.07409187', '0.042581536', '0.024472148', ...
    '0.014064453', '0.008083019', '0.004645413', '0.002669778', ...
    '0.001534355', '0.000881813', '0.000506789', '4.66290269E-10', '143'};
answer = inputdlg(prompt, dlg_title, num_lines, def, 'on');
concentration = zeros(1,10);
for i = 1:10
    concentration(i) = str2num(answer{i});
end

```

```

end

% Molar concentration of full strength GNP (after concentrating 8x
% (8*5.8286283626702E-11 M))
conc_GNP = str2num(answer{11});

% Concentration factor, k.
k = str2num(answer{12});

% Perform linear regression and plot data and error bars.
[xData, yData] = prepareCurveData( concentration, absorbance_avg );

% Set up fittype and options.
ft = fittype( 'poly1' );

% Fit model to data.
[fitresult, gof] = fit( xData, yData, ft );

% Plot fit with data.
figure( 'Name', 'Absorbance vs. Concentration' );
errorbar(concentration,absorbance_avg,absorbance_std, 'b. ');
hold on
h = plot( fitresult, xData, yData );
% Get coefficients of line
c = coeffvalues(fitresult);
legend( h, 'Absorbance vs. Concentration', strcat('A = ' ...
    , num2str(c(1)), 'C + (' , num2str(c(2)), '), R^2 = ', ...
    num2str(gof.rsquare)), 'Location', 'North' );
% Label axes
xlabel( 'Concentration' );
ylabel( 'Absorbance' );
grid off

% Determine and plot LOD
LODy = mean(absorbance(:,12)) + 3*(std(absorbance(:,12)));
LODx = (LODy - c(2))/c(1);
hold on
plot(LODx,LODy,'rs')
text(LODx+.0005,LODy-.0005,'LOD')

% Determine x value for full strength GNP
GNPy = mean(absorbance(:,11));
GNPx = (GNPy - c(2))/c(1);

% Calculate dye concentrations equivalent to GNP in M/k (based on
% comparison to absorbance of GNP)
concentration_GNP = ((conc_GNP/GNPx)*concentration)/k;

% Calculate LOD concentration equivalent to GNP in M
conc_GNP_LOD = ((conc_GNP/GNPx)*LODx)/k

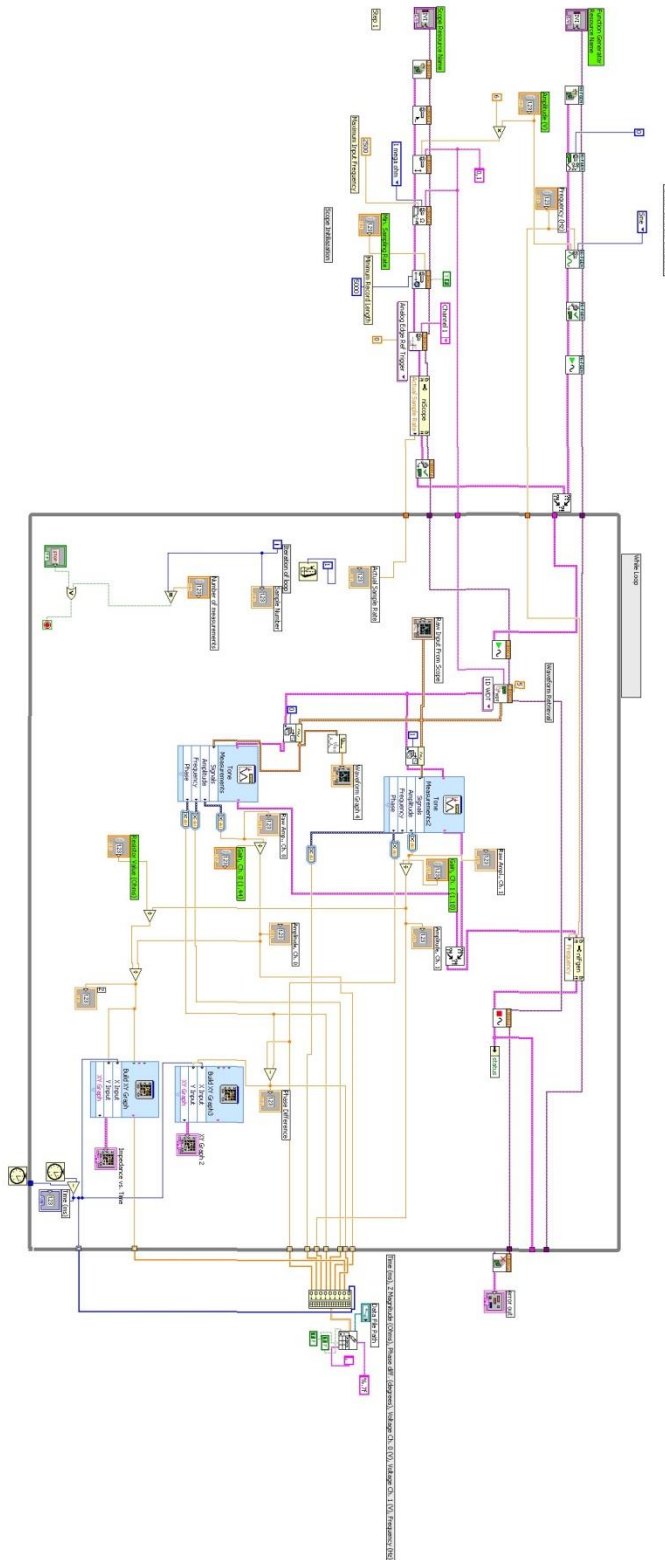
```

APPENDIX B: Microscope Image Processing Code (MATLAB)

```
clear all
clc

myFolder = uigetdir;
if ~isdir(myFolder)
    errorMessage = sprintf('Error: The following folder does not...
exist:\n%s', myFolder);
    uiwait(warndlg(errorMessage));
    return;
end
filePattern = fullfile(myFolder, '*.jpg');
jpegFiles = dir(filePattern);
data = cell(length(jpegFiles), 2);
for k = 1:length(jpegFiles)
    baseFileName = jpegFiles(k).name;
    fullFileName = fullfile(myFolder, baseFileName);
    fprintf(1, 'Now reading %s\n', baseFileName);
    imageArray = imread(fullFileName);
    data{k,1} = baseFileName;
    data{k,2} = mean(mean(imageArray(:,:,2)));
end
```

APPENDIX C: Electrical Impedance Measurement Block Diagram (LabVIEW)



APPENDIX D: Impedance Value Extraction Code (MATLAB)

```
close all
clear all
clc

% Import data from csv file
data = csvread(uigetfile('*.csv'));

x = data(:,1);
y = data(:,2);
clear data

% Plot data
plot(x,y);
axis([min(x) max(x) min(y) max(y)]);
% Label axes
xlabel( 'x, Time (ms)' );
ylabel( 'y, Impedance (ohms)' );

% Input x range bounds from mouse clicks
disp('Select minimum, then maximum x values')
x_min = ginput(1);
x_min = x_min(1);

x_max = ginput(1);
x_max = x_max(1);

close

% Find min and max x index values and crop data
for i = 1:size(x,1)
    if x(i) >= x_min-50 && x(i) <= x_min+50
        x_min_ind = i;
    elseif x(i) >= x_max-60 && x(i) <= x_max+60
        x_max_ind = i;
    end
end

x(x_max_ind:end) = [];
x(1:x_min_ind) = [];
y(x_max_ind:end) = [];
y(1:x_min_ind) = [];

[xData, yData] = prepareCurveData( x, y );

% Set up fittype and options.
ft = fittype( 'poly2' );
```

```

% Fit model to data.
[fitresult, gof] = fit( xData, yData, ft, 'Normalize', 'on' );

% Plot fit with data.
figure( 'Name', 'untitled fit 1' );
h = plot( fitresult, xData, yData );
legend( h, 'Impedance vs. Time', 'Polynomial fit', 'Location',
'NorthEast' );
% Label axes
xlabel( 'x, Time (ms)' );
ylabel( 'y, Impedance (ohms)' );
grid on

% Get coefficients of polynomial
c = coeffvalues(fitresult);

% Take derivative of function and determine the x value where the
% minimum occurs
x_val = -(c(2))/(2*(c(1)));

% Calculate and print minimum impedance value
min_impedance = c(1)*(x_val)^2 + c(2)*(x_val) + c(3)

% Print R^2 value
rsquare = gof.rsquare

```

APPENDIX E: GNP Concentration Protocol

A procedure described by Cytodiagnostics was followed in order to bring the GNP concentration up to a level high enough to be detected on NC optically [39].

Procedure:

1. Place aliquot of colloidal gold in appropriate centrifuge tube
2. Centrifuge the gold nanoparticles for 30 minutes using the appropriate G force depending on size of the gold nanoparticles (see Table 6)
3. Remove supernatant and re-suspend in appropriate volume of ultra-pure water
4. Vortex to re-disperse particles

Table 6. Appropriate Centrifuge Speeds and Times for Various GNP Sizes

Size (nm)	Speed (g)	Time (min)
5	100,000	30
10	17,000	60
15	17,000	30
20	6,500	30
30	4,500	30
40	2,500	30
50	2,000	30
60	1,125	30
80	600	30
100	400	30
150	180	30
200	100	30